UNIVERSITÀ DEGLI STUDI DI TRIESTE

XXIX CICLO DEL DOTTORATO DI RICERCA IN CHIMICA

New Molecules and Nano-materials for Artificial Photosynthesis

Settore scientifico-disciplinare: CHIM/06 Chimica Organica

DOTTORANDA
ERICA PIZZOLATO

COORDINATORE
PROF. MAURO STENER

SUPERVISORE DI TESI
PROF. MAURIZIO PRATO

ANNO ACCADEMICO 2015/2016

Abstract

The Thesis project has been focused on innovative synthetic systems for artificial photosynthesis. This is a complex photocatalytic architecture that allows the conversion of solar light into chemical energy, enabling water splitting into hydrogen and oxygen under visible light irradiation. With the principal aim of orchestrating physical and chemical interfaces, a great research effort is currently dedicated at the optimization of the envisaged molecular components, including light-antennae, photosensitizers and multi-redox catalysts, as independent building blocks, together with their arrangement within nano-structured environments that define geometry, morphology and surface properties of the resulting photosynthetic system.

In this Thesis, novel systems for photocatalytic water oxidation have been investigated, focusing on the design of catalyst-photosensitizers dyads by covalent (**Chapter 2**) or supramolecular strategies (**Chapter 3**). A final goal is the integration of these photosynthetic dyads on electroactive semiconductor surfaces, for the development of regenerative photoanodes (**Chapter 4**).

The PhD work has been developed along three main research lines:

1) The synthesis and characterization of a novel covalent dyad based on a Co(II) catalyst and a Ru(II) photosensitizer moiety (E. Pizzolato *et al. Phys. Chem. Chem. Phys.* **2014**, *16*, 12000). Combined electrochemical and photophysical studies reveal that photoinduced, redox events involving the two metal centres occur within a short timescale of 15 ps, confirming efficient electronic interactions between the two units and functional water oxidation activity (**Chapter 2**).
2) The study of a novel supramolecular assembly, combining an organic metal-free bis-cationic perylene bisimide (PBI) photosensitizer with a totally inorganic anionic polyoxometalate (Ru_4POM). This latter represents the state-of-the-art of molecular catalysts for water oxidation. This PBI self-assembles in water into 1-D structures and it provides one of the strongest photo-generated oxidant $E(PBI^{*2+/1+}) = 2.20$ V vs NHE; its combination with Ru_4POM is driven by electrostatic interactions and leads to the formation of a 2D porous hybrid architectures with a nano-lamellar sub-structure, alternating organic-inorganic molecular domains. This innovative supramolecular architecture shows: i) an ordered supramolecular structure; ii) fast photoinduced electron transfers (ET) in a 100 ps timescale (in the natural system, ET

occur in the 40 μs-1.6 ms range); iii) oxygenic activity under visible light in neutral aqueous solution (E. Pizzolato *et al.* "Perylene bisimides-oxygenic/polyoxometalates photosynthetic assemblies", manuscript in preparation) (**Chapter 3**).

3) The fabrication of composite photoanodes combining the photoactive PBI/Ru_4POM nano-hybrid with nanocrystalline tungsten-oxide (*nano*WO_3) as the semiconductor acceptor layer. The photoelectrode demonstrates catalytic activity upon illumination with visible light ($\lambda > 450$ nm) in slightly acidic electrolyte (pH 3), with a maximum photocurrent density of 75 μA/cm^2 at 1.20 V vs NHE and an Absorbed Photon to Current Efficiency (APCE) of 1.30%, superior to literature benchmark of 0.8% for PBI-sensitized photoelectrodes with IrO_2 as oxygen evolving catalyst (**Chapter 4**). This result paves the way to further improvement concerning the decoration of the semiconductor surface to boost the photocatalytic performance and to improve the photoelectrode robustness.

Sommario

Il progetto di Tesi propone sistemi sintetici innovativi per la fotosintesi artificiale. Questo processo si basa su una complessa architettura fotocatalitica che permette la conversione della luce solare in energia chimica, scindendo l'acqua in idrogeno e ossigeno mediante l'irraggiamento con luce visibile.

Attualmente, gli sforzi della ricerca sono indirizzati all'ottimizzazione dei singoli componenti molecolari, inclusi sistemi antenna, fotosensibilizzatori e catalizzatori redox, insieme alla loro disposizione in ambienti nanostrutturati che definiscono la geometria, la morfologia e le proprietà superficiali dei sistemi fotosintetici risultanti. Questo studio risulta decisivo allo scopo di orchestrare i diversi processi fisici e chimici che avvengono all'interfaccia tra queste diverse unità.

In questa Tesi sono stati studiati nuovi sistemi per l'ossidazione fotocatalitica dell'acqua, ponendo l'attenzione sulla progettazione di diadi catalizzatore-fotosensibilizzatore mediante un approccio covalente (**Capitolo 2**) o mediante un approccio supramolecolare (**Capitolo 3**). L'obiettivo finale è, quindi, l'integrazione di queste diadi fotosintetiche su superfici elettroattive, allo scopo di sviluppare efficienti fotoanodi (**Capitolo 4**).

Il progetto di dottorato si è sviluppato lungo tre diverse linee di ricerca:

1) La sintesi e la caratterizzazione di una nuova diade covalente basata su un catalizzatore di Co(II) e su un fotosensibilizzatore di Ru(II). (E. Pizzolato *et al. Phys. Chem. Chem. Phys.* **2014**, *16*, 12000). Studi combinati elettrochimici e fotofisici hanno rivelato la presenza di eventi redox tra i due centri metallici che avvengono in uno spazio temporale di 15 ps, confermando l'interazione elettronica tra le due unità e la sua attività di ossidazione dell'acqua (**Capitolo 2**).
2) Lo studio di un nuovo assemblaggio supramolecolare, che prevede la combinazione di un perilene bisimide (PBI), un fotosensibilizzatore organico, non metallico e biscationico, con un poliossometallato anionico e totalmente inorganico (Ru_4POM). Attualmente quest'ultimo rappresenta lo stato dell'arte dei catalizzatori molecolari per l'ossidazione dell'acqua. La PBI scelta, invece, è in grado di autoassemblarsi in acqua in una struttura monodimensionale; inoltre, questa PBI in stato eccitato rappresenta uno degli ossidanti fotogenerati più potenti, $E(PBI^{*2+/1+}) = 2.20$ V vs NHE. Grazie a interazioni elettrostatiche, essa è in grado di combinarsi con il Ru_4POM, formando un'architettura bidimensionale porosa ibrida, con dominii

organici-inorganici. Questa innovativa architettura supramolecolare mostra: i) una struttura supramolecolare ordinata; ii) veloci trasferimenti elettronici fotoindotti, in uno spazio temporale di 100 ps (nel sistema naturale questi avvengono nell'intervallo di 40 μs-1.6 ms); iii) attività ossigenica in soluzione acquosa neutra sotto irraggiamento con luce visibile (E. Pizzolato *et al.* "Perylene bisimides-oxygenic/polyoxometalates photosynthetic assemblies", manoscritto in preparazione) (**Capitolo 3**).

3) La fabbricazione di fotoanodi compositi, combinando il nanoibrido fotoattivo PBI/Ru_4POM con ossido di tungsteno nanocristallino (*nano*WO_3) come strato semiconduttore accettore di elettroni. Il fotoelettrodo mostra attività catalitica in seguito a illuminazione con luce visibile ($\lambda > 450$ nm) in una soluzione elettrolitica acida (pH 3). In particolare, la densità di fotocorrente massima è di 75 μA/cm^2 a 1.20 V vs NHE, mentre la resa quantica interna (APCE) del 1.30% risulta superiore rispetto al riferimento di letteratura di 0.8%, riportato per fotoelettrodi sensibilizzati con PBI e con IrO_2 come catalizzatore per l'evoluzione di ossigeno (**Capitolo 4**). Questi risultati aprono la strada a ulteriori miglioramenti, tra cui la decorazione della superficie dell'elettrodo semiconduttore al fine di aumentarne le prestazioni fotocatalitiche.

INDEX

Index

1 Introduction

1.1 The energy issue

The energy sector is one of the pillars of growth, competitiveness and development for modern economies. Now, humanity finds itself living through a period of profound change in the global energy landscape.[1] The major challenge of the 21st century is filling the gap between energy demand and supply with competitive, reliable and sustainable energy sources, considered essential for all advanced economies.

Independently from the energy sources that we are considering, the world has to deal with the increasing energy demand that is expected to grow every year. Between 1995 and 2013 global energy consumption passed from 9 billions toe (tons of oil equivalents; about 13 TW per year) to 13 billions toe (about 20 TW per year) (Fig 1.1). As reported in recent energy outlooks, the energy consumption rate is projected to double from the current value by 2050, and to triple by 2100, both as effect of the expected population growth and of the increased demand from the developing countries.[2–5]

Since now, the use of fossil fuels has represented the main energy resource, with 81.5% of our energy coming from them.[6,7] In 2013 more than 30% of worldwide gross consumption of energy was coming from petroleum and oil products, while solid fuels such as coal and lignite accounted for a slightly lower share, and just over one fifth of the total was gas; combined, these three fuels accounted for just over four fifths of global energy consumption (Fig. 1.1).

	1995	2000	2005	2010	2013	2013 (%)
Petroleum and Products	3372	3660	4007	4131	4210	31.1%
Solid Fuels	2208	2343	2950	3506	3928	29.0%
Gas	1807	2067	2352	2736	2902	21.4%
Renewables	1207	1290	1428	1664	1829	13.5%
Hydro*	213	225	252	296	326	2.4%
Geothermal*	39	52	54	65	66	0.5%
Solar/Wind/Other*	3	8	17	48	95	0.7%
Biofuels and Waste*	967	1025	1127	1287	1377	10.2%
Nuclear	608	676	722	719	646	4.8%
Other	17	22	22	33	40	0.3%
Total	9219	10057	11481	12789	13555	100.0%

Fig 1.1 A table resuming the global gross inland consumption in Mtoe (toe = tons of oil equivalents) between 1995 and 2013.[7]

One of the most prominent problem among the Earth's inhabitants is disparity due to fossil fuels use. As reported by the European Commission in their annual report,[7] the distribution of world energy production does not match with the gross inland consumption. Some regions of the world, like China, United States and Europe, produce less energy than they consume, while others, like Russia and Middle East, are energy exporters (Fig. 1.2). These differences in the energy dependence ratio lead to politic and economic issues due to the power of few countries holding the majority of the energy sources. Access to energy continues to divide the "haves" from the "have-nots". Globally, a large fractions of the world's population still lacks access to one or several types of basic energy services, including electricity, clean cooking fuel and an adequate means of transportation.[8]

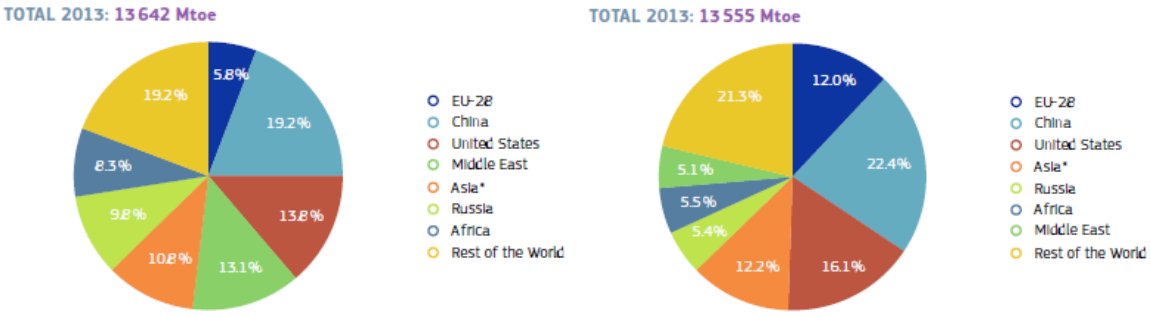

World energy production World gross inland consumption

Fig 1.2 Representation in pie charts of the world energy production divided by region (left) and world gross inland consumption divided by region (right) in 2013.[7]

There are two opposite school of thoughts related to the fossil fuels availability. Some report that the energy for the future will derive also from unconventional sources that were previously considered inaccessible due to high costs of extraction (such as natural gas).[9] Other report that civilization is going to face a problem that might change the energy landscape, the so-called oil peak.[10] In this scenario, there will come a time in which the supply will not be able to satisfy the ever increasing demand.

Then, even though the wide success of fossil fuels and their past appeal in technological advances, their exploitation has been under the spotlight due to a number of issues that have pushed energy up the political agenda, including the volatility of prices, interruptions to energy supplies, and increased attention to anthropogenic (human-induced) effects of energy use on climate change.

The overwhelming reliance on fossil fuels, in particular, threatens to alter the Earth's climate to an extent that could have severe consequences for the integrity of both natural and vital

human systems.[11] Indeed, during these years mankind has to face the problem of fossil fuels harmful effects, such as pollution that threatens human health, and the emission of greenhouse gases associated to global warming, which affects ecosystems.[12] The combustion activities for human purposes have injected in the air a small amount of carbon (about 7 Gt/year) if compared to the naturally occurring exchange between the biosphere and the atmosphere (about 200 Gt/year).[10] However, the concentration of CO_2 has steadily increased by 30% with respect to the industrial revolution levels and this is enough, on the long term, to alter the Earth's radiation balance and trigger artificial climate variations.

In conclusion, it is clear that humanity has to face an energy transition from fossil fuels to renewable energy sources, in order to avoid the above-mentioned issues. Any long-term solution relies on the identification and exploitation of alternative energy sources, ideally cheap, abundant, clean and widespread on Earth.

In 1912, the Italian photochemist Giacomo Ciamician proposed the exploitation of solar energy, recognizing its enormous potential as abundant, fairly distributed, carbon-neutral and clean source.[13] Every year the sun provides solar energy to our planet at a rate of 120000 TW. Therefore the energy from one hour of sunlight is equivalent to all the energy humankind currently uses in a year.[12,14]

Solar energy represents an appealing alternative for ensuring a suitable future, but since it is intermittent and diffuse, it requires to be captured, converted and stored. The most attractive way to energy conversion and storage is in the form of chemical bonds as Nature has acted for years with photosynthesis.

1.2 Natural Photosynthesis

Through billion years of evolution, Nature has devised a system to harness energy provided by the sun. Green plants are able to convert efficiently sunlight into chemically accessible energy by absorbing photons, to convert H_2O and CO_2 into O_2 and carbohydrates, the fuel of the plant (Eq. 1.1).

$$6\ H_2O + 6\ CO_2 + h\nu \rightarrow C_6H_{12}O_6 + 6\ O_2 \qquad (1.1)$$

Although in photosynthetic organisms, chlorophyll and other pigments are able to absorb the whole visible solar radiation, only the red part of the spectrum ($\lambda > 680$ nm, "red photons",

energy of about 1.8 eV)[14] is used to extract electrons and protons from water, to ultimately drive CO_2 reduction. These photosynthetic processes are performed thanks to the coupling of two photosystems in the membrane of thylakoids inside chloroplasts. The photosystem II (PSII) exploits light to permit the extraction of electrons/protons from water, while photosystem I (PSI) uses light in order to drive $NADP^+$ reduction to NADPH, that initiates then the CO_2 fixation process, in a dark step.

The first step in the photosynthetic machinery is the light absorption by the pigments. The energy is then funnelled to the enzyme PSII, which is composed by multiple subunit able to carry out the catalytic conversion of water into oxygen, protons and electrons, the so-called "water splitting reaction". In particular, the PSII complex is the reaction centre where the charge separation occurs. Its unit can stabilize the electron-hole pairs produced after light absorption converting the stored light energy into an electrochemical potential.[12,14] A chlorophyll molecule, P_{680}, is excited and is turned into a high oxidizing species, $P_{680}^{\cdot+}$, while the reducing equivalent is transferred along an electron chain to PSI, where the absorption of a second photon starts the $NADP^+$ reduction process (Fig. 1.3).

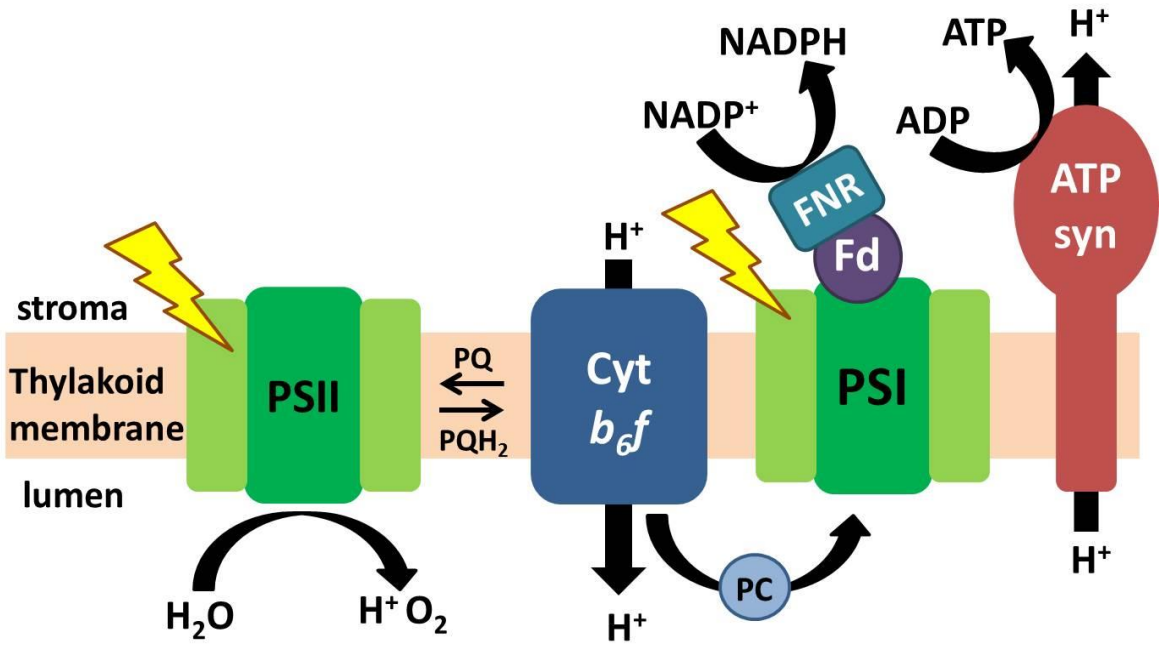

Fig. 1.3 Schematic representation of the thylakoid membrane showing the protein complexes involved in the photosynthetic light reactions.

These photosystems are highly efficient nanomolecular devices since the organisation of the electron carriers and other cofactors is optimized to facilitate the forward energy storing

reactions while minimizing the backward, unproductive and wasteful energy realising reactions. Even if several mechanistic aspects need to be defined, the study of the natural system has inspired the design of biomimetic systems that can work under an artificial environment.

1.2.1 The Photosystem II and the Oxygen Evolving Complex

Photosystem II (PSII) in oxygenic organisms is unique among photosynthetic reaction centers. It is the only known biological system capable of performing the photoinduced oxidation of water, one of the most thermodynamically demanding reactions in biological systems.[15] For this reason, it has been intensely studied by scientists trying to understand how the natural system works.

The PSII is a protein-pigment complex found in the thylakoid membranes of plants and internal membranes of cyanobacteria. Its core consists of a pseudo-symmetric heterodimer of two homologous proteins, D1 and D2 (Fig. 1.4).[16]

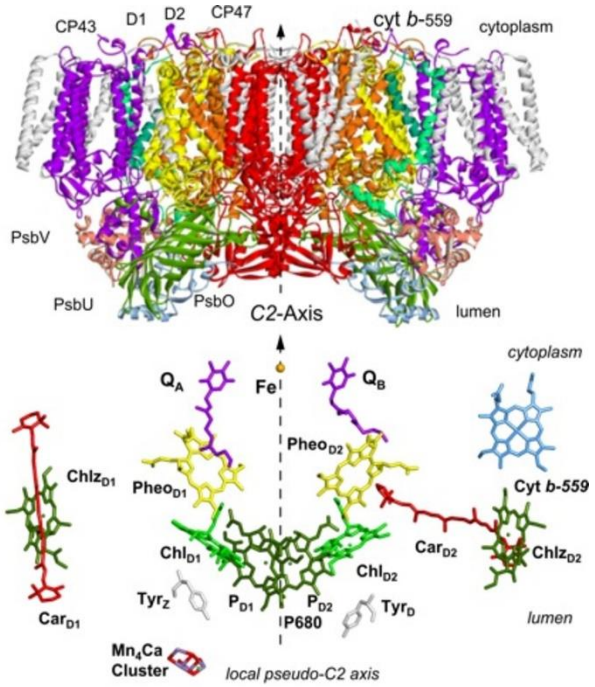

Fig. 1.4 Side view of the structure of PSII, the water splitting enzyme of photosynthesis. Below, the arrangement of the cofactors in the central D1/D2 proteins involved in charge separation, electron transport and water oxidation.

Unlike the reaction centers of all other photosystems which have a special pair of closely spaced chlorophyll molecules, within PSII the water oxidation reaction is triggered by the photochemical oxidation of a chlorophyll monomer, P_{680}, resulting in a charge separation (or electron-hole pairs) at the reaction center.[17] The oxidized form $P_{680}^{\cdot+}$ is a strong oxidant with an oxidation potential of *ca.* +1.2 V versus NHE (Normal Hydrogen Electrode),[18] and recovers the electron from the redox-active tyrosine, Tyr_z, which in turns oxidizes the Mn_4CaO_5 cluster in the oxygen-evolving complex (OEC), the real catalyst for water oxidation to oxygen. After four consecutive electron abstraction, the Mn_4CaO_5 cluster is regenerated by oxidizing two water molecules to produce O_2 and four protons (Eq. 1.2).

$$2\ H_2O \rightarrow O_2 + 4H^+ + 4e^- \qquad (1.2)$$

Due to its high efficiency (turnover frequency, TOF, up to 400 s^{-1}) and low overpotentials (η *ca.* 0.30 V),[16,19] the OEC is the ideal prototype for the development of artificial catalysts for water oxidation. X-ray crystallography has revealed that it is composed of a heteronuclear Mn_3CaO_4 cubane, bridging via oxide or hydroxide ligands to a dangling, fourth manganese atom (Fig. 1.5a).[20–28]

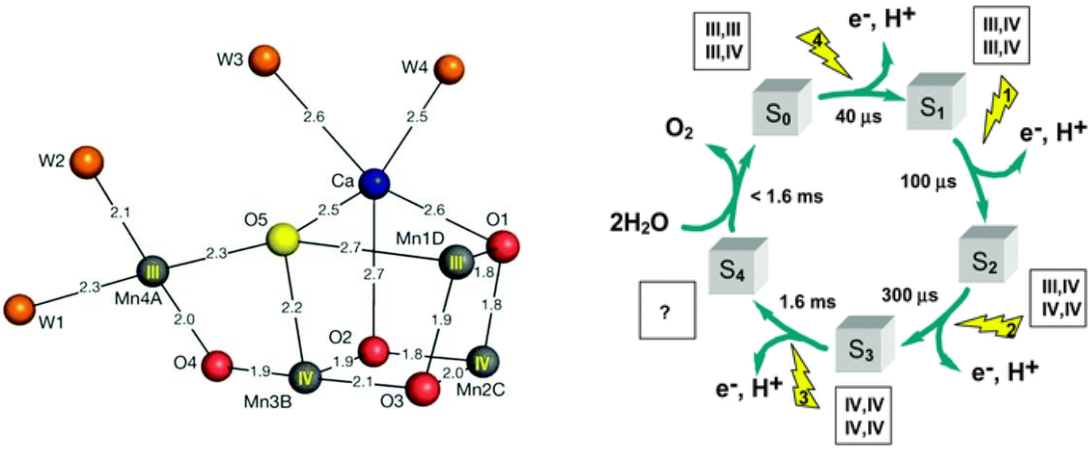

Fig. 1.5 a) Structural representation of the OEC;[21] **b)** S-state cycle of photosynthesis (Kok cycle).

This species is capable of oxidizing water with an impressive turnover frequency, defined as the number of oxygen molecules evolved per molecules of catalyst per unit of time, in the range 100-400 s^{-1}.[27] However, the structural changes of the OEC responsible for such efficiency and functionality along the catalytic cycle (Kok cycle, Fig. 1.5b),[29] have yet to be established at the molecular level.[30] During one turnover, the OEC is able to store the four oxidizing equivalents generated by light, leading to the stepwise formation of

intermediates commonly referred to as the S_n states (n = 0-4, depending on the degree of oxidation of the tetramanganese cluster). The sequential transitions from S_0 (the most reduced state) to S_4 (the most oxidized state) involve electrons and protons transfer events. These are mediated by the redox-active tyrosine residue, Tyr_Z, through the formation of a neutral radical, and a histidine residue, linked to the Tyr_Z by a hydrogen bond that permits the abstraction of a proton from the Tyr_Z, preventing the charge accumulation. Every oxidation step is then accompanied by a proton removal, in order to avoid the formation of high-energy intermediates that could lead to high activation energies. The short-lived S_4 state has accumulated step by step the four oxidazing equivalents, losing four protons.[31] This unstable intermediate is capable of oxidizing water in a single, four electron process, returning to the S_0 state and realising one oxygen molecule. Although the exact Mn oxidation states and the site of O-O formation in S_4 are still debated, the key feature of this catalyst is its impressive capability of working as a charge pool, accumulating the four oxidative equivalents and oxidizing water in a single concerted step, avoiding the high activation energy related to multistep mechanisms.

The success for the efficiency of PS II lies in the perfect organization of the supramolecular architecture and in the particular structure of the OEC. Nevertheless, even Nature finds the water oxidation reaction a difficult task: the OEC gets damaged during photosynthesis and must be resynthesized every half an hour due to the harsh oxidative conditions.[32]

Because of the high complexity of photosynthetic machinery, the mechanism by which water is oxidized in the natural photosystem is still actively studied with the view that further insight will be important for the design of artificial systems for solar energy-to-fuel conversion.[33]

1.3 Artificial Photosynthesis

Inspired by Nature, an artificial device can be designed to efficiently convert solar light into fuels, starting from clean and abundant raw materials. A practical approach would be to use solar energy to split water into molecular oxygen and hydrogen (Eqs. 1.2-1.4). This process requires the coupling of two half-reactions: (i) oxidation of H_2O to generate electrons, the reducing equivalents (Eq. 1.2) and (ii) reduction of protons to produce molecular hydrogen (Eq. 1.3).[18]

$$2\ H_2O \rightarrow O_2 + 4H^+ + 4e^- \quad (1.2)$$

$$4H^+ + 4e^- \rightarrow 2H_2 \quad (1.3)$$

$$2\ H_2O \rightarrow O_2 + 2H_2 \quad (1.4)$$

In order to occur, water splitting requires a complex architecture of functional modules, involving molecules and materials. With this aim, an artificial device has to hold the components to carry out all the steps taking place in the natural system, such as light absorption, energy and electron transfer and redox catalysis. A possible scheme for the artificial system is presented in Fig. 1.6 and consists of an antenna system, a photosensitizer, a donor-acceptor couple (reaction center) and two redox catalysts for oxygen and hydrogen evolution, respectively.[12]

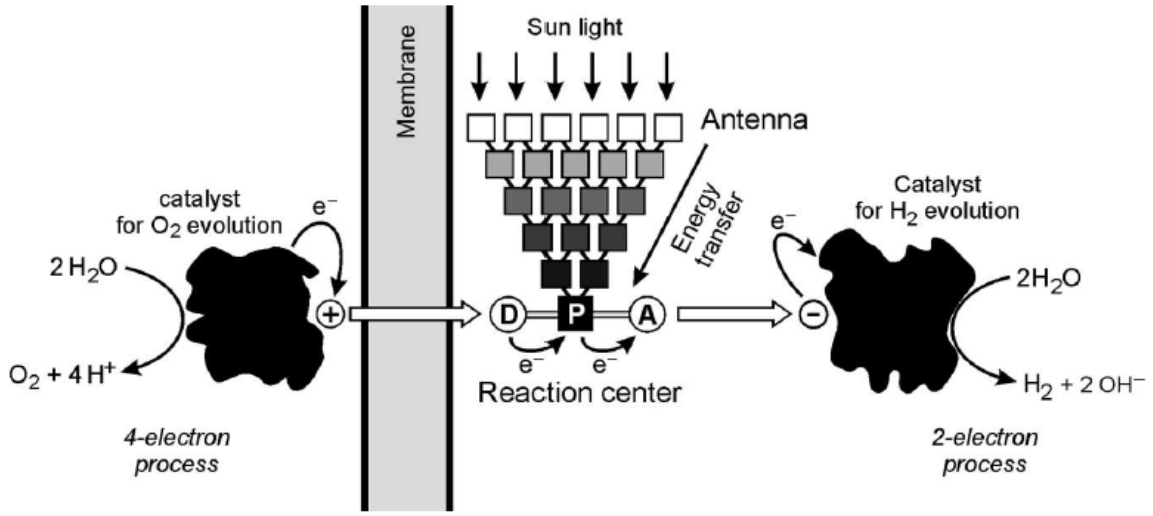

Fig. 1.6 Schematic representation of an artificial photosynthetic system for water splitting.[34]

The first step involves the absorption of light by the antenna system: it ideally consists of a variety of different chromophores in order to (i) maximize the absorption of solar radiation in the range from UV to IR and to (ii) transfer efficiently the energy to the photosensitizer (P) (Eq. 1.5). In its excited state, the photosensitizer induces an electron transfer from a suitable donor (D) to an acceptor (A), leading to an overall charge separation (Eqs. 1.6-1.7):

$$D - P - A \rightarrow D - P^* - A \quad (1.5)$$

$$D - P^* - A \rightarrow D - P^+ - A^- \rightarrow D^+ - P - A^- \quad (1.6)$$

$$D - P^* - A \rightarrow D^+ - P^- - A \rightarrow D^+ - P - A^- \quad (1.7)$$

This is the crucial part of the artificial process, since the charge separation has to last as long as possible in order to trigger the two redox reactions, avoiding unproductive recombination.[35]

Then, electrons are transferred from A^- to a reduction catalyst, cat_{red}, to promote the reduction of protons to hydrogen (two-electron process) (Eqs. 1.8-1.9), while the holes are transferred from D^+ to an oxidation catalyst, cat_{ox}, to promote the oxidation of water to oxygen (four-electron process) (Eqs. 1.10-1.11).

$$2A^- + cat_{red} \rightarrow 2A + cat_{red}^{2-} \quad (1.8)$$

$$cat_{red}^{2-} + 2H^+ \rightarrow cat_{red} + H_2 \quad (1.9)$$

$$4D^+ + cat_{ox} \rightarrow 4D + cat_{ox}^{4+} \quad (1.10)$$

$$cat_{ox}^{4+} + 2H_2O \rightarrow cat_{ox} + O_2 + 4H^+ \quad (1.11)$$

Due to the high complexity of this physical and chemical processes, current research activity focuses on the optimization of molecular components as independent building blocks, including antennae, photosensitizers and catalysts, together with their arrangement within nano-structured environments, in order to define geometry, morphology and surface properties of the resulting photosynthetic systems.[36]

The most challenging issue is the design of efficient catalysts for the two redox reactions. In particular, a good redox catalyst has to: (i) accumulate the reduction or oxidation equivalents in order to interface the one-electron charge separation with the multi-electronic reactions, (ii) be fast enough to prevent charge recombination and (iii) be robust in the long term, since an artificial system has not the possibility of restoring its components, as the natural system does.

While several catalytic systems for hydrogen evolution have been already reported to efficiently perform the two-electron reduction process,[37] the development of catalysts for the four-electron water oxidation to oxygen has been less investigated. Indeed, this latter process is still recognized as the bottleneck of the overall water splitting reaction.[32]

1.4 The Water Oxidation reaction

During last years, scientists have focused their attention on the oxidation of water to oxygen and many efforts have been made both in the development of new catalysts and in the comprehension of the reaction mechanism.[38] The issues related to this process are:

- thermodynamic: the standard potential for the half reaction in Eq. (1.2) is 1.23 V versus the normal hydrogen electrode (NHE), and it depends on the pH according to Eq. (1.12):

$$E = (1.23 - 0.059 \times pH)\ V\ vs\ NHE \qquad (1.12)$$

- kinetic: it implies high activation energy barriers and slow rates, since it is a complex reaction involving the simultaneous removal of four electrons and four protons from two water molecules together with the formation of a new oxygen-oxygen bond.

In an artificial system, the thermodynamic potential is supplied by the charge separation induced by the light absorption; a catalyst is then needed to overcome the kinetic issue.

1.5 Overview of common catalytic systems

Many complementary methods are used to evaluate the performance of water oxidation catalysts. Among these, the most used are photochemical, electrochemical and photoelectrochemical methods. Although the conditions employed do not mimic exactly the environment of a photosynthetic cell, using these different approaches enables the rapid screening of the catalysts.[18,39]

1.5.1 Photocatalytic systems

In a photocatalytic system, the oxidant species is generated *in situ*, after absorption of light by a suitable photosensitizer. In particular, a three-component system consisting of water oxidation catalyst (WOC)/photosensitizer (PS)/sacrificial electron acceptor (SEA) is commonly used. The role of the SEA is the replacement of the reduction half reaction by an easier and faster redox reaction.

For WOCs screening, $[Ru(bpy)_3]^{2+}$ (bpy = 2,2'-bipyridyl) is usually exploited as photosensitizer together with sodium persulfate, $Na_2S_2O_8$, as SEA[40] (alternatively, $[Co(NH_3)_5Cl]^{2+}$ has been exploited as SEA).[39,41]

After light absorption (Eq. 1.13), the excited state of the photosensitizer, $[Ru(bpy)_3]^{2+*}$, undergoes an oxidative quenching by $S_2O_8^{2-}$, producing $[Ru(bpy)_3]^{3+}$, a sulfate anion (SO_4^{2-}) and a sulfate radical ($SO_4^{\bullet-}$) (Eq. 1.14). The sulfate radical is a strong oxidant ($E^0 > 2.40$ V vs NHE), capable of directly oxidizing a second $[Ru(bpy)_3]^{2+}$ molecule to $[Ru(bpy)_3]^{3+}$ (Eq. 1.15). Four equivalents of photogenerated $[Ru(bpy)_3]^{3+}$ are then able to oxidize the WOC (Eq. 1.16); it is important to note that also the sulfate radical may oxidize the WOC (Eq. 1.17). Finally, after the accumulation of four holes, the WOC in this active state, WOC^{4+}, is able to oxidize water (Eq. 1.18).

$$PS + h\nu \rightarrow PS^* \quad (1.13)$$

$$PS^* + S_2O_8^{2-} \rightarrow PS^+ + SO_4^{2-} + SO_4^{\bullet-} \quad (1.14)$$

$$PS + SO_4^{\bullet-} \rightarrow PS^+ + SO_4^{2-} \quad (1.15)$$

$$4PS^+ + WOC \rightarrow 4PS + WOC^{4+} \quad (1.16)$$

$$WOC + SO_4^{\bullet-} \rightarrow WOC^+ + SO_4^{2-} \quad (1.17)$$

$$WOC^{4+} + 2H_2O \rightarrow WOC + O_2 + 4H^+ \quad (1.18)$$

In order to preferentially promote the direct quenching of the photosensitizer by the persulfate, and to prevent unproductive quenching by the WOC, it is essential to conduct the photocatalytic experiments with a significantly higher concentration of the photosensitizer than the WOC.[18,42] Low concentrations of the WOC limit also competitive absorptions of photons.

1.5.2 Electrochemical systems

Electrochemical methods are often used for the screening of catalysts. In particular, cyclic voltammetry (CV) and controlled potential electrolysis (CPE) are the most used techniques to obtain the catalytic parameters related to the performance of the involved systems.[43,44]

CV is an electroanalytical technique in which the current passing at the surface of an electrode immersed in a solution of the redox-active species (alternatively, the redox-active species can be grafted on the electrode) is measured against an applied potential. This technique requires a three-electrode cell with a working electrode (WE), a reference electrode (RE) and a counter electrode (CE). In the WE, the reaction of interest is occurring,

the RE has a stable and well-known electrode potential, to whom the potential measured at the WE is referred to, and the CE is used to close the current circuit with a reverse redox reaction.

During the experiment, at the WE the potential is ramped linearly versus time, reaching a maximum value and then switched in the opposite direction to return to the starting value; these steps can be repeated several times. To obtain a voltammogram, the current recorded at the WE is reported against the potential.

During CPE experiments, the potential at the WE is maintained constant over time and the response of the system is obtained as current and charge passed at the electrode as a function of time. With this technique, the stability of the catalyst can be evaluated and, in the case of water oxidation, it is often combined with oxygen measurement.

1.5.3 Photoelectrocatalytic systems

The coupling of electrochemical techniques with the light-induced water oxidation is at the basis of photoelectrochemistry. Its relevance lies in the combination of multiple processes, from light absorption to charge separation and electron transfers, in a single heterogeneous device.

During a photoelectrochemical experiment at the WE, normally a semiconductor (SC), the current due to a charge separation induced by light absorption (photocurrent) is recorded. In this case, the catalysts can be in the homogeneous phase or anchored onto the electrode surface. The second approach is a step further towards the incorporation of the WOC in a photoelectrochemical cell (see section 1.7). Moreover, it may ensure the stability of the WOC through its heterogenization, enhancing also its activity towards water oxidation. Different methods can be used to anchor WOCs on a conducting surface:[39] (i) physisorption, exploiting van der Waals forces, (ii) electrostatic interactions, exploiting the different charges between the surface and the WOC, (iii) encapsulation, i.e. immobilization of the WOC inside a matrix, and (iv) chemisorption, linking covalently the WOC to the surface. In this last case, the catalyst is usually modified by the introduction of functional groups such as carboxylate (-COO-) or phosphonate (-$PO(OH)_2$) groups.[45,46]

1.5.4 Parameters for evaluation of catalyst performance

From the different techniques described above, it is possible to extract useful parameters for the evaluation of the performance of catalysts. It is essential to underline that these techniques can provide complementary information about the system under investigation. Since a large variety of experimental conditions can be found in current literature, it is often difficult to compare directly different systems; hence, it is important to report the catalyst performance parameters together with the employed conditions.
For a photocatalytic system, the most used evaluation parameters are:

- the **turnover number** (TON) refers to the ratio between the moles of product (O_2 in the case of water oxidation) per mole of catalyst used;
- the **turnover frequency** (TOF) refers to the TON per unit of time, and is related to the rate of catalytic activity;
- the **chemical yield** refers to the ratio between the moles of product per mole of sacrificial agent used. In these systems, this parameter is important since the quantity of sacrificial agent can limit the efficiency of the whole process;
- the **quantum yield** (QY) refers to the ratio between the moles of O_2 per mole of absorbed photons.

In an electrochemical system, useful parameters to consider are:[43,44,47–49]

- the **overpotential** (η): it is the additional potential needed to drive a redox reaction at a specific rate, over the thermodynamic requirement. It is often reported as the difference between the applied potential and the standard potential of the considered redox reaction;
- the **onset potential**: it is the applied potential at which starts the catalytic process;
- the **turnover frequency** (TOF) refers to the ratio between the moles of product evolved per mole of catalyst per unit of time. In electrocatalytic experiments, this parameter depends on the applied potential, while the TOF_0, the TOF extrapolated at overpotential equal to 0, has been recently proposed as universal parameter to compare the different systems;
- the **turnover number** (TON) refers to the ratio between the moles of product evolved per mole of catalyst, and is typically obtained in electrolysis experiments;
- the **Faradaic efficiency**: it is used in CPE experiments and, in the case of water oxidation, it is defined as the ratio between the actual oxygen evolved during the

experiment and the theoretical value calculated from the Faraday's law of electrolysis (Eq. 1.19):

$$n = \frac{Q}{z \cdot F} \tag{1.19}$$

where n is the theoretical value of moles of oxygen produced, Q is the charge passed through the electrode during electrolysis, z is the number of electrons involved in the redox reaction ($z = 4$ in the case of water oxidation) and F is the Faraday's constant (96485 C mol^{-1}).

In addition to electrocatalytic parameters, for a photoelectrochemical experiment, other parameters are:

- the **incident photon-to-current efficiency** (IPCE) refers to the ratio between the flux of electrons, Φ_{e^-}, flowing in the circuit and the incident photons, Φ_{ph}, per cent (Eq. 1.20):

$$IPCE_\lambda = \frac{\Phi_{e^-}}{\Phi_{ph}} \cdot 100 = \frac{J_\lambda \cdot 10^{-2} / F}{J_\lambda / N_A \cdot E_\lambda} \cdot 100 \approx 1240 \cdot \frac{J_\lambda}{\lambda \cdot I_\lambda} \tag{1.20}$$

where J_λ is the steady state photocurrent density at a certain value of λ, F is the Faraday constant, I_λ is the irradiance defined as the irradiated power at λ per unit area, N_A is Avogadro's number and $E_\lambda = hc/\lambda \times 10^{-9}$ is the energy of a photon of wavelength λ. The IPCE refers to the percentage of incident photons that are converted to electric current and it is often reported as external quantum efficiency (EQE).

- the **absorbed photon-to-current efficiency** (APCE) refers to the ratio between the flux of electrons flowing in the circuit and the absorbed photons per cent. It is calculated from the IPCE value and the light harvesting efficiency (LHE), extrapolated from the UV-Vis spectra of the samples (Eq. 1.21)

$$APCE_\lambda = \frac{IPCE_\lambda}{LHE_\lambda} = \frac{IPCE_\lambda}{1 - T(\lambda)} = \frac{IPCE_\lambda}{1 - 10^{-A(\lambda)}} \tag{1.21}$$

where $T(\lambda)$ is the transmittance and $A(\lambda)$ is the absorbance at λ. This parameter is often reported as the internal quantum efficiency (IQE).

1.6 State of the art: photosensitizers and WOCs

Due to the complexity of the processes involved in water oxidation, the optimization of the single molecular units of the artificial photosynthetic machinery is required, and in particular in the three-component system described above (Eqs. 1.13-1.18).

Suitable photosensitizers for water oxidation must have (i) strong absorbance (ideally $\varepsilon > 10^4$ M^{-1} cm^{-1}) in a broad range of the visible region (380-700 nm), (ii) long-lived excited states at room temperature and (iii) high oxidation potential to oxidize the WOC to its active state.[39]

After light absorption, PS* has to undergo a fast and efficient electron transfer to the SEA, leading to the formation of PS^+ and SEA^-. A possible competitive reaction can be the radiative or non-radiative emission of PS*. For this reason, a long excited state lifetime is required.[50] Finally, the oxidation potential of PS^+ must be suitable to allow the subsequent oxidation of the catalyst. In other words, it has to be higher than the potential of the couple $WOC^{n+}/WOC^{(n-1)+}$. Then, since the redox potential for oxidizing water is 1.23 V vs NHE, the potential of the WOC^{4+}/WOC^{3+} couple must be more positive than this value. This means that 1.23 V vs NHE represents the lower potential limit (note that the redox potential for the O_2/H_2O couple is pH-dependent, Eq. 1.12). Another important requirement for the WOC is the ability to accumulate four oxidizing equivalents, managing multi-electron transfers in a narrow potential range. This is facilitated in systems in which the electron transfer events are coupled with proton transfers. This so-called proton-coupled electron transfer (PCET) ensures redox levelling through charge neutralization. Without PCET, the energy of subsequent electron transfer events would increase dramatically, preventing the catalysis.[51]

Furthermore, WOCs must be stable under oxidative conditions. Ideally, for a commercially viable solar fuel generating device, they have to last for at least 10^8 turnovers, but no known catalyst (either biological or synthetic) has so far this stability.[52]

Finally, the WOC must be fast and selective, and suitable for the coupling with the PS unit maintaining its features described above.

1.6.1 Photosensitizers

The main photosensitizers used in photocatalytic water oxidation and their features are reported in Table 1.1.

Table 1.1 Overview on the optical and electrochemical properties of the PS.

Photosensitizer	λ_{max}, [nm] (ε, M^{-1} cm^{-1})	λ emission, [nm]	Lifetime of excited state, [ns]	E PS^+/PS, [V vs NHE]
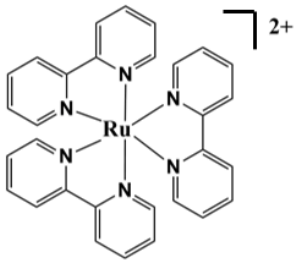 $[Ru(bpy)_3]^{2+}$	450 (1.4×10^4)	602 (triplet)	630 (triplet)	1.26
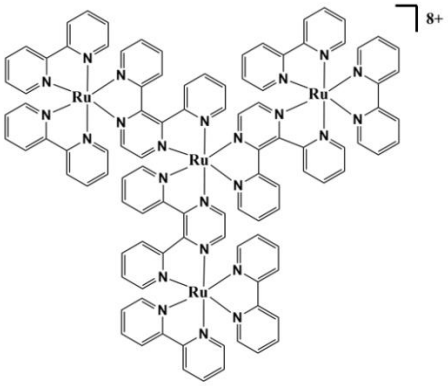 $\{Ru[(\mu\text{-dpp})Ru(bpy)_2]_3\}^{8+}$	545 (4.6×10^4)	780 (triplet)	30 (triplet)	1.70
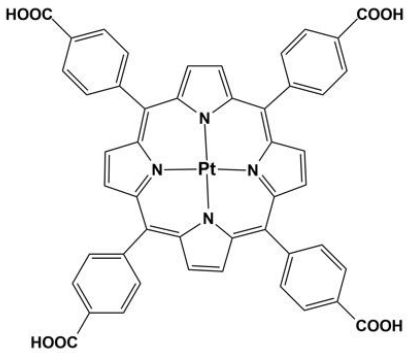 Pt(II)-TCPP	395 (B-band, $2.1x10^5$), 511, 542 (Q-bands, 1.7×10^4, 2.7×10^3)	681 (triplet)	2200 (triplet)	1.42

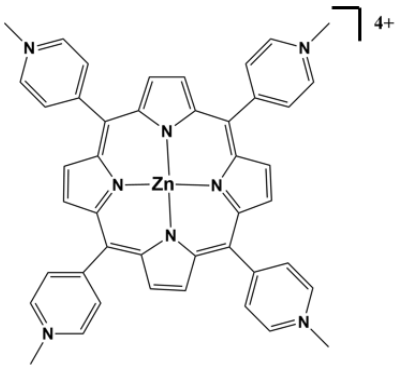 Zn(II)TMePyP^{4+}	430 (B-band), 575, 620 (Q-bands)	633, 665 (singlet)	1.3 (singlet) 3200 (triplet)	1.18

$[Ru(bpy)_3]^{2+}$ has been extensively used as photosensitizer. It has an absorption band with λ_{max} at 450 nm corresponding to a metal-to-ligand charge transfer (MLCT) d $\rightarrow \pi^*$ transition. The excited state is a triplet MLCT (^{3}MLCT) with an energy of about 2.12 eV, a lifetime of 630 ns and a luminescent quantum yield of 0.028.[50] These properties reveal slow decaying processes leading to the ground state of $[Ru(bpy)_3]^{2+}$, giving the possibility of involving the ^{3}MLCT state in many efficient electron transfer processes. Moreover, the oxidation potential of the $[Ru(bpy)_3]^{3+/2+}$ couple in aqueous solution is +1.26 V vs NHE, fulfilling the requirement (iii) described above.

Multinuclear Ru(II) dendrimers have been also presented for their use as photosensitizers,[53] since they offer several advantages over $[Ru(bpy)_3]^{2+}$. In particular, $\{Ru[(\mu\text{-dpp})Ru(bpy)_2]_3\}^{8+}$ (dpp = 2,3-bis(2-pyridyl)pyrazine) has been used in a photoactivated system for water oxidation.[50,54,55] It is based on Ru(II) metal centers with bpy as peripheral ligands and dpp as bridging ligands. This complex presents an absorption spectrum more extended in the visible region (up to 700 nm), with respect to $[Ru(bpy)_3]^{2+}$, that matches better with the solar emission (Fig. 1.7). The low-energy absorption band maximizing at 545 nm is due to MLCT transitions involving both the bpy and the dpp ligands as acceptor. The excited state emits at about 780 nm, has a lifetime of 30 ns in aqueous solution and a quantum yield of 0.002. The redox potential of the $\{Ru[(\mu\text{-dpp})Ru(bpy)_2]_3\}^{9+/8+}$ couple is +1.70 V vs NHE, about 440 mV higher than the oxidation potential of $[Ru(bpy)_3]^{2+}$. This makes the Ru(II) dendrimer more effective in extracting electrons from the various redox state of the catalyst than the $[Ru(bpy)_3]^{2+}$.

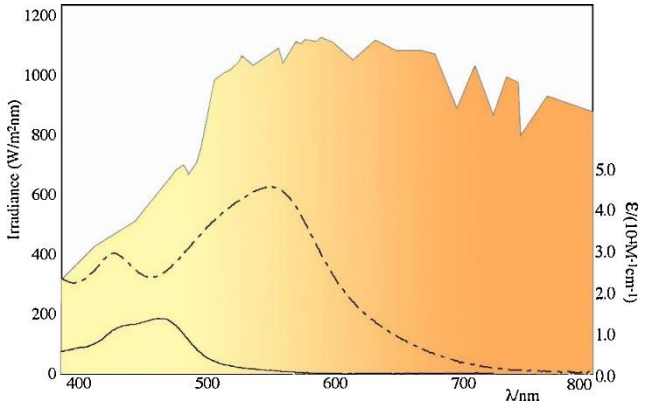

Fig. 1.7 Absorption spectra of $[Ru(bpy)_3]^{2+}$ (solid line), of the Ru(II) dendrimer (dotted-dashed line) and their comparison with the solar spectrum at the sea level (orange area).[50]

Taking inspiration from the natural system, metalloporphyrins have also been reported as photosensitizers for light-driven water oxidation, thanks to their broad spectral absorption and high long-lived excited states in solution. However, their one-electron oxidation potential is similar, or in some cases lower, to that of $[Ru(bpy)_3]^{2+}$. For this reason, their application is limited to low-overpotential WOCs or to high pH media.[56] Nevertheless, the modification of the ligand structure can increase the redox potential, making them suitable for the coupling with a wider range of WOCs.[57]

Recently, a tetracarboxylic acid Pt(II) porphyrin (Pt-TCPP, TCPP = tetrakis(4-carboxyphenyl)porphyrin) has been tested in combination with Ir- and Co-based catalysts.[56] This species has a longer triplet-state lifetime than the $[Ru(bpy)_3]^{2+}$ (2200 vs 630 ns), and is water-soluble, since the carboxylic groups are deprotonated in neutral aqueous solution.

Also a Zn(II) porphyrin (Zn-TMePyP^{4+}, TMePyP = tetramethylpyridylporphyrin) has been reported for photocatalytic water oxidation.[58] Its polycationic nature makes it conveniently soluble in aqueous solution and provides a redox potential for the Zn-TMePyP$^{5+/4+}$ couple of 1.18 V vs NHE, suitable for water oxidation at high pH. Also in this case, the triplet-state lifetime is longer than that of $[Ru(bpy)_3]^{2+}$ (3200 vs 630 ns).

The optimization of photosensitizers and antenna systems as independent building blocks paves the way to the research of the suitable candidate able to meet the needs of the light-driven water oxidation process, with the aim to activate the WOC.

1.6.2 Molecular WOCs

In the past years, several catalysts, both homogeneous (molecular catalysts)[42,59] and heterogeneous (mainly metal oxides catalysts),[60–63] have been reported for their application in photoactivated catalytic processes. Molecular WOCs are particularly appealing thanks to their unique features: (i) their properties are potentially tunable by molecular design;[33] (ii) they can overcome metal oxides performance, reaching outstanding activity; (iii) the understanding of the reaction mechanism can be facilitated by the molecular system; (iv) in a light-driven process, the interaction between the molecular WOC and the PS can be easily controlled.[64–66]

An open issue in the use of molecular WOCs is whether they are the real catalysts involved in the reaction or the precursor of the actual active species. Indeed, due to the strongly oxidative conditions related with water oxidation process, the WOCs can possibly undergo to irreversible transformations, involving the formation of metal or metal oxides, in the forms of colloids, films or powders.[67,68] For this reason, it is fundamental to understand the evolution of the system during the catalytic reaction through an accurate study and characterization of the species.

The state-of-the-art of molecular WOCs will be presented, considering the most attractive examples of tetrametallic and of earth abundant single site molecular WOCs.

1.6.2.1 Tetrametallic molecular WOCs

The most evident feature of the natural OEC in the PSII is the presence of four transition metal centers, able to sequentially accumulate the four oxidizing equivalents needed to drive water oxidation. For this reason, in recent years attention has been focused on the development and testing of tetrametallic molecular WOCs.

An important family of WOC considered for light-driven water oxidation is the one bearing a totally inorganic class of ligands: the polyoxometalates (POMs) (Fig. 1.8).[42] These are molecular metal-oxo clusters of early transition metals in their highest oxidation state (V^{V}, Nb^{V}, Ta^{V}, Mo^{VI}, W^{VI}) and therefore inert to oxidation. This is a key aspect since they can confer robustness to the whole molecular structure under the harsh oxidative conditions of catalysis. However POMs are sensitive to pH conditions that have to be controlled in order to avoid hydrolytic degradation, particularly favored in alkaline environment. For this

reason, the optimization of the pH conditions, the ionic strength and the counter ion nature is required to boost the catalytic efficiency of POMs.

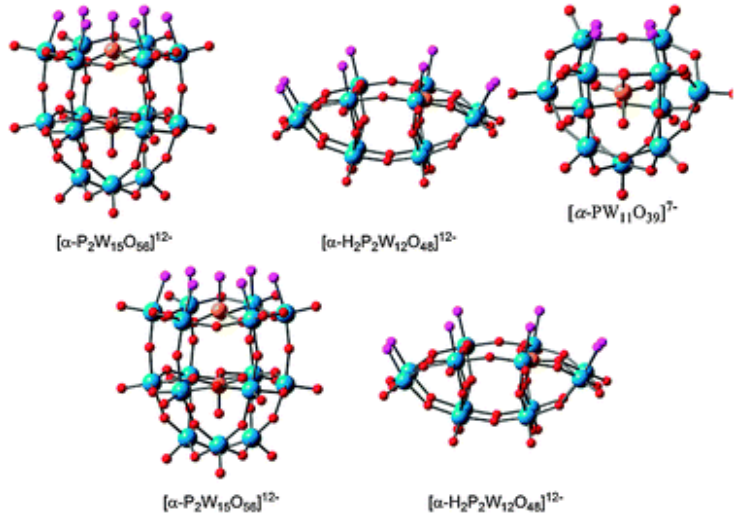

Fig. 1.8 Structures of polyoxometalate (POM) ligands. Light blue: tungsten; red: oxygen; purple: oxygen atoms of the coordination site.[42]

Other key features of POMs are: (i) their capability of coordinating catalytically active transition metal centers;[69,70] (ii) the polyanionic charge that allows the solubility in a wide range of solvents, depending on the nature of the counter ion; (iii) the few-nanometer dimensions.

In 2008, a breakthrough in the field of WOCs employing POMs ligand was achieved. A tetra-ruthenium compound obtained from the lacunary POM $[\gamma\text{-}SiW_{10}O_{36}]^{8-}$ was reported simultaneously by two research groups.[71,72] The resulting species $\{Ru^{IV}_4(\mu\text{-}O)_4(\mu\text{-}OH)_2(H_2O)_4[\gamma\text{-}SiW_{10}O_{36}]_2\}^{10-}$ (Ru_4POM) displays an adamantane-like structural motif of the ruthenium-oxo core, reminiscent of the natural OEC (Fig. 1.9).

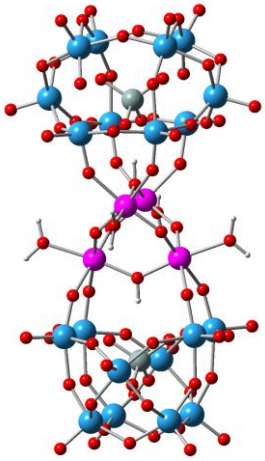

Fig. 1.9 Structure of the $\{Ru^{IV}_4(\mu\text{-}O)_4(\mu\text{-}OH)_2(H_2O)_4[\gamma\text{-}SiW_{10}O_{36}]_2\}^{10-}$, Ru_4POM. Light blue: tungsten; red: oxygen; grey: silicon; purple: ruthenium.[71]

Ru_4POM turned out to be active towards water oxidation in photocatalytic experiments in the presence of $[Ru(bpy)_3]^{2+}$ as PS and $Na_2S_2O_8$ as SEA, where it shows outstanding performance. In neutral solution (phosphate buffer, pH 7) and under visible light irradiation, Ru_4POM reaches 350 TONs, while oxygen production is limited by the oxidative decomposition of the $[Ru(bpy)_3]^{2+}$.[54,73,74] The interaction between PS and WOC has indeed a huge impact on the efficiency of the catalytic process. In this case, by laser flash photolysis experiments it is possible to follow the electron transfer (ET) dynamics occuring in the PS/WOC system in order to understand the reaction mechanism and to further optimize the system. In such experiment, ET from photogenerated $Ru(bpy)_3^{3+}$ to Ru_4POM occurs with a second-order rate constant of 3.6×10^9 M^{-1} s^{-1},[75] confirming that the molecular Ru_4POM, in this case, is superior to some of the best collodail catalysts (e.g. IrO_x, for which values of the order of 10^6 M^{-1} s^{-1} have been reported).[76] This fast hole scavenging of the Ru_4POM towards $[Ru(bpy)_3]^{2+}$ is crucial to minimize the decomposition of the PS.

As observed in CV experiments, Ru_4POM is capable of undergoing consecutive one-electron oxidations through PCET,[77,78] in analogy with the natural OEC. Several redox events associated to oxidation of the Ru^{IV} centers to higher oxidation states occur, until the species reaches the active form capable of oxidizing water. The electrochemical experiments show an overpotential (η) for the Ru_4POM in the range 0.20-0.35 V, depending on the pH.[71,72] This value is comparable to the estimated overpotential for the natural complex (η of *ca.* 0.3-0.4 V at physiological pH),[79] making Ru_4POM one of the most efficient WOCs presented in literature and suitable for the combination with a wide range of PS.

The electrochemical features and activity of Ru_4POM are maintained when supported onto nanostructured materials,[80–82] exploiting its polyanionic nature.

Due to the low availability (1.0×10^{-3} ppm)[79] and high cost of ruthenium, other POM WOCs containing earth abundant first row transition metals, in particular cobalt and manganese, have been recently proposed.

Cobalt is known to be catalitically active since early 80s,[83] while the $[Co_4(H_2O)_2(\alpha\text{-}PW_9O_{34})_2]^{10-}$ (Co_4PW_9) was proposed by Hill and co-workers as the first carbon-free homogeneous catalyst containing abundant metals (Fig. 1.10).[84] Also in this case, a tetracobalt core is the active site of the molecule, constituted by four redox metal centers linked by μ-oxo briges.

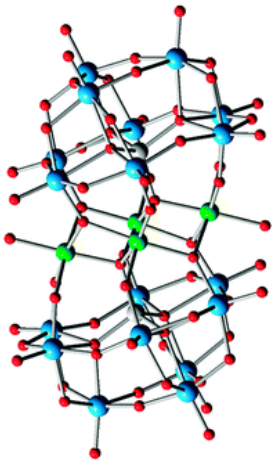

Fig. 1.10 Structure of the $[Co_4(H_2O)_2(\alpha\text{-}PW_9O_{34})_2]^{10-}$, Co_4PW_9. Light blue: tungsten; red: oxygen; grey: phosphorus; green: cobalt.[84]

In photocatalytic experiments using the $[Ru(bpy_3]^{2+}/Na_2S_2O_8$ system, oxygen is evolved by Co_4PW_9 with TONs up to 220 in borate buffer at pH 8.[85] Even if authors proved the stability of the species in the photoactivated system, under electrochemical conditions the molecular structure of the Co_4PW_9 is no more preserved, due to the deposition of an amorphous film of CoOx, which becomes the major active catalyst.[86]

Inspired by the natural OEC, a step forward in the design of earth abundant molecular WOCs is represented by the use of manganese. Besides its natural abundance and its low cost, it is also environmentally benign and, furthermore, its large redox chemistry allows the access to a wide range of oxidation states with strong oxidizing power. Unfortunately, this is associated with an intrinsic instability of these high-valent species, requiring their stabilization with suitable ligands in order to prevent their decomposition. These ligands

should also be robust and stable scaffold against oxidative degradation, due to the strong oxidizing power of these manganese species.

Recently, Bonchio and co-workers presented a tetramanganese species stabilized by a hybrid organic-inorganic set of ligands, the $[Mn^{III}_3Mn^{IV}O_3(CH_3COO)_3(A\text{-}\alpha\text{-}SiW_9O_{34})]^{6-}$ (Mn_4POM) (Fig. 1.11).[87]

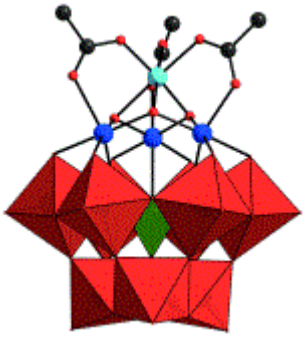

Fig. 1.11 Structure of the $[Mn^{III}_3Mn^{IV}O_3(CH_3COO)_3(A\text{-}\alpha\text{-}SiW_9O_{34})]^{6-}$, Mn_4POM. Dark grey: carbon; red: oxygen; blue: manganese(III); light blue: manganese (IV); green polyhedron: SiO_4; red polyhedra: WO_6.[87]

This molecular WOC has remarkable structural similarities with the natural OEC in the S_0 state. Moreover, the presence of acetate ligands helps the access and stabilization of Mn high oxidation states needed for the catalysis. In CV experiments, under oxidative scan an anodic wave is observed at +1.07 Vvs NHE, related to a three-electron oxidation of the Mn core ($Mn^{III}_3 \rightarrow Mn^{IV}_3$), and a following intense catalytic wave at +1.45 V vs NHE is ascribed to water oxidation, establishing an overpotential of 0.53 V for Mn_4POM. This WOC has also been tested in a photoactivated system with $[Ru(bpy)_3]^{2+}/Na_2S_2O_8$ in $NaHCO_3/Na_2SiF_6$ buffer (pH 5.2). The catalyst evolves oxygen showing TOF up to 2.84×10^{-3} s^{-1} and TON of ca. 5.2. Also in this case, oxygen production is limited by the irreversible bleaching of the photosensitizer which occurs upon continuous irradiation and was confirmed by the UV-Vis analysis of the used reaction mixture. From laser flash photolysis studies, the evidence for the occurance of three fast electron transfers (within 50 ms) from Mn_4POM to photogenerated $[Ru(bpy)_3]^{3+}$ has been reported. This further similarity with the natural OEC, where three fast oxidations (within 300 μs) occur in the Kok cycle from the S_0 to the S_3 state, paves the way for a deeper investigation on the high potentiality of such WOC.

1.6.2.2 Single site WOCs

In close analogy with the natural OEC, remarkable efforts have been made towards the development of multinuclear transition metal complexes. Indeed, multimetallic catalysts could in principle distribute the four oxidizing equivalents needed for water oxidation over several metal centers, thus lowering the energy barrier of the overall catalytic process. It was then believed that single metal site catalysts were not able to reach the different redox states at the suitable potential to be involved in the catalytic cycle. Conversely, they have been recently proposed as WOCs, with a proposed mechanism for O-O bond formation involving in most cases a water nucleophilic attack to a metal-oxo group. In this way, the oxidation state of the metal center is lowered by the water attack to the high-valent M-O intermediate, reducing the number of oxidation states of the metal needed for the catalytic cycle.

An example is the ruthenium sigle site complex, proposed by Sun and co-workers, $[Ru^{II}(bda)(isoq)_2]$ (H_2bda = 2,2'-bipyridine-6,6'-dicarboxylic acid; isoq = isoquinoline) (Fig. 1.12).[88–90] This study underlines some insight into the mechanism in the presence of a sacrificial oxidant, which requires a bimolecular event involving two water molecules for the formation of the O-O bond.

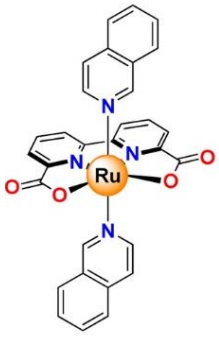

Fig. 1.12 Structure of the mononuclear ruthenium complex $[Ru^{II}(bda)(isoq)_2]$.[88]

Moreover, under photochemical activation with the $[Ru(bpy)_3]^{2+}/Na_2S_2O_8$ system, it shows a TOF of 0.31 s^{-1}, together with a high stability (TON = 218).[91]

Also in the case of single site WOCs, earth abundant transition metals of the first row have been employed, in particular cobalt, iron and copper, due to their availability and low costs. In 2013, Groves and co-workers have reported a series of single site Co^{III} porphyrins able to act as electrochemical WOCs in neutral pH (Fig.1.13a).[92] In particular, the Co^{III}-5,10,15,20-tetrakis-(1,3-dimethylimidazolium-2-yl)porphyrin with a highly electron-deficient ligand was found to be the most active catalyst. The O_2 formation rate was 170 nmol cm^{-2} min^{-1} (k_{obs} = 1.4 × 10^3 s^{-1}), with a 90% Faradaic efficiency.

Electrochemical studies performed in 0.2 M sodium phoshate buffer at pH 7 show a strong catalytic current with an onset potential at +1.4 V vs NHE and a high O_2 evolution over several hours without loss of catalytic activity. Indeed, authors provided different evidences for the robustness of the complex under catalytic conditions, showing negligible decomposition over hours of operation.

Similar complexes based on Co^{III}-porphyrins able to perform water oxidation under light activation have been reported by Sakai and co-workers.[93] In particular, the Co^{III} is surronded by a porphyrin with different aryl groups in the four meso-positions (Fig. 1.13b). The best performing complex, bearing benzenesulfonic acid in meso-positions, reaches 122 TONs and a TOF of 0.17 s^{-1} in 0.1 M phosphate buffer at pH 11, with the $[Ru(bpy)_3]^{2+}/Na_2S_2O_8$ system.

Another molecular cobalt-based complex able to catalyze both oxidation and reduction of water has been reported by Lau (Fig. 1.13c).[94] This *trans*-$[Co^{II}(qpy)(OH_2)_2]^{2+}$ complex (qpy = 2,2':6',2'':6'',2'''-quaterpyridine) was able to oxidize water with the $[Ru(bpy)_3]^{2+}/Na_2S_2O_8$ system in 15 mM borate buffer pH 8, reaching 335 TONs upon irradiation at λ = 457 nm for 90 minutes.

In 2013, a similar cobalt complex bearing a salophen ligand (N,N'-bis(salicylaldehyde)-1,2-phenylenediamine) was presented by Sartorel and co-workers (Fig. 1.13d).[95] This Co^{II}(salophen) complex provided water oxidation in neutral aqueous solution both electrochemically and in a photoactivated system. In particular, a very low operating overpotential of 0.3 V was found, outperforming the previously reported cobalt-based WOCs, with overpotentials in the range 0.5-0.6 V.[96–98] Also, in the presence of the $[Ru(bpy)_3]^{2+}/Na_2S_2O_8$ system, it is able to oxidize water in phosphate buffer pH 7 reaching 17 TONs and a TOF of 5.6×10^{-3} s^{-1}.

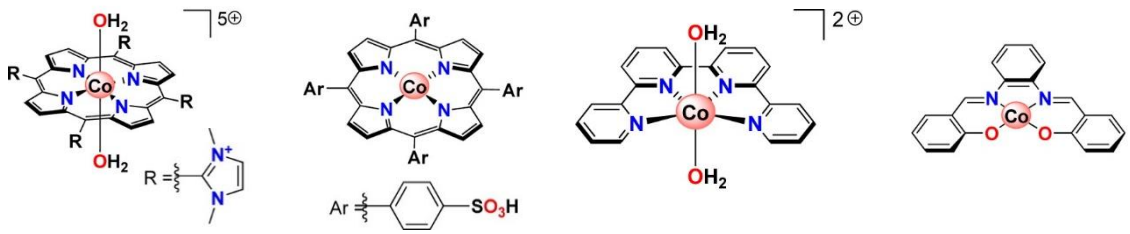

a) **b)** **c)** **d)**

Fig. 1.13 Structure of the mononuclear cobalt catalysts: **a)** Co^{III}-5,10,15,20-tetrakis-(1,3-dimethylimidazolium-2-yl)porphyrin;[92] **b)** Co^{III}-meso-tetra(4-sulfophenyl)porphyrin;[93] **c)** *trans*-$[Co^{II}(qpy)(OH_2)_2]^{2+}$;[94] **d)** Co^{II}(salophen).[95]

Because of its low toxicity, low cost and high natural availability, iron has been also considered as a promising metal for the building of artificial WOCs.

Molecular single site iron complexes have been commonly reported to act as WOCs in the presence of a sacrifical oxidant, such as Ce^{IV}.[99,100] Recently, Meyer and co-workers have presented an iron electrocatalyst for water oxidation working in propylene carbonate-water mixtures (Fig. 1.14).[101] The $[Fe^{III}(dpaq)(H_2O)]^{2+}$ (dpaq = 2-[bis(pyridine-2-ylmethyl)]amino-N-quinolin-8-yl-acetamido) performed at least 29 TONs over a 15 hours electrolysis period with a 45% Faradaic efficiency and no observable decomposition of the catalyst.

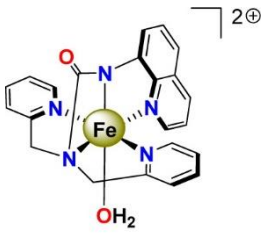

Fig. 1.14 Structure of the mononuclear iron complex $[Fe^{III}(dpaq)(H_2O)]^{2+}$.[101]

Finally, the investigation of copper-based catalysts represents a new promising research area for water oxidation. So far, electrochemical bias have been used for the activation of such WOCs.

The first example of homogeneous copper-based WOC was reported in 2012 by Mayer and co-workers.[102] This $(bpy)Cu^{II}(OH)_2$ (bpy = 2,2'-bipyridine) has the remarkable feature of self-assembling from simple copper salts and bipyridine in aqueous solution, leading to the formation of the active WOC (Fig. 1.15a). From electrochemical experiments, authors estimated a TOF value of 100 s^{-1} under purely kinetic conditions, when the current is limited only by catalytic steps in solution (S-shaped CVs). This kinetic limit is favored at slow scan rates (≤10 mV s^{-1}) and low catalyst concentrations (≤100 μM in Cu). Furthermore, from the linear dependence of the catalytic current with the Cu concentrations, they proved the molecular nature of the catalyst and a single-site mechanism.

In 2013, Meyer and co-workers reported another copper-based electrocatalyst able to self-assemble in aqueous solution at pH 11 from $Cu(OH)_2$ and triglycylglycine macrocyclic ligand (TGG^{4-}), the $[(TGG^{4-})Cu^{II}\text{-}OH_2]^{2-}$ (Fig. 1.15b).[103] In a CV experiment under the same conditions, a well-defined and reversible wave at +0.58 V vs NHE is observed, followed by an intense catalytic current with an onset potential at +1.10 V vs NHE,

corresponding to an overpotential of 520 mV. Upon an 8 hours electrolysis, a Faradaic efficiency of 99% was calculated together with a TOF of 33 s^{-1} and a TON of 13.

a) **b)**

Fig. 1.15 Structure of the mononuclear copper catalysts: **a)** $(bpy)Cu^{II}(OH)_2$;[102] **b)** $[(TGG^{4-})Cu^{II}\text{-}OH_2]^{2-}$.[103]

In Table 1.2, the molecular WOCs and their features are briefly summarized, together with the operating conditions reported for the catalysis.

Table 1.2 Overview on molecular WOCs and their properties.

Catalyst	System	Properties	Ref.
POM WOCs			
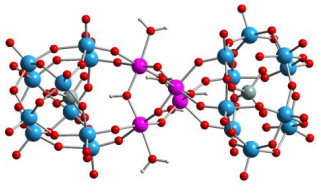 $\{Ru^{IV}_4(\mu\text{-}O)_4(\mu\text{-}OH)_2(H_2O)_4[\gamma\text{-}SiW_{10}O_{36}]_2\}^{10-}$	Electrochemical	η = 0.20-0.35 V (pH 1-7)	[71–75,77–81]
	Light-driven, $([Ru(bpy)_3]^{2+}/Na_2S_2O_8)$	TON = 350 (pH 7)	
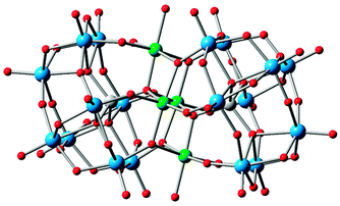 $[Co_4(H_2O)_2(\alpha\text{-}PW_9O_{34})_2]^{10-}$	Light-driven, $([Ru(bpy)_3]^{2+}/Na_2S_2O_8)$	TON = 220 (pH 8)	[84–86]
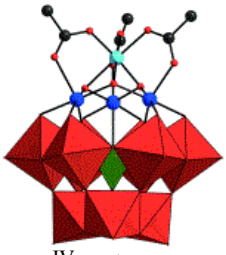 $[Mn^{III}_3Mn^{IV}O_3(CH_3COO)_3(A\text{-}\alpha\text{-}SiW_9O_{34})]^{6-}$	Electrochemical	η = 0.53 V (pH 5.2)	[87]
	Light-driven, $([Ru(bpy)_3]^{2+}/Na_2S_2O_8)$	TOF = 2.84 × 10^{-3} s^{-1} (pH 5.2)	

Table 1.2 Overview on molecular WOCs and their properties (continue from the previous page).

Single site WOCs			
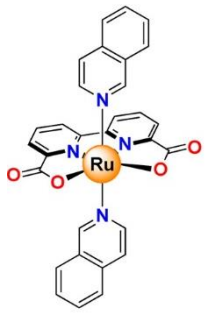 $[Ru^{II}(bda)(isoq)_2]$	Light-driven, $([Ru(bpy)_3]^{2+}/Na_2S_2O_8)$	TON = 218 TOF = 0.31 s^{-1} (pH 7)	[88–91]
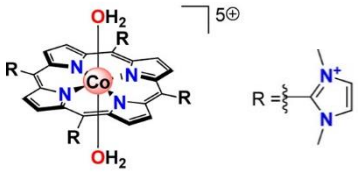 Co^{III}-5,10,15,20-tetrakis-(1,3-dimethylimidazolium-2-yl)porphyrin	Electrochemical	$k_{obs} = 1.4 \times 10^3$ s^{-1} (pH 7) Faradaic efficiency = 90%	[92]
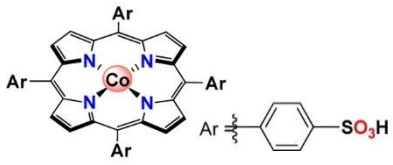 Co^{III}-meso-tetra(4-sulfophenyl)porphyrin	Light-driven, $([Ru(bpy)_3]^{2+}/Na_2S_2O_8)$	TON = 121.8 TOF = 0.17 s^{-1} (pH 11)	[93]
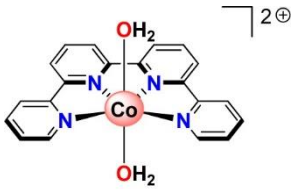 *trans*-$[Co^{II}(qpy)(OH_2)_2]^{2+}$	Light-driven, $([Ru(bpy)_3]^{2+}/Na_2S_2O_8)$	TON = 335 (pH 8)	[94]
 Co^{II}(salophen)	Electrochemical	η = 0.30 V (pH 7)	[95]
	Light-driven, $([Ru(bpy)_3]^{2+}/Na_2S_2O_8)$	TON = 17 TOF = 5.6×10^{-3} s^{-1} (pH 7)	

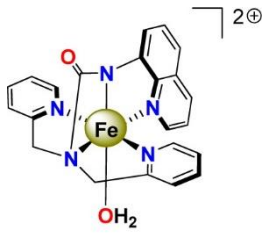 $[Fe^{III}(dpaq)(H_2O)]^{2+}$	Electrochemical	TON > 29 TOF = 0.15 s^{-1} Faradaic efficiency = 45% (propylene carbonate/H_2O 92:8, v/v)	[101]
 $(bpy)Cu^{II}(OH)_2$	Electrochemical	η = 750 mV TON > 30 TOF = 100 s^{-1} (pH > 12)	[102]
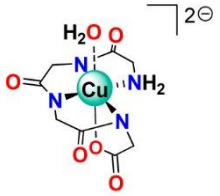 $[(TGG^{4-})Cu^{II}\text{-}OH_2]^{2-}$	Electrochemical	η = 520 mV TON = 13 TOF = 33 s^{-1} Faradaic efficiency = 99% (pH 11)	[103]

1.7 The design of photoelectrochemical devices

The development of artificial devices integrating the molecular components described above and capable of mimicking the photosynthetic natural assembly represents a key challenge for evolution in the field of energy storage. During last years, attention has been focused on the building of such systems capable of splitting water using solar light, the so-called solar cells. An example of these devices are the photoelectrochemical cells (PECs) (Fig. 1.16).[104] They are based on two photoelectrodes connected together by an external circuit, one for water oxidation in the anodic compartment (photoanode) and one for proton reduction in the cathodic compartment (photocathode). These two are separated by a porous baffle which is permeable to protons and which prevents also hazardous mixtures of oxygen and hydrogen. Here, both electrodes are semiconductors (n-type for photoanode and p-type for photocathode) used to exploit the photo-induced bias due to the photo-generated electron-hole pairs. Suitable energy levels for the conduction and valence bands of the semiconductors should be considered, in order to match the thermodynamic requirement for the redox processes. Alternative strategies can also be adopted: a semiconductor with a small

band gap, whose bands level might not be suitable for the reaction, can be coupled with an organic dye molecule (light-harvesting chromophore) able to absorb visible light and transfer photoexcited electrons from its HOMO orbital to the conduction band of the semiconductor, thus converting in an oxidized form. This strategy, together with suitable water oxidation catalysts, is today widely used in dye-sensitized photoelectrochemical cells (DS-PEC).

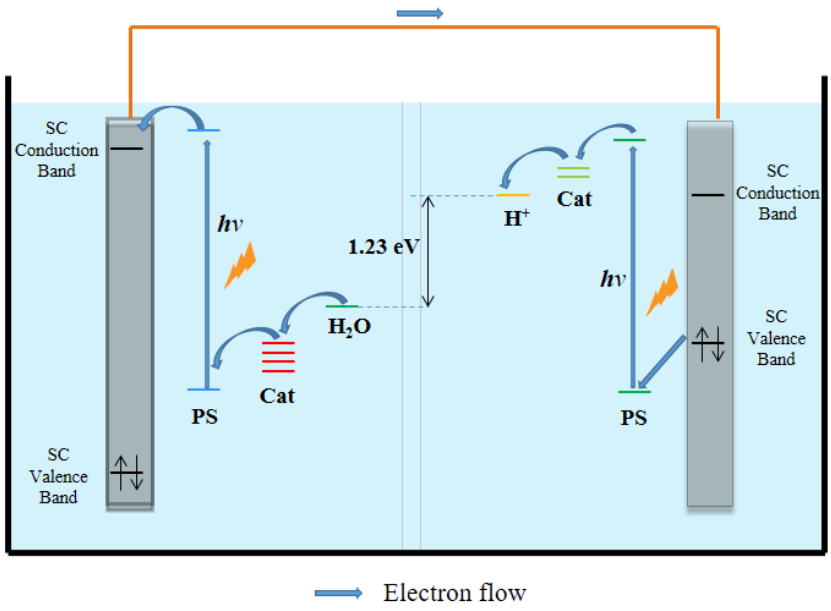

Fig. 1.16 General scheme of a photoelectrochemical cell (PEC) for water splitting.

1.7.1 Dye-sensitized photoanodes for water oxidation: state of the art

A dye-sensitized photoanode (and in general, a photoelectrode) should include these components:

- a **transparent conductive oxide film** (TCO) onto the glass slide used as electrode for electron collection;
- a **n-type semiconductor** (SC) usually made of nanocrystalline metal oxides film with good electron mobility for obtaining the charge saparation, such as TiO_2, SnO_2 and WO_3 (Fig. 1.17). Nanostructured films should be preferred to increase the active surface;
- a **dye** or a **photosensitizer** (PS) used to generate oxidizing holes upon injection of the photoexcited electrons in the conduction band of the semiconductor. The suitable chromophore should have the excited state level higher than the semiconductor

conduction band edge and the ground state level lower than the water oxidation energy threshold;

- a stable **WOC** able to collect the four oxidizing holes from the oxidized form of the dye. It is then restored upon oxidation of water.

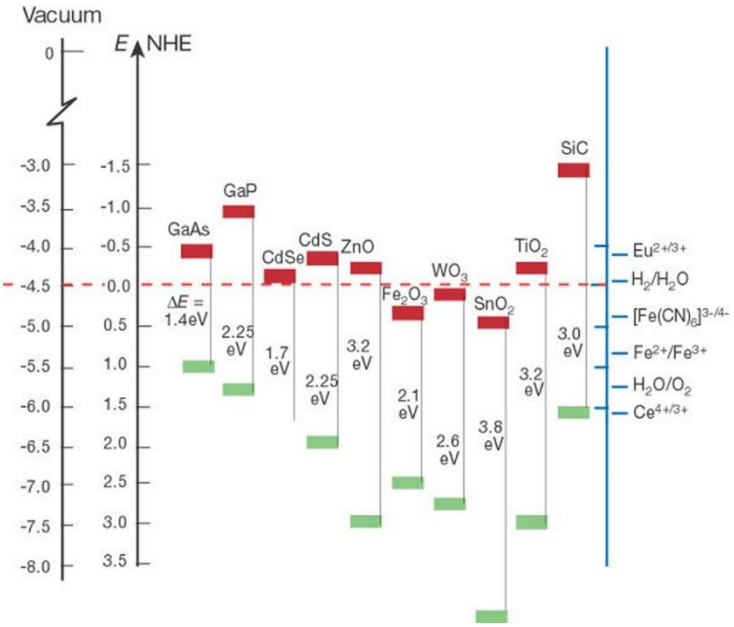

Fig. 1.17 Band gaps and energy band levels of common semiconductors compared to water oxidation and reduction standard potentials.

The processes occurring in the anodic compartment can be summarized in these steps:

$$PS + h\nu \rightarrow PS^* \quad (1.21)$$

$$PS^* + SC \rightarrow PS^+ + SC(e^-) \quad (1.22)$$

$$TCO + SC(e^-) \rightarrow TCO(e^-) + SC \quad (1.23)$$

$$PS^+ + WOC \rightarrow PS + WOC^+ \quad (1.24)$$

$$WOC^{4+} + 2H_2O \rightarrow WOC + O_2 + 4H^+ \quad (1.25)$$

However, also recombination processes can occur, limiting the efficiency of the cell:

$$PS^+ + SC(e^-) \rightarrow PS + SC \quad (1.26)$$

$$WOC^{n+} + SC(e^-) \rightarrow WOC^{(n-1)+} + SC \quad (1.27)$$

For this reason, several tricks can be used to prevent such unproductive processes. For instance, the anchoring of the dye to the semiconductor surface can be employed to obtain fast electron injection (Eq. 1.22) and to avoid dye desorption. Also, photosensitizer-catalyst

assemblies obtained by covalent linking, electrostatic interaction or using recognition groups can be exploited, leading to fast electron transfers (Eq. 1.24).

From transient absorption spectroscopy, it is possible to determine the rate of electron transfers involved in these processes.[105] In order to avoid excited state relaxation of the dye, an electron injection on a sub-ps timescale should occur from the excited state of the dye to the semiconductor (Eq. 1.22). Moreover, electron transfer from the catalyst to the oxidized form of the dye occur in the sub-ns timescale (Eq. 1.24). In order to avoid back electron transfers from the semiconductor film to the oxidized dye (Eq. 1.26) and to the oxidized WOC (Eq. 1.27), electron transport through the semiconductor to the TCO should be as fast as possible to ensure the long-lived charge states of the WOC (Eq. 1.23). To this aim, metal oxides blocking layers deposited between the semiconductor and the dye can be used to limit the back electron transfer to the oxidized WOC.[106]

In order to evaluate the efficiency of these photoanodes, several parameters are used: the onset potential, TON and TOF, which are strictly connected with the catalyst performance, and the IPCE and APCE parameters, which are related to the intrinsic capability of the photoelectrode of converting solar light into electrical current (see section 1.5.4).

Commonly, the photoanodes presented in literature took advantage of ruthenium polypyridyl-based photosensitizers, in particular the $[Ru(bpy)_3]^{2+}$, already used for water oxidation in solution.

In 2010, Scandola and co-workers presented a photoanode, coupling this photosensitizer, nanocrystalline TiO_2 semiconductor and the Ru_4POM as WOC.[74] They reported that the Ru_4POM is able to give very fast hole scavenging from the photogenerated $[Ru(bpy)_3]^{3+}$ in the sub-ns timescale, thanks to the intimate contact between the polyanionic catalyst and the positively charged dye. Although an electrostatic interaction exists between the dye and the WOC, Hill and co-workers stated that the Ru_4POM loading onto the semiconductor-dye assembly largely depends on the point of zero charge of the supporting metal oxide rather than on the charge of the dye.[107]

A successive study by Hill and co-workers reported TiO_2-based photoanodes with a ruthenium polypyridyl photosensitizer incorporating a supramolecular recognition motif (crown ether) able to stabilize the binding of the Ru_4POM. Thank to this enhanced catalyst-dye coupling, this photoanode shows a three-fold increase in the photocurrent related to water oxidation and in the APCE value respect to the electrode with the non-functionalized dye.[108]

In 2013, Sun and co-workers have obtained exceptional results by coadsorbing onto nanostructured TiO_2 particles both $[Ru(bpy)_3]^{2+}$ and a Ru^{II}(bda) (as WOC) derivatives.[109] Visible light driven water oxidation was demonstrated by oxygen evolution in phosphate buffer solution at pH 6.8. A record photocurrent density of more than 1.7 mA/cm^2 was achieved by applying an external bias of 0.2 V vs NHE, together with a Faradaic efficiency of 80%. Since now, this is the best-performing dye-sensitized photoanode with molecular components reported in literature.

Recently, another class of metal-free organic dyes has been considered for electrode sensitization instead of using ruthenium derivatives: the perylene bisimide (PBI) derivatives (Fig. 1.18). These polycyclic aromatic molecules have been considered for their exceptional features: they have (i) a strong absorption in the visible region ($400 < \lambda < 700$ nm) with a nearly unity quantum yield, (ii) a high thermal and oxidative stability, (iii) high electron mobility, (iv) sustainable costs of the raw materials, and (v) supramolecular self-assembling properties leading to the formation of functional architectures, due to the π-stacking between neighbouring molecules.[110–113] In addition, due to the easy tunability of the HOMO and LUMO levels, PBIs has been already used in the field of organic electronics since they exhibit n-type semiconducting properties.

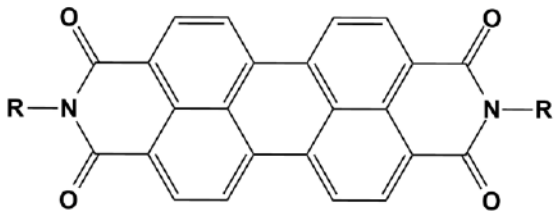

Fig. 1.18 General structure of a perylene bisimide (PBI) molecule.

An example of photoanode involving the use of PBIs was reported by Finke and co-workers in 2014.[114] A thin film of phosphonate-functionalized PBI was spin-coated onto an indium tin oxide (ITO) electrode and the CoOx catalyst was then photoelectrochemically deposited on the PBI film from a solution of Co(II) precursor in potassium phosphate buffer pH 7. This ITO| PMPDI| CoOx photoanode shows visible-light-assisted water oxidation reaching photocurrents of 150 μA/cm^2 and Faradaic efficiency higher than 80% under an applied bias of 1.2 V vs NHE. The key feature of this photoelectrode is the anchoring of the dye through strong covalent binding, ensuring an intimate contact between the dye and the semiconductor surface and preventing dye losses.

Bignozzi and co-workers have recently reported a further example of photoanode using PBI as dye, IrO_2 nanoparticles as water oxidation catalyst and different porous nanocrystalline metal oxide films including TiO_2, SnO_2, ZnO_2 and WO_3 as semiconductors.[115] The bis-cationic PBI was able to spontaneously absorb onto semiconductor substrates, but electron injection was found to be effective only on WO_3, since the back electron transfer to the oxidized dye is three order of magnitude slower than injection, as proved by transient absorption spectroscopy and injection trials with sacrificial agents. The spin-coating of IrO_2 nanoparticles onto the PBI film gave a 4-fold enhancement of the photocurrent density, reaching 70 $\mu A/cm^2$ at 0.75 V vs NHE in aqueous 0.1 M $NaClO_4$ pH 3 under illumination with an AM 1.5 G light with 435 nm cut-off.

Finally, attempts through the incorporation of the natural PSII onto nanostructured electrodes have been made by Reisner and co-workers.[116] The enzymatic photoanode consists of PSII immobilized on a mesoporous ITO electrode (*meso*ITO| PSII), where the PSII embeds the functionalities for light absorption, charge separation and water oxidation catalysis, while ITO is used as electron collector. This photoanode is capable of oxidizing water with an onset potential of +0.6 V vs NHE in a 2-(N-morpholino)ethanesulfonic acid (MES) solution pH 6.5, requiring low-energy red-light photons (680 nm). The electrode shows few limitation related to surface charge recombination and slow water oxidation catalysis but it suffers from photoinstability, due to the lack of repair machinery in the isolated PSII.

In 2015, a further improvement of this photoelectrode was obtained, where a hierarchically structured ITO electrode (IO-*meso*ITO) was developed to give exceptionally high loadings of PSII.[117] ITO electrodes were built incorporating a macroporous inverse opal (IO) architecture to facilitate the penetration of the enzyme throughout the electrode structure, with a mesoporous skeleton to further increase the effective surface area and to facilitate stable anchoring of the enzyme. The optimized IO-*meso*ITO| PSII electrode showed an onset potential at +0.2 V vs NHE and gave rise to photocurrents as high as 930 $\mu A/cm^2$ at an applied potential of 0.5 V vs NHE under irradiation with $\lambda = 679$ nm. In addition, a Faradaic efficiency of 75% and an exceptionally PSII-based TON of 4200 were found. When the PSII was coadsorbed with an Os complex-modified polymer (redox polymer) on the hierarchical electrode (IO-ITO| polymer-PSII), the performance substantially improved, reaching photocurrent densities of up to 410 $\mu A/cm^2$ at an applied potential of 0.5 V vs NHE and Faradaic efficiency of 85%.[118]

In Table 1.3, the photoanodes reported in the literature are briefly summarized, together with the parameters for the evaluation of their performance.

Table 1.3 Overview on photoanodes and their properties.

Photoanode	E vs NHE [V]	J_{max} [μA/ cm^2]	TOF [s^{-1}]	Stability $t_{1/2}$ [min]	IPCE [%]	APCE [%]	Ref.
nanoTiO_2| $[Ru(bpy)_2(dpbpy)]^{2+}$| Ru_4POM	0.20	14.2	0.004	<2	-	0.11	[108]
nanoTiO_2| [Ru(Na-5-crown-phen)$_2$ (dpbpy)]$^{4+}$| Ru_4POM	0.20	54.8	0.02	2	-	0.39	[108]
nanoTiO_2| $[Ru(bpy)_2(dpbpy)]^{2+}$| Ru(II)(bda)(4-picoline)	0.20	1700	1.0	<2	14	-	[109]
ITO| PBI| CoO_x	1.20	150	-	-	0.12	1	[114]
nanoWO_3| PBI| IrO_2	0.75	70	-	-	0.6	0.8	[115]
*meso*ITO| PS II	0.55	0.3	0.03	4	0.125	0.70	[116]
IO-*meso*ITO| PS II	0.50	930	12.9	*ca.* 5	17.0	-	[117]
IO-ITO| polymer-PS II	0.50	410	6.7	4	7.7	-	[118]

1.8 Aim of the thesis

In order to build an efficient artificial device for light-driven water oxidation, it is fundamental the effective assembly of the single optimized components, with the principal aim of orchestrating physical and chemical interfaces. In particular, the interplay between a suitable photosensitizer with a suitable catalyst is one of the key aspects for the performance of the water oxidation process, since their interactions have a marked impact on the stability of the overall system.

In this Thesis, novel systems for photocatalytic water oxidation will be investigated, focusing on the design of catalyst-photosensitizer dyads by covalent or supramolecular strategies.

In **Chapter 2**, synthesis, characterization and photocatalytic results of a novel covalent dyad based on a Co(II) single site catalyst and a Ru(II) photosensitizer moiety will be presented.

The covalent anchoring is pivotal in addressing fast (tens of picoseconds) electron transfer rates.

In **Chapter 3**, the study of a novel supramolecular assembly, combining an organic metal-free bis-cationic perylene bisimide, PBI, as photosensitizer with a totally inorganic anionic polyoxometalate, Ru_4POM, as WOC will be presented; this system evolves oxygen exploiting visible light, in the presence of persulfate as the sacrificial electron acceptor.

A final goal is the integration of the photosynthetic dyads on electroactive semiconductor surfaces for the development of regenerative photoanodes: in **Chapter 4**, the fabrication of composite photoanodes combining the photoactive PBI/Ru_4POM nano-hybrid with nanocrystalline tungsten oxide (*nano*WO_3) as the semiconductor acceptor layer will be reported, and shows photoelectrochemical water oxidation under visible light, with photocurrent densities up to 75 $\mu A/cm^2$ and Absorbance Photon to Current Efficiency (APCE) of 1.30 %.

2 A covalent approach to water oxidation: a Co(II) catalyst-Ru(II) photosensitizer dyad

2.1 Introduction

In recent years, the development of light-activated catalytic systems aiming at the production of renewable fuels has attracted great interest. In particular, efforts have been dedicated to the development of suitable photosensitizer(PS)-catalyst(WOC) assemblies for water oxidation driven with visible light.

Covalent approaches could guarantee a stringent molecular control on the PS-WOC distances and geometries as governing factors for photoinduced electron transfers to prevent side reactions leading to photosensitizer self-oxidation and degradation, or to prevent unproductive charge recombination.[54,75,76,107,119–123]

A novel dyad based on a compartmental Co(II)-Ru(II) covalent assembly will be presented in this Chapter.[124] The catalytic moiety is based on a Co(II)salophen (Coslp) unit, recently reported in literature (see section 1.6.2.2).[95] This complex enables water oxidation at neutral pH combined with a photoactivated $[Ru(bpy)_3]^{2+}/Na_2S_2O_8$ system. Coslp is able to perform up to 17 turnovers upon irradiation at 450 nm, with a quantum yield of 0.079. The oxygen evolution is levelled off after *ca.* 2 hours due to $[Ru(bpy)_3]^{2+}$ degradation. Indeed, in such photoactivated cycles, a critical step is the electron transfer from the catalyst to the oxidized photosensitizer that occurs via a bimolecular route ($k = 1.12\times10^8$ $M^{-1}s^{-1}$ for the primary ET) and may contribute to the degradation of the photosensitizer, often determining the overall efficiency of the process.

Therefore, in order to boost such electron transfer rate, a covalent approach has been proposed to enhance PS-WOC interactions.

The covalent linkage of the catalyst-photosensitizer moieties is obtained by a suitable functionalization of a phenanthroline type ligand (Fig. 2.1). Combined electrochemical and photophysical studies reveal that photoinduced, intramolecular redox events involving the two metal centres occur within a very short timescale of tens of picoseconds, confirming efficient electronic interactions between the two units. Moreover, a preliminary study dealing with the activity of the dyad in light driven water oxidation is presented, and perspectives towards the application of dyads of such type to regenerative photoanodes are discussed.

2.2 Results and discussion

2.2.1 Synthesis and electrochemical characterization

The synthesis of the Co(II)-Ru(II) dyad, **1**, (Fig. 2.1) was carried out adapting a literature procedure reported by Pellegrin and coworkers for a ruthenium-copper analog.[125,126]

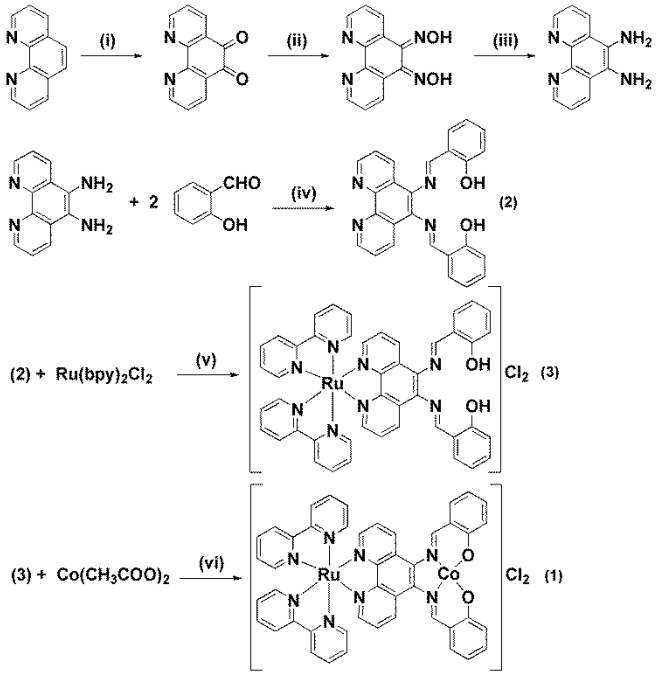

Fig. 2.1 Synthesis of **1**. (i) H_2SO_4/HNO_3, NaBr, 100°C, yield 35%; (ii) $NH_2OH{\cdot}HCl$, $BaCO_3$ in refluxing ethanol, yield 57%; (iii) 10% Pd/C, N_2H_4 in refluxing ethanol, yield 42%; (iv) triethylorthoformate in refluxing ethanol, yield 42%; (v) triethylorthoformate, $AgNO_3$ in refluxing ethanol, yield 66%; (vi) methanol, room temperature, yield 91%.

The key intermediate is the ligand N,N'-bis(salicylidene)-5,6-(1,10-phenanthroline)diamine, **2**, obtained by a four-step synthesis starting from 1,10-phenanthroline. These steps include: (i) oxidation of 1,10-phenanthroline to 1,10-phenanthroline-5,6-dione in HNO_3/H_2SO_4 under reflux;[127] (ii) condensation of 1,10-phenanthroline-5,6-dione with hydroxylamine to obtain the 1,10-phenanthroline-5,6-dioxime;[128] (iii) its reduction with hydrazine to yield the 1,10-phenanthroline-5,6-diamine;[128] and (iv) condensation of the last product with two equivalents of salicylaldehyde.[125,126] The intermediates were characterized by elemental analysis, IR and ^{1}H-NMR (see section 5.1). In particular, the ^{1}H-NMR of compound **2** shows the peaks

related to the aromatic part of the molecule, which are comprised between 7.10 and 9.21 ppm, and the peak related to the hydrogen of the -OH groups at 13.02 ppm (Fig. 2.2).

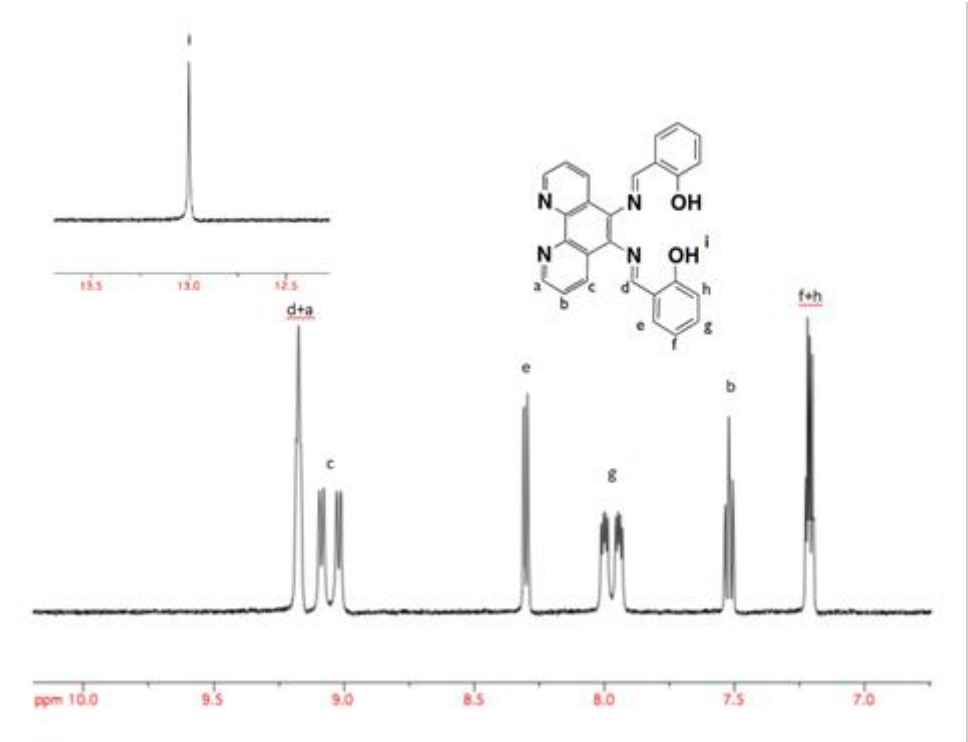

Fig. 2.2 ^{1}H-NMR (300 MHz) of compound **2** in d^{6}-DMSO.

The metallation of the ligand **2** was then achieved by reaction with *cis*-Ru(bpy)$_2$Cl$_2$, under reflux in methanol in the presence of triethylorthoformate;[125,126] the resulting complex **3** was isolated in 66% yield. The Ru(II) centre is coordinated to the ligand **2**, maintaining the two bpy ligands in its coordination sphere, as confirmed by elemental analysis and ^{1}H-NMR characterization. Also in this case, the ^{1}H-NMR reveals the signals related to compound **2** with the addition of the peaks related to the bpy ligands on the Ru centre, between 7.38 and 9.38 ppm (Fig. 2.3).

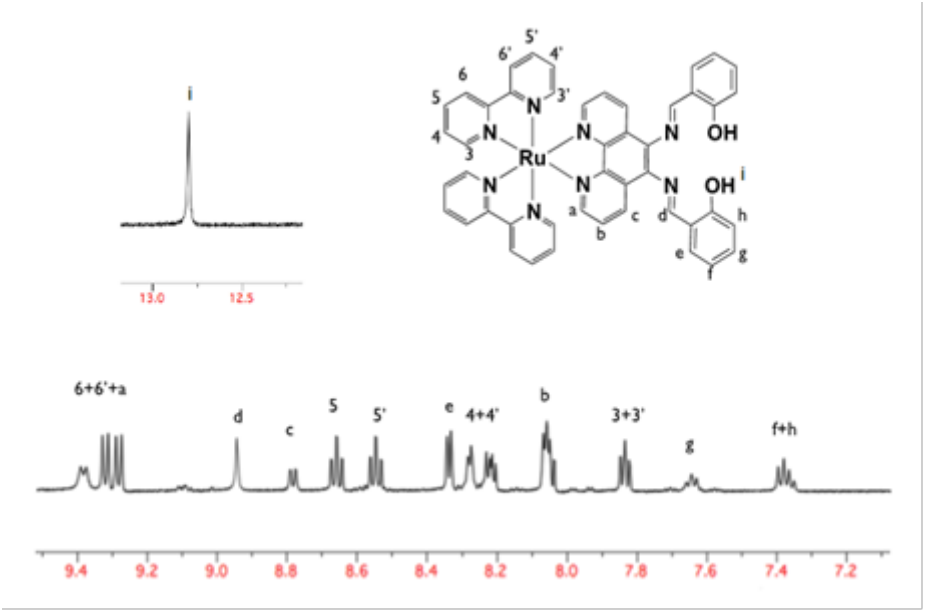

Fig. 2.3 ^{1}H-NMR (300 MHz) of compound **3** in d^{6}-DMSO.

The final step foresees the metallation of the salophenic moiety with Co(II). This was obtained by addition of cobalt acetate to the complex **3** at room temperature in methanol, and precipitation of compound **1** in 91% yield by addition of diethyl ether.

The dyad **1** and the cobalt free analog **3** were characterized by electrochemical analysis in acetonitrile solution (Fig. 2.4). During the cathodic scan, three reversible reduction waves are observed for complex **3**, respectively at $E_{1/2}$ = -1.14, -1.34 and -1.69 V vs NHE (Table 2.1). These peaks are consistent with subsequent one-electron reduction of the phenanthroline and of the bipyridine ligands.[125,126,129] The first two reversible peaks are observed also for complex **1** at the same potentials. In addition an irreversible peak at -0.74 V vs NHE is observed and ascribed to the reduction of Co(II) to Co(I).[130] During anodic scan, two irreversible processes are observed at +0.90 V and +1.43 V vs NHE for complex **3**, likely ascribable to the oxidation of the phenol groups on the salophen moiety. Moreover, a reversible process at $E_{1/2}$ = +1.53 V vs NHE is attributed to the $Ru^{III/II}$ couple. For complex **1**, only the reversible wave related to the $Ru^{III/II}$ couple at +1.52 V is observed, since the phenol groups on the salophen moiety are involved in the coordination of the cobalt centre and therefore not susceptible to oxidation.

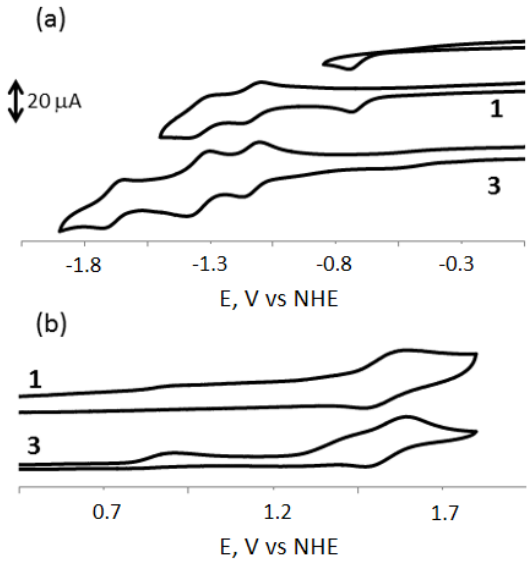

Fig. 2.4 Cyclic voltammograms of **1** and **3** under cathodic **(a)** and anodic **(b)** scans. 0.5 mM in acetonitrile, 0.1 M tetra-n-butylammonium perchlorate as a supporting electrolyte. Working electrode: glassy carbon, counter electrode: platinum wire, and reference electrode: Ag/AgCl (3 M NaCl).

Table 2.1 Potentials associated with redox events under cathodic and anodic scans for complexes **1** and **3** in acetonitrile.

	E vs NHE [V]						
1		-1.34	-1.14	-0.74[a]			1.52
3	-1.69	-1.34	-1.14		0.90[b]	1.43[b]	1.53

[a] Cathodic peak for the irreversible process; [b] anodic peak for the irreversible process.

The behavior of **1** and **3** has been examined also in aqueous solutions, as the target solvent for artificial photosynthesis (Fig. 2.5). From CV anodic scan of **3** in 0.2 M aqueous phosphate buffer at pH 7, two irreversible waves at +0.90 V and +1.25 V vs NHE are observed due to the oxidation of the phenolic groups. For complex **1**, the lack of these two waves confirms the cobalt coordination to the oxygen in the salophen moiety, together with an additional catalytic wave due to water oxidation starting at +1.25 V vs NHE.

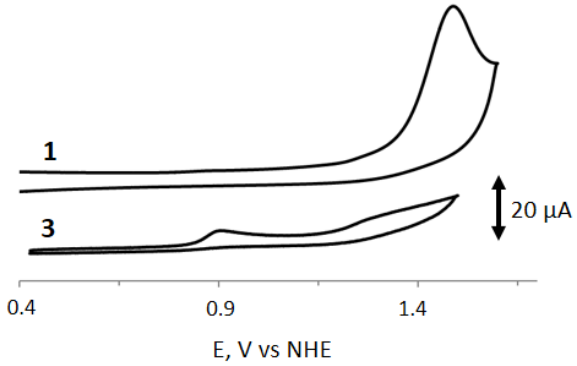

Fig. 2.5 Cyclic voltammograms of **1** and **3** under anodic scan. 0.5 mM in 0.2 M phosphate buffer pH 7. Working electrode: glassy carbon, counter electrode: platinum wire, and reference electrode: Ag/AgCl (3 M NaCl).

2.2.2 Photophysical characterization of 1 and 3 in acetonitrile and in aqueous buffer

The absorption spectra of compounds **1** and **3** compared to $[Ru(bpy)_3]^{2+}$ have been recorded in acetonitrile (Fig. 2.6). In both cases, a metal-to-ligand charge transfer (MLCT) band centered at 460 nm is observed, typical of ruthenium-based polypyridine photosensitizer. Ligand-centered (LC) transitions in the 250-350 nm region can be detected, ascribable to the bipyridine ligands (maximum absorption at 288 nm) and to the phenanthroline unit (maxima at 334 and 348 nm).[125,126,131,132] For complex **1**, a broad absorption is also observed between 350 and 450 nm, which may be attributed to cobalt-based transitions.[95,133–136]

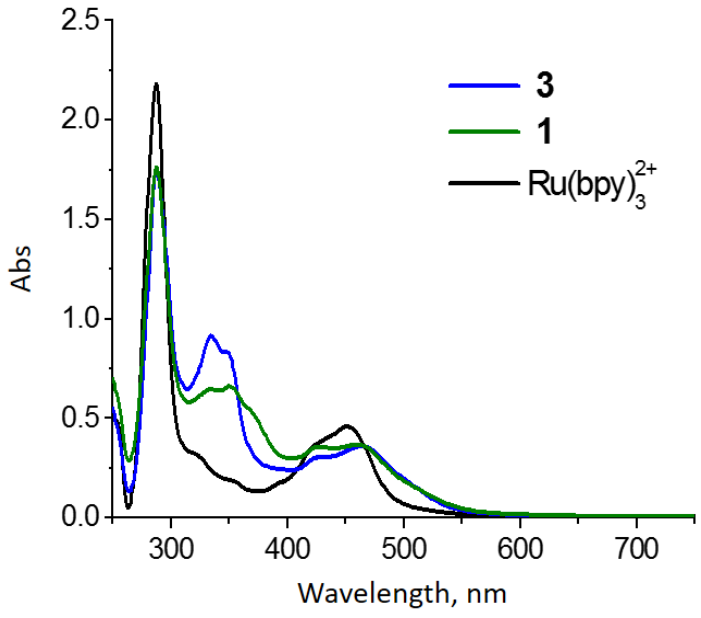

Fig. 2.6 Absorption spectra of molecular dyads **1**, **3**, and model $[Ru(bpy)_3]^{2+}$ in acetonitrile.

Upon excitation at 466 nm, the emission of both **1** and **3** in acetonitrile solution is almost completely quenched (>95% with respect to a solution of $[Ru(bpy)_3]^{2+}$ with the same optical density).

In order to identify the electron transfer events responsible for the abatement of the emission, ultrafast spectroscopy (UFS) experiments were performed in collaboration with Prof. Scandola and Dr. Natali at University of Ferrara. In the case of **3**, upon excitation at 400 nm, the initial transient absorption spectrum shows a MLCT bleach and a broad absorption at longer wavelength with a relative maximum at 530 nm, reasonably assigned to the triplet excited state, formed after excitation by ultrafast intersystem crossing from the singlet excited state (Fig. 2.7). In a 244 ps time window, the MLCT bleach practically disappears and the positive absorption increases in intensity with a shift of the maximum from 530 to 510 nm. The time constant calculated for this process is *ca.* 45 ps and is due to electron transfer from the phenolic groups to the ruthenium center of the MLCT excited state (reductive quenching), since the 510 nm absorption is a fingerprint of the reduction of ruthenium polypyridine complexes.[137] This process is a PCET and is likely assisted by intramolecular hydrogen bonding within the salophen moiety of the ligand.[138,139]

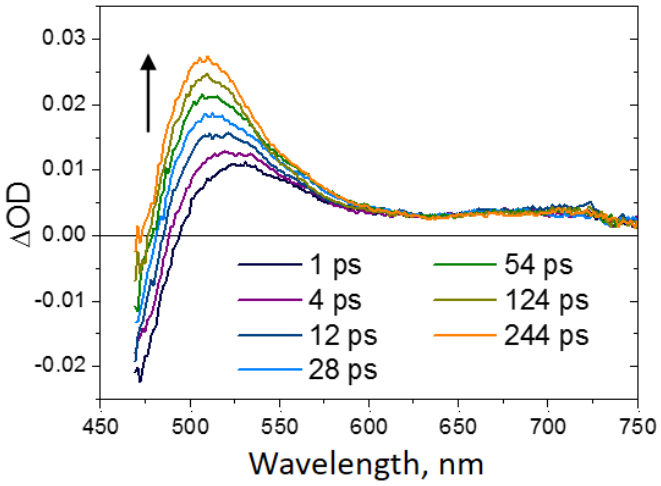

Fig. 2.7 Difference absorption spectra at 1-244 ps obtained by UFS (400 nm excitation) on **3** in acetonitrile.

When the cobalt is inserted in the ligand cavity, the photophysical processes significantly change. Similarly to **3**, the initial transient spectrum obtained by UFS corresponds to the triplet MLCT excited state. In this case, however, the positive absorption at 530 nm decays rapidly with a time constant of 15 ps (Fig. 2.8a). In this process a long-lived transient with an estimated lifetime of *ca.* 6 ns is formed, characterized by weak positive absorption and

substantial bleach left at 470 nm. Overall, these spectral changes are compatible with fast oxidative quenching of the MLCT excited state by the cobalt center, followed by slow charge recombination (Fig. 2.8b).

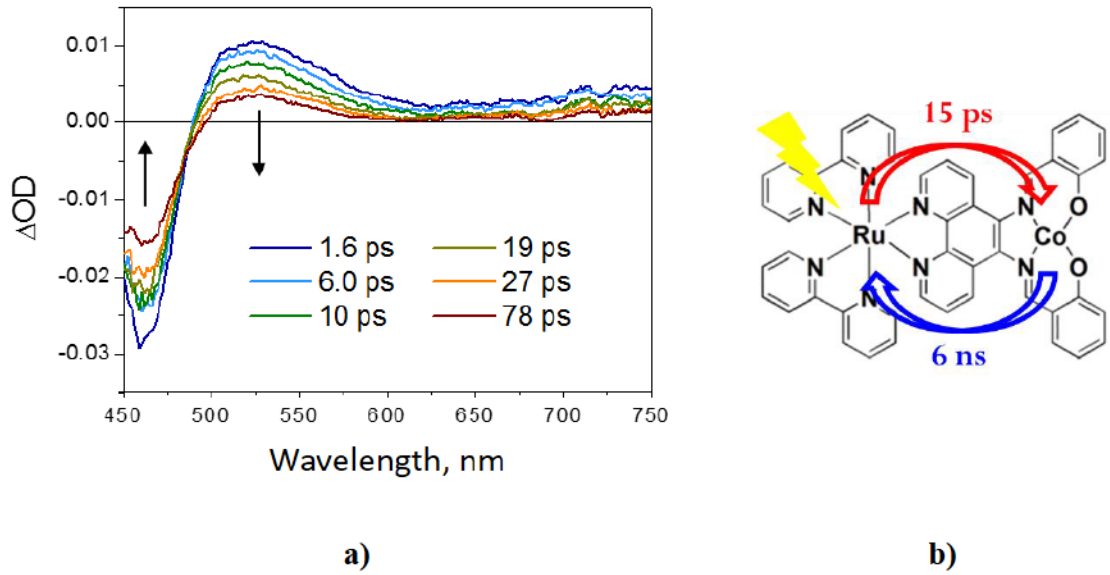

a) **b)**

Fig. 2.8 a) Difference absorption spectra at 1-244 ps obtained by UFS (400 nm excitation) on **1** in acetonitrile; **b)** scheme of the intramolecular electron transfer events occurring in **1**.

The photophysical properties of **1** and **3** change dramatically in aqueous phosphate buffer at pH 7, where partial recovery of the typical emission of Ru(II) polypyridine species is observed for both compounds (Fig. 2.9).

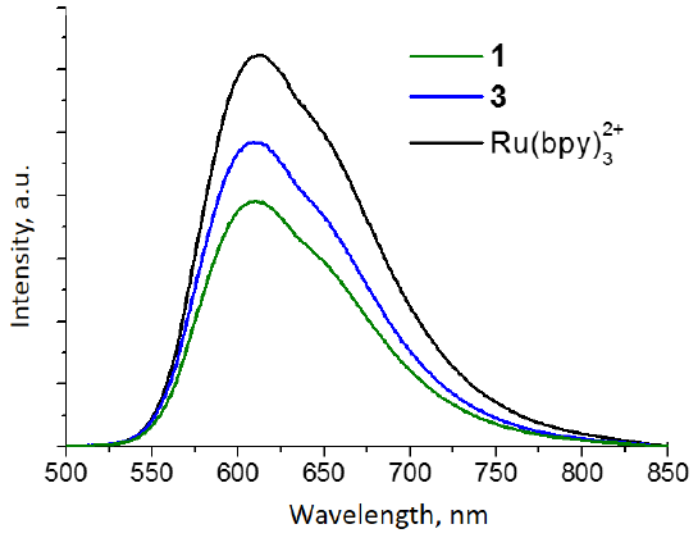

Fig. 2.9 Emission spectra (excitation at 400 nm, optically matched solutions) in 20 mM phosphate buffer (pH 7) of **1**, **3**, and $[Ru(bpy)_3]^{2+}$.

In the case of **3**, partial protonation of the salophenic ligand may take place in phosphate buffer at pH 7, thus preventing the proton-coupled electron transfer mechanism of the reductive quenching. Concerning compound **1**, the lack of quenching by the cobalt centre is observed but it seems to be hardly attributable to a solvent effect. A possible explanation could be the presence of more complex equilibria in aqueous environment, possibly involving (i) coordination of axial ligands[140] making oxidative quenching thermodynamically unfavourable or, more likely, (ii) partial leaching of cobalt. This could be relevant to the evaluation of light activated water oxidation.

2.2.3 Light driven water oxidation

The performance of complex **1** through water oxidation was tested in a photocatalytic system in the presence of 5 mM of $Na_2S_2O_8$ as sacrificial electron acceptor and 1 mM of $[Ru(bpy)_3]^{2+}$ as a photosensitizer (this was added in order to improve the light absorption of the solution) (Scheme 2.1). This system has been already described in section 1.5.1 (Eqs. 1.13-1.18).

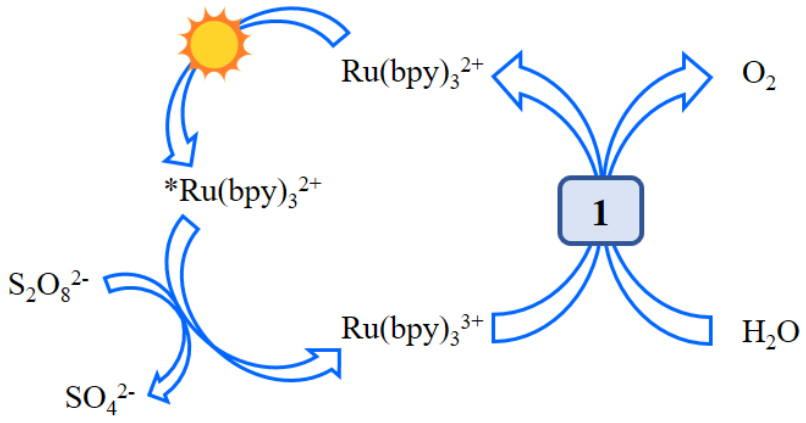

Scheme 2.1 Schematic representation of the photoinduced system.

In Fig. 2.10 typical oxygen evolution kinetics are reported, where the gas formation starts upon illumination of the solution containing the three components **1** / $[Ru(bpy)_3]^{2+}$ / $S_2O_8^{2-}$ (time = 0 min), and stops after about two hours due to photosensitizer degradation. Indeed, $[Ru(bpy)_3]^{3+}$, the photogenerated oxidant, is susceptible to self-degradation by auto-oxidation of the bipyridine organic ligands. As already mentioned, the sulfate radical formed during the reaction is a high oxidizing species and in principle it could react directly with

the catalyst; to avoid this process a higher concentration of photosensitizer respect to the WOC is required, to direct preferentially the reaction to the oxidation of the PS. Finally, a buffered solution is used as solvent in order to prevent lowering of pH during the catalytic reaction, since the oxygen production is simultaneous with H^+ generation.

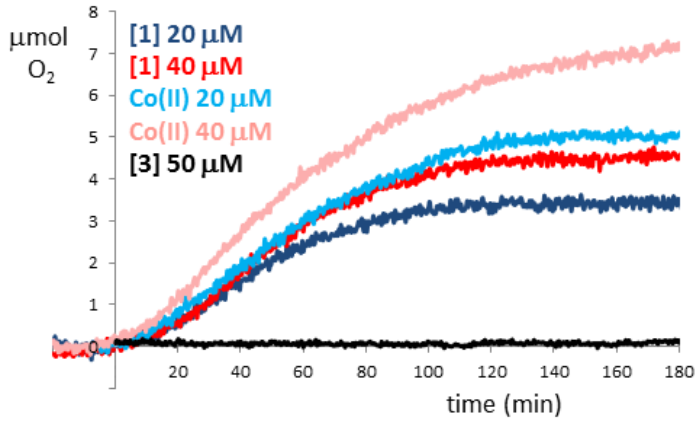

Fig. 2.10 Kinetics of O_2 evolution from 15 mL of 20 mM phosphate buffer pH 7 with 5 mM $Na_2S_2O_8$, 1 mM $[Ru(bpy)_3]^{2+}$, illumination by a LED emitting at 450 nm. Blue trace: 20 µM **1**; red trace: 40 µM **1**; light blue trace: 20 µM $Co(NO_3)_2$; pink trace: 40 µM $Co(NO_3)_2$; black trace: 50 µM **3**.

The kinetics of oxygen evolution in 20 mM phosphate buffer pH 7 have been reported with 20 and 40 µM of **1** (blue and red traces, respectively; see Table 2.2) upon irradiation with a blue LED emitting at 450 nm. In these two runs, 3.50 and 4.55 µmol of O_2 are produced after 3 hours; these correspond to a total TON per cobalt center of 11.7 and 7.6 respectively. The maximum O_2 production rates (determined in the linear range of the kinetic profiles, between 5 and 10 minutes after irradiation) are 0.80 and 0.96×10^{-4} µmol/s, corresponding to TOF values of 2.67 and 1.61×10^{-3} s^{-1}, respectively. The maximum quantum yield (Φ) of the process ([**1**] = 40 µM) is 0.037. As expected, the cobalt free analog **3** is inactive under the same reaction conditions (black trace in Fig. 2.10).

Table 2.2 Catalytic performance parameters for **1** in water oxidation process with 5 mM $Na_2S_2O_8$, 1 mM $[Ru(bpy)_3]^{2+}$, illumination by a LED emitting at 450 nm in 20 mM phosphate buffer pH 7.

Complex 1 [μM]	O_2 evolution [μmol] (TON)	O_2 evolution rate [μmol/s] (TOF, s^{-1})	Quantum yield (Φ)	Chemical Yield [%]
20	3.50 (11.7)	0.80×10^{-4} (2.67×10^{-3})	0.030	9.3
40	4.55 (7.6)	0.96×10^{-4} (1.61×10^{-3})	0.037	12.1

Moreover, in order to check if the catalytic activity could be partially ascribed to Co(II) ions leaching from complex **1** (hypothesis (ii) presented above; Eq. 2.1),[92,141] oxygen evolution tests were performed with $Co(NO_3)_2$ as catalyst in the same conditions and at the same metal concentration (light blue and pink traces in Fig. 2.10). Also in this case, oxygen evolution is observed with similar kinetic profiles in the 20-40 μM range as in the presence of **1**. Therefore, the presence of dissociation equilibria leading to the formation of Co(II) aquo-ions from **1** (Eq. 2.1) cannot be ruled out by kinetic evidences.

$$\mathbf{1} \underset{-\,2\,H^{+}}{\overset{2\,H^{+}}{\rightleftharpoons}} \mathbf{3} + Co^{II}(aq) \qquad (2.1)$$

In addition, since it is generally assumed that Co(II) aquo-ions evolves to cobalt nanoparticles under water oxidation conditions, dynamic light scattering (DLS) measurement were performed for the spent reaction mixture: since the scattering intensity was found to be close to the detection limit of the instrument (as it occurs for the freshly prepared solution mixture), this technique rules out a major formation of nanoparticles.

The equilibria hypothesis can also justify the partial emission recovery of **1** observed in aqueous solution compared to the quenched system in acetonitrile. Thus, the emission properties can be ascribed to complex **3**, generated from **1** upon leaching of the Co(II) center (Fig. 2.9, see above discussion). Therefore, the oxygen evolving catalysis can be likely due to both complex **1** and Co(II) aquo-ions in the ratio 20:80, as estimated by the emission intensity shown in Fig. 2.9. Indeed, also from CV scans in phosphate buffer (Fig. 2.5) seems

that Co(II) is not completely released from **1** with formation of **3**, since the voltammogram for the two species are totally different. In particular, the irreversible wave related to the oxidation of phenol groups in **3** is not observed in the CV scan of **1**, suggesting the presence of complex **1**.

Finally, some flash photolysis experiments have been performed in collaboration with Prof. Franco Scandola and Dr. Natali at University of Ferrara, in order to probe the photoinduced generation of Ru(III) by excitation of complex **1** or **3** in the presence of persulfate. Indeed, in such photocatalytic cycles, the primary process is the oxidative quenching of the photosensitizer MLCT excited state by $S_2O_8^{2-}$, leading to the generation of Ru(III), followed by hole transfer to the catalyst. A high rate for the last step is the key requirement to prevent photosensitizer degradation. Experiments were performed in phosphate buffer pH 7, with 5 mM $Na_2S_2O_8$ and 50 μM of **1** or **3** upon excitation at λ = 355 nm (Fig. 2.11). With complex **3**, after few nanoseconds (time resolution given by the laser pulse) very little amounts of Ru(III) are detected, *ca.* 5% of what is expected from comparative experiments carried out with $[Ru(bpy)_3]^{2+}$ (Fig. 2.11a and b). This result is very likely ascribable to fast (sub-ns) intramolecular hole scavenging from Ru(III) by the phenolic moieties. The fact that a similar, very small amount of Ru(III) is obtained with dyad **1** (Fig. 2.11c) is fully consistent with the hypothesis of extensive (*ca.* 80%) dissociation of **1** to **3**.

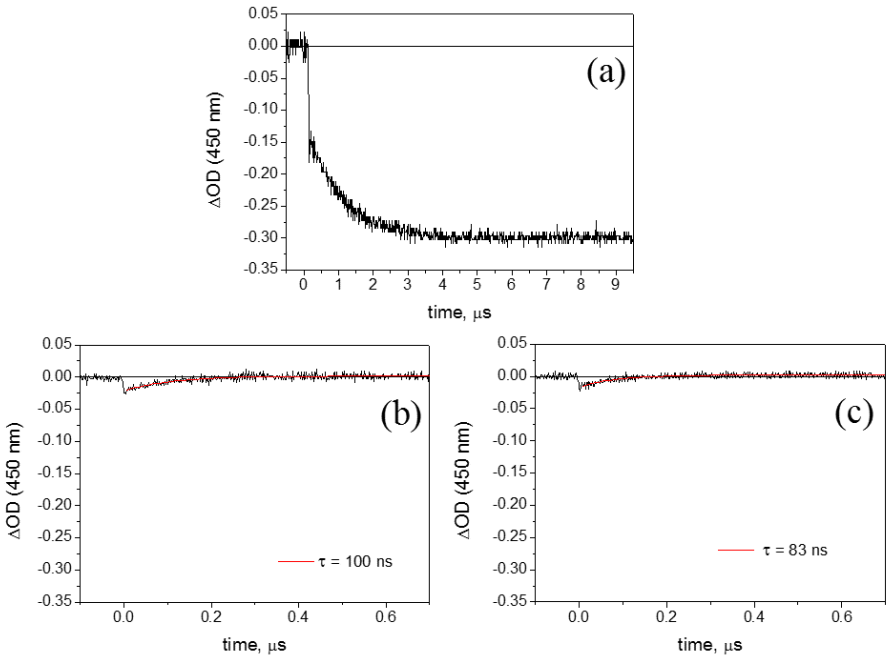

Fig. 2.11 Kinetic analysis at 450 nm obtained by laser flash photolysis (355 nm excitation) in pH 7 phosphate buffer solutions (optically matched at the excitation wavelength) containing **a)** $[Ru(bpy)_3]^{2+}$ and 5 mM $Na_2S_2O_8$, **b) 3** and 5 mM $Na_2S_2O_8$, and **c) 1** and 5 mM $Na_2S_2O_8$.

2.3 Conclusions and perspectives

In this chapter, a novel covalent dyad **1** has been presented, based on a compartmental Co(II)-Ru(II) assembly, where a cobalt salophen unit (water oxidation catalytic moiety) is anchored to a Ru(II) unit with bipyridine and phenanthroline type ligands (photosensitizer moiety).

From photophysical characterization in aqueous environment, an oxidative quenching of the photosensitizer moiety by the Co(II) is observed in 15 ps, confirming the electronic interaction between the two metal centers. In principle, this fast quenching of the photosensitizer excited state might be detrimental for the use of **1** in homogeneous systems in the presence of persulfate as SEA, where oxidative quenching of the photosensitizer excited state occurs via a bimolecular route, typically in tens of ns.[50,74,75,95,121–123,142] However, in regenerative systems where the PS-WOC dyad is supported onto a surface of a semiconductor, electron injection into the conduction band of the semiconductor can occur in hundreds of fs.[143] For this reason, such dyad displaying an intramolecular quenching could still be considered for this application.

Another key aspect that has to be considered is the stability of the dyad in the aqueous environment. From photophysical characterization in phosphate buffer and catalytic activity of **1**, the presence of dissociation equilibria has been hypothesized, suggesting in particular the partial leaching of the cobalt center. In this respect, the behavior of this complex is markedly different from that observed for the cobalt(II) salophen catalyst, which was found to be stable in aqueous environment.[95] The reason of the instability of **1** might be related to its cationic character, and to the electron-withdrawing character of the salophen moiety in **1**, leading to the destabilization of the coordination of the cobalt ion, especially in its low oxidation state. Moreover, a slight distortion of the salophenic ligand is expected, due to the steric hindrance between the protons in 4 and 4' positions of the phenanthroline moiety and the protons of the imine groups,[125] causing instability towards cobalt coordination. To this aim, strategies to reinforce the stability towards the aqueous environment should be considered, in order to propose salophen-based dyads for the design of efficient and durable photoanodes.

3 A supramolecular route for water oxidation with visible light: Perylene bisimides-oxygenic POM photoactive assemblies

3.1 Introduction

As discussed in Chapter 2, a covalent approach between a chromophore and a catalyst is a valuable approach to tune the control of the distances and of the geometries of the donor-acceptor species. Nevertheless, a covalent anchoring of two functional units may require severe synthetic strategies, while the photocatalytic outcome is often suppressed by fast charge recombination. Interestingly, Nature uses non-covalent motifs to drive the process of photosynthesis;[42,144,145] therefore, a supramolecular approach has been considered to design a novel assembly combining a metal-free perylene bisimide (PBI) as photosensitizer[113,114,146] with a totally inorganic ruthenium polyoxometalate (POM) as catalyst (Fig. 3.1).

PBI dyes have been extensively applied in photovoltaic technologies as versatile organic semiconductors, with tunable absorption and electron accepting properties,[115,147–150] while POMs are an emerging class of robust, all-inorganic molecular WOCs, proposed as synthetic analogs of the OEC in PSII.[42,87,151,152]

The redox properties of PBIs can be conveniently tuned by modification of their substituents (most often in the 1, 6, 7 and/or 12 positions of the hydrocarbon core, the so-called "bay" positions, and in the imide N,N' positions; Fig. 3.1a),[110,113] to reach suitable ground and excited state reduction potentials, turning into very potent photo-oxidants.[149] Indeed, their electron accepting capability emerges upon photoexcitation in combination with several electron donors such as phtalocyanines,[153–156] porphyrins,[157,158] and metal complexes.[146,159] For these reasons, PBIs are considered a molecular version of n-type organic semiconductors. Other key features, as already reported in section 1.7.1, include: (i) strong absorptions in the visible region ($400 < \lambda < 700$ nm), (ii) a high thermal and oxidative stability, (iii) sustainable costs of the raw materials, and (iv) supramolecular self-assembling properties leading to the formation of functional architectures, due to the π-stacking between neighbouring molecules.[110–113]

In particular, the cationic N,N'-bis(trimethylammonium)ethylene)perylene-3,4,9,10-tetracarboxylic acid bisimide (PBI^{2+}) (Fig. 3.1a) has been considered for the construction of a supramolecular assembly with the polyanionic $\{Ru^{IV}_4(\mu\text{-}O)_4(\mu\text{-}OH)_2(H_2O)_4[\gamma\text{-}SiW_{10}O_{36}]_2\}^{10-}$ (Ru_4POM),[71,72] a state of the art WOC (Fig. 3.1b; see section 1.6.2.1) in terms of overpotential ($\eta = 0.25$ - 0.35 V, depending on the pH),[71,72] electron transfer (ET) rates to photosensitizers (ET occurring in few picoseconds with Ru(II) polypyridine

photosensitizers)[160] and quantum yield in photoactivated cycles for water oxidation with visible light (Φ up to 0.30).[54] These two molecular components self assemble in water by electrostatic interactions, as supported by the map of eletrostatic potential (MEP) analysis (Fig. 3.1c), leading to the formation of a novel PBI^{2+}•Ru_4POM hybrid.

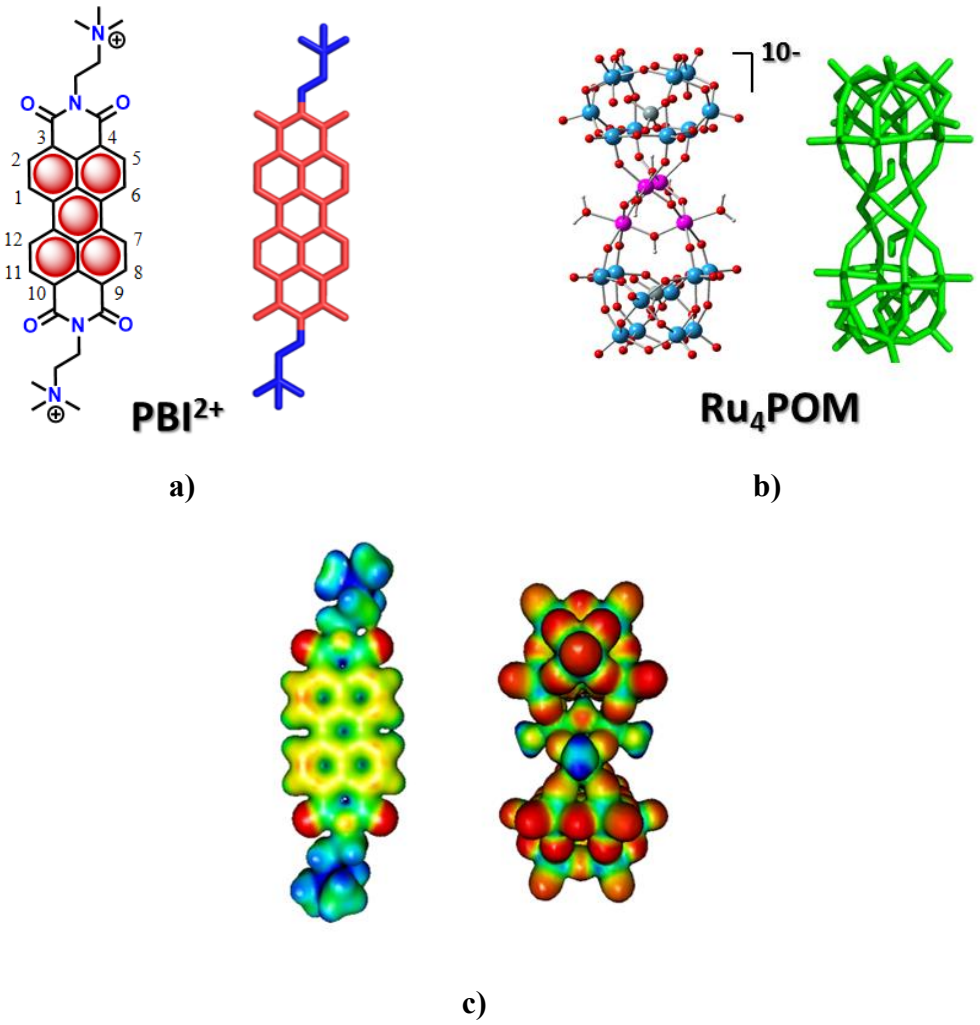

Fig. 3.1 a) Schematic view of the water soluble, amphiphilic, bis-cationic photosensitizer N,N′-bis(2-(trimethylammonium)ethylene)perylene-3,4,9,10-tetracarboxylic acid bisimide, PBI^{2+} and **b)** of the decaanionic, totally inorganic, water oxidation catalyst $[Ru_4(\mu\text{-}O)_4(\mu\text{-}OH)_2(H_2O)_4(\gamma\text{-}SiW_{10}O_{36})_2]^{10-}$, Ru_4POM. **c)** Map of the electrostatic potential of PBI^{2+} and Ru_4POM (blue and red regions indicate positive and negative electrostatic potential, respectively); a single point energy calculation at the B3LYP/LANL2DZ level was performed from the crystallographic geometries of PBI^{2+} and Ru_4POM.

In this Chapter, the characterization of the PBI^{2+}•Ru_4POM hybrid in aqueous solution (pH = 2.5 - 7) will be presented, enabling water oxidation with visible light in a sacrificial cycle in the presence of persulfate as electron acceptor.

3.2 Results and Discussion

The PBI^{2+} carrying two peripheral tetra-alkyl ammonium pendants has been selected as photosensitizer, based on the following aspects: (i) it is water soluble; (ii) its amphiphilic nature induces self aggregation into linear stacked arrays even in dilute aqueous solutions;[111,161] (iii) the redox potentials of its excited state $E(PBI^{*2+}/PBI^{+}) = 2.20$ V vs the Normal Hydrogen Electrode, NHE, indicates a very potent photogenerated oxidant that matches the thermodynamic requirements for water oxidation; (iv) its electron accepting properties has been studied in photoinduced electron transfer processes;[153–155,157–159,162,163] (v) its bis-cationic charge at opposite poles offers the possibility of electrostatic interactions with anionic species, in this case with Ru_4POM.

The characterization of the PBI^{2+}•Ru_4POM hybrid has been performed by spectrophotometric and conductometric titrations, fluorescence quenching experiments, Small Angle X-ray Scattering (SAXS) analysis, zeta potential and time-resolved spectroscopy in aqueous solution, at pH 7 and 2.5. Moreover, the impact of persulfate used as sacrificial electron acceptor in light driven experiments at pH 7 has been tested in order to evaluate the stability and the performance of the preformed aggregate.

3.2.1 Solution Characterization in Phosphate Buffer pH 7

3.2.1.1 Solution Characterization of PBI^{2+}

In general, PBIs assemble in aqueous media into supramolecular aggregates, driven by hydrophobic π-π interactions between their aromatic cores. This occurs also for PBI^{2+}, as confirmed by absorption and fluorescence experiments in aqueous solution (10^{-6} - 5×10^{-5} M) by comparison with experiments in DMF, representative of organic phases, where no self-aggregation of PBI^{2+} occurs (Fig. 3.2-3.3).

According to literature, aggregate formation is confirmed by typical absorption fingerprints,[111,164] in particular when the absorption maximum at 501 nm features a higher oscillator strength than the one at 539 nm (compare spectra in Fig. 3.2 with the black one in Fig. 3.3, this latter being registered in DMF and typical for non aggregated PBI). Indeed, during the aggregation process, the ratio of the two most intensive absorption bands inverts because of the strong excitonic interactions between the PBI chromophores. As a

consequence of the hypsochromic shift of the dominant absorption bands of these aggregates, they are denoted as H-aggregates.

Fluorescence experiments perfomed in DMF upon excitation at 350 nm further confirm a non aggregated state, showing the PBI^{2+} emission features at 540 and 580 nm (Fig. 3.3); the emission quantum yield is 90% (vs Rhodamin 6G, QY = 95%), typical of PBI^{2+} non-interacting monomers.[165] Conversely, in water (20 mM phosphate buffer pH 7.0) the emission features are red shifted by *ca.* 6 nm with respect to DMF,[166] while emission intensity is significantly abated (Fig. 3.4), with a fluorencence quantum yield of 7% ($[PBI^{2+}] = 10^{-5}$ M), as expected for the PBI^{2+} stacked arrays.[111,146,167] This fluorescence quenching is more significant with concentration increase ($> 10^{-5}$ M, inset in Fig. 3.4). This can be explained considering that: (i) the emission features observed in water are the same observed in DMF (except for the *ca.* 6 nm red shift) and are related to the monomer species, that displays a higher quantum yield than the aggregate; (ii) upon increasing the total concentration of PBI^{2+}, the amount of monomer increases in a non-linear way (the equilibrium is shifted towards aggregated forms, see Fig. 3.2 and inset), justifying the non-linear increase of fluorescence intensity observed at $[PBI^{2+}] > 10^{-5}$ M (Fig 3.4 and inset); (iii) the weak abatement of fluorescence intensity at $[PBI^{2+}] > 10^{-5}$ M (inset in Fig. 3.4) may be ascribed to self-absorption (absorbance > 1).

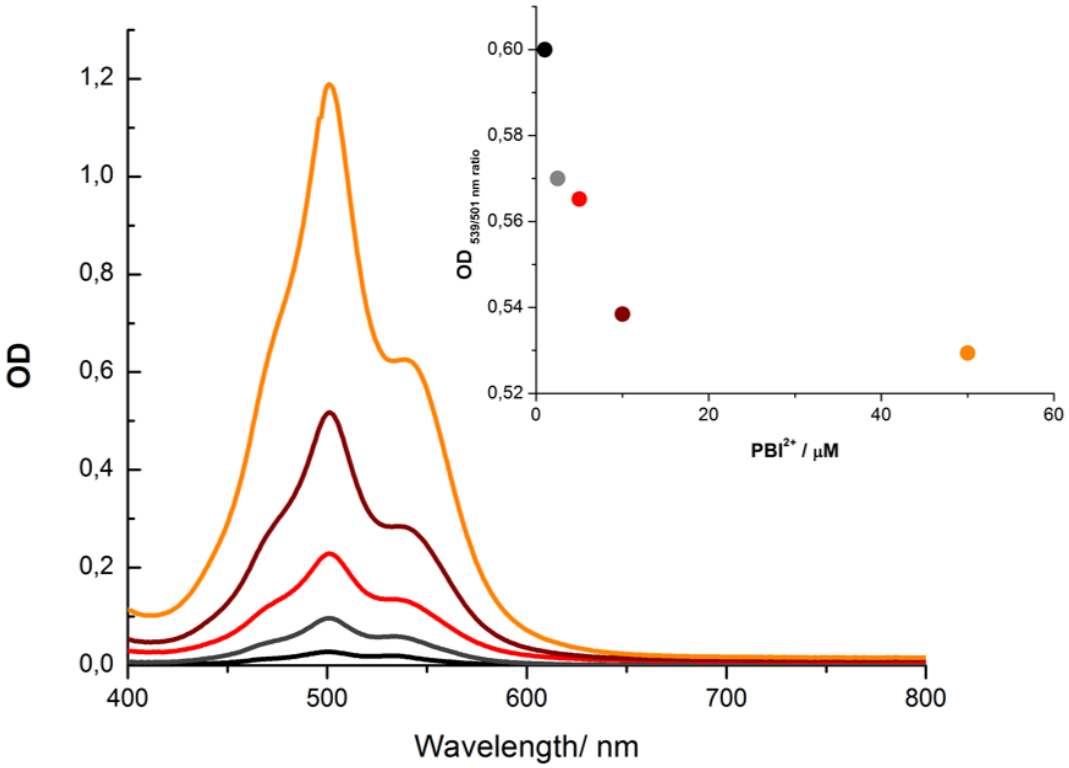

Fig. 3.2 Absorption spectra measured for PBI^{2+} in 20 mM phosphate buffer pH 7.0, R.T., from 10^{-6} M (black line) to 5×10^{-5} M (bright orange line). Inset: ratio of the absorption intensity at 539 nm and 501 nm at different PBI^{2+} concentrations.

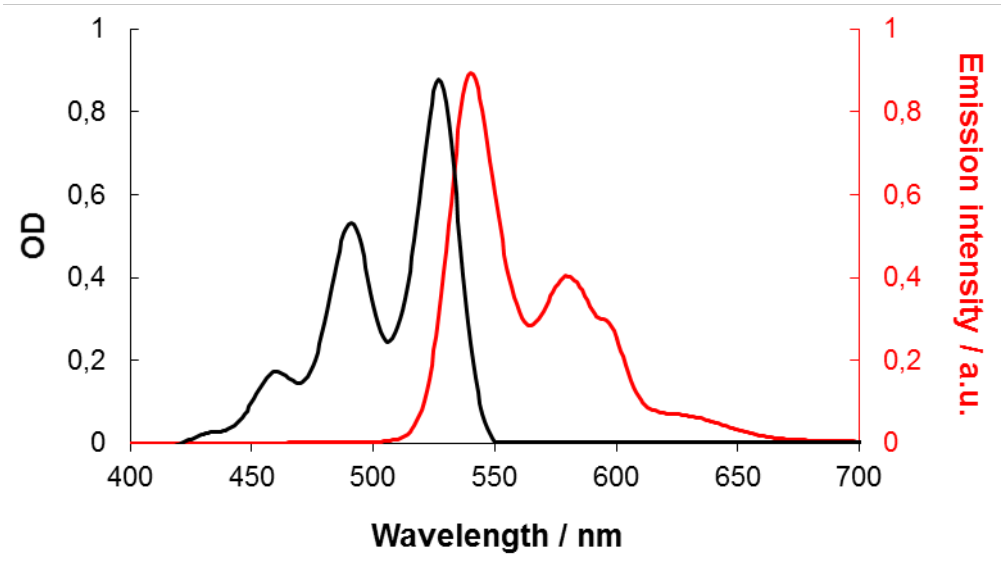

Fig. 3.3 Normalized absorption (black line) and fluorescence spectra (red line) measured for PBI^{2+} (10^{-5} M) in DMF. Excitation wavelength: 350 nm.

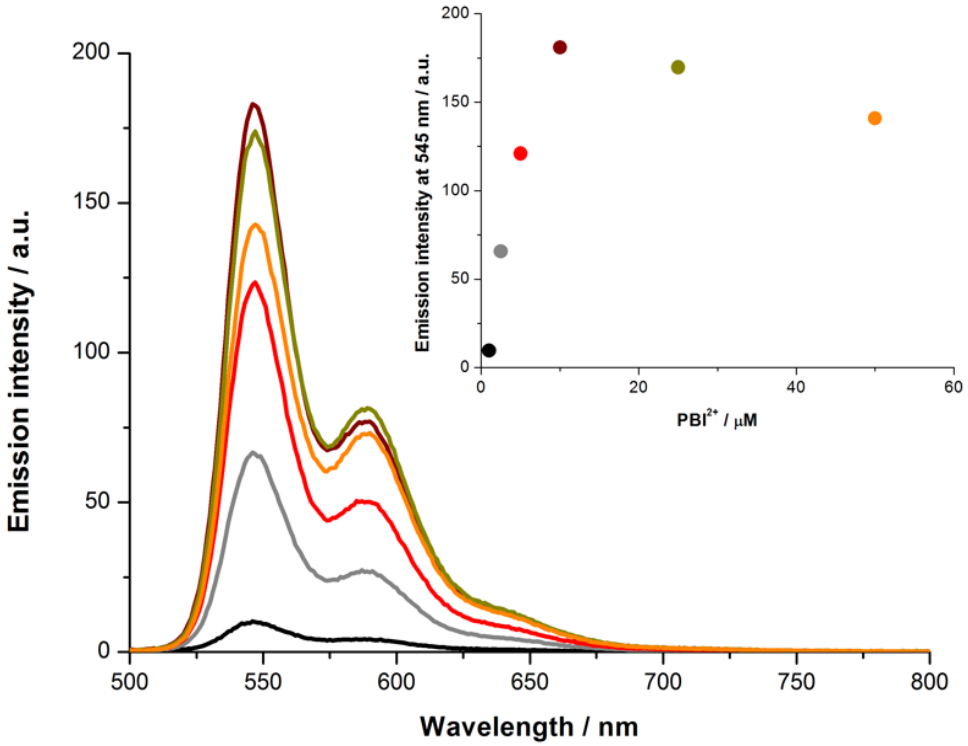

Fig. 3.4 Fluorescence spectra for PBI^{2+} in 20 mM phosphate buffer pH 7.0, R.T., with concentrations ranging from 10^{-6} (black line) to 5×10^{-5} M (bright orange line). Excitation wavelength: 480 nm. Inset: Fluorescence intensity at 545 nm at different PBI^{2+} concentrations. The fluorescence quantum yield (vs Rhodamin 6G, QY = 95%) was found 7% in aqueous phase (stacked arrays) and 90% in DMF (monomers).

The formation of 1-D structures is also confirmed by scanning electron microscopy (SEM) images, where fibers several μm long are observed (Fig. 3.5).

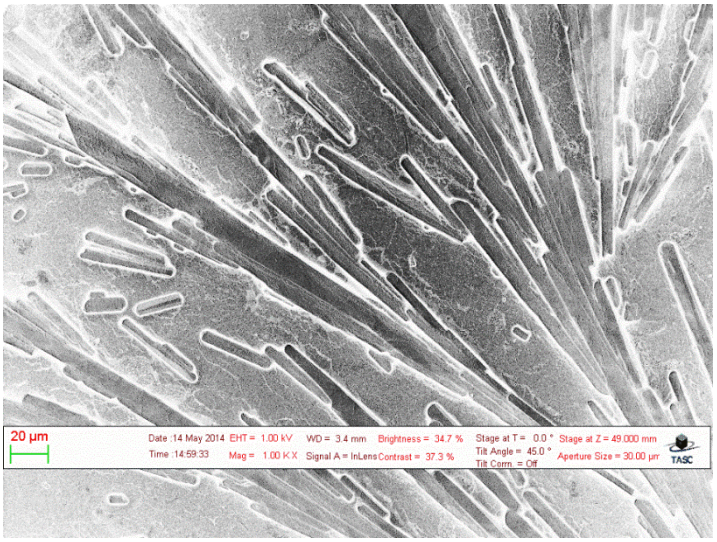

Fig. 3.5 Representative SEM image of PBI^{2+} aggregates formed in 20 mM phosphate buffer pH 7.0 and deposited onto a silicon wafer ($[PBI^{2+}] = 10^{-4}$M).

From Small Angle X-ray Scattering (SAXS) experiments carried out in collaboration with Prof. Heinz Amenitsch in Elettra Sinctrotrone (Basovizza, Trieste), the existence of a large ordered structure in solution is evidenced, while from Wide Angle X-ray Scattering (WAXS) analysis a diffraction peak at 0.36 nm is compatible with a π-π stacking distance, is consistent with the presence of long range ordered aggregates.[168]

Finally, zeta potential analysis can be exploited to detect the presence of charge density, localized in the external surface of the stacked arrays. However, in 20 mM phosphate buffer pH 7, the apparent potential is 0 mV (Fig. 3.6). This could be ascribed to charge balancing of the long strong π-π stacking of PBI^{2+} aggregates from the Cl^- counter anion of PBI^{2+}, or from the $HPO_4^{2-}/H_2PO_4^-$ anions of the buffer.

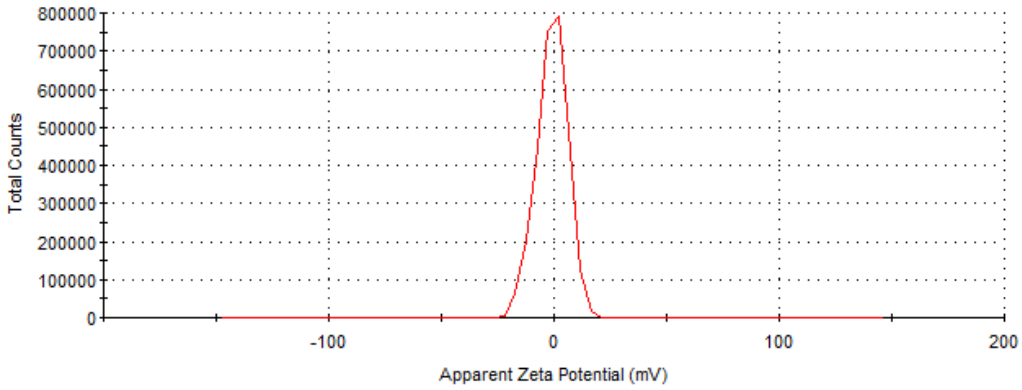

Fig. 3.6 ζ-Potential measurements of PBI^{2+} (2.5×10^{-5} M, red line) in 20 mM phosphate buffer pH 7.0.

The redox properties of PBI^{2+} have been studied by cyclic voltammetry (CV) and spectroelectrochemistry in 0.2 M phosphate buffer at pH 7. These characterizations allow to determine the electron acceptor potential for the ground and excited states.[166,169]

From CV (0.1 mM PBI^{2+} in 0.2 M phosphate buffer pH 7; Indium Tin Oxide, ITO, working electrode, scan rate 50 mV/s - the ITO electrode was used instead of a glassy carbon, where partial adsorption of PBI^{2+} occurs), a first reduction wave with a cathodic peak potential E_{pc} = -0.20 V vs NHE is observed, with a corresponding anodic peak in the reverse scan at +0.03 V vs NHE (Fig. 3.7a). This process is ascribed to the formation of the one-electron reduced form of PBI^{2+},[166,170] as supported by spectroelectrochemical experiments, with the raising of features at 517-800 nm and a bleaching in the 435-517 nm region (isosbestic points at 435 and 517 nm) (Fig. 3.7b-c). From a sygmoidal fitting of the differential absorbance versus the applied potential, an $E_{1/2}$ = -0.10 V vs NHE for the PBI^{2+}/PBI^+ couple is determined (Fig. 3.7d-e).

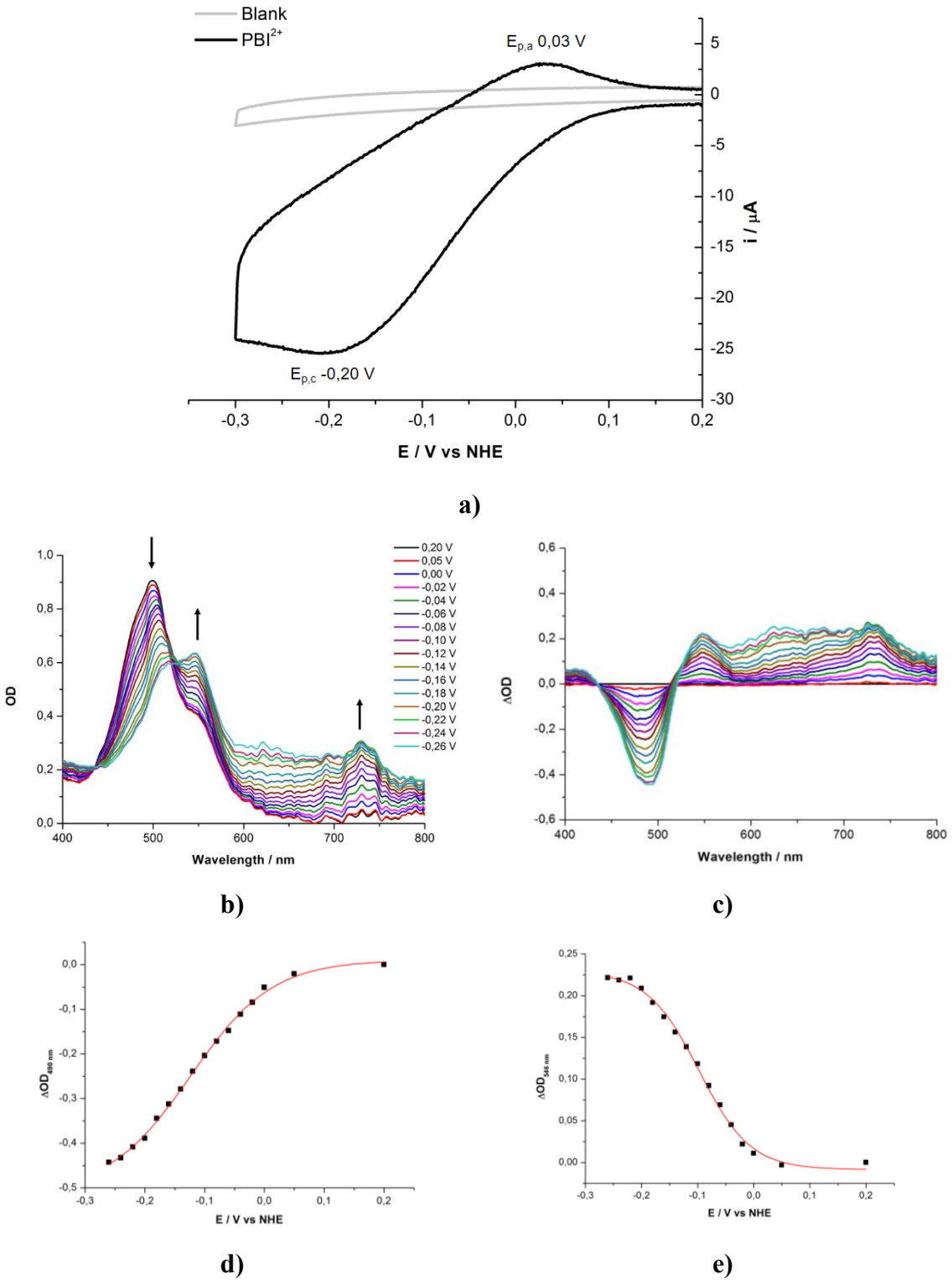

Fig. 3.7 a) Cyclic voltammetry (CV) obtained under cathodic scan for a solution of PBI^{2+} (10^{-4} M in 0.2 M phosphate buffer pH 7.0). Working electrode: ITO; counter electrode: platinum wire; reference electrode: Ag/AgCl (3 M NaCl); scan rate = 50 mV/s. **b)** Spectroelectrochemical measurement obtained under cathodic scan (from 0.20 V to -0.26 V vs NHE) for a solution of PBI^{2+} (5×10^{-4} M in 0.2 M phosphate buffer pH 7.0, cuvette with 1 mm optical path). Working electrode: platinum grid; counter electrode: platinum wire; reference electrode: Ag/AgCl (3 M NaCl); **c)** differential absorption spectra of PBI^{2+} (5×10^{-4} M) under cathodic scan. Sigmoidal fitting of the differential absorption spectra at **d)** 490 nm and **e)** 546 nm versus the applied potential.

Then, from the singlet excited state energy ($E_{0,0}$ PBI^{*2+}) of 2.30 eV obtained from emission experiments, it is possible to determine the redox potential of the couple $PBI^{*2+/1+}$ from the sum of $E_{0,0}$ and $E_{1/2}(PBI^{2+}/PBI^{+})$: this results in $E(PBI^{*2+/1+}) = +2.20$ V vs NHE. which means that the singlet excited state PBI^{*2+} is one of the most powerful photogenerated one-electron oxidants in aqueous solution, significantly more positive than Cerium Ammonium Nitrate (CAN), $E(Ce^{IV}/Ce^{III}) = +1.75$ V vs NHE,[171] often used as sacrificial oxidant in dark water oxidation catalysis, and than $Ru(bpy)_3^{3+}$ (bpy = 2,2'-bipyridine), $E(Ru^{III}/Ru^{II}) = +1.26$ vs NHE, the most investigated photogenerated oxidant for water oxidation applications.[42,171] Based on these results, PBI^{*2+} is expected to promote subsequent photoinduced electron transfer events from the WOC Ru_4POM, driving its step-oxidation to high valent intermediates responsible for water oxidation.[172]

3.2.1.2 Solution Characterization of the PBI^{2+}•Ru_4POM Photosynthetic Ensemble

Spectrophotometric, conductometric and emission titrations

A strong ionic association between PBI^{2+} and Ru_4POM is suggested by a spectrophotometric titration, where modifications of the absorption spectrum of the PBI^{2+} dye are observed upon addition of the Ru_4POM catalyst. The absorption spectrum of PBI^{2+} (2.5×10^{-5} M) features indeed a progressive modification of the two bands at 501 and 539 nm, decreasing in intensity upon addition of Ru_4POM (6.25×10^{-7} - 1.5×10^{-5} M) with isosbestic points at 465 and 562 nm (Fig. 3.8). The overall change in the spectrum indicates a definite change in the aggregation state of PBI^{2+}, by establishing a new equilibrium with the Ru_4POM complex. Moreover, the analysis of the titration curve at 501 nm versus the Ru_4POM equivalents suggests a PBI^{2+}/Ru_4POM association stoichiometry of 5:1 (corresponding to 0.2 equivalents of Ru_4POM, inset in Fig. 3.8), as expected from the ratio of the relative charges (2+ for PBI^{2+}, 10- for Ru_4POM).

The 5:1 stoichiometry is further confirmed by a conductometric titration, where aliquots of Ru_4POM (0 - 4×10^{-5} M) were added to a 10^{-4} M PBI^{2+} solution in 2 mM phosphate buffer pH 7 (Fig. 3.9), observing the equivalent point after addition of 0.2 equivalents of Ru_4POM.

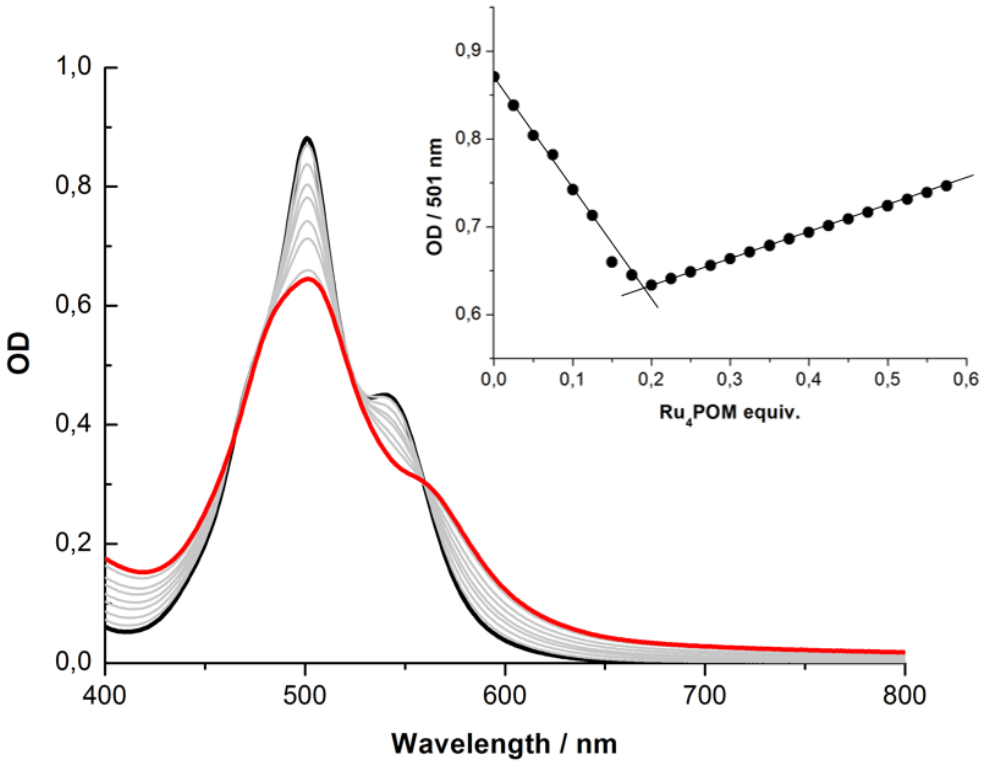

Fig. 3.8 UV-Vis spectrophotometric titration of stacked PBI^{2+} in 20 mM phosphate buffer pH 7 (2.5×10^{-5} M, black line) with Ru_4POM (up to 5×10^{-6} M, 0.2 eq.) that leads to the progressive formation of the PBI^{2+}•Ru_4POM hybrid (red line). Inset: titration curve monitored at 501 nm against the added equivalents of Ru_4POM.

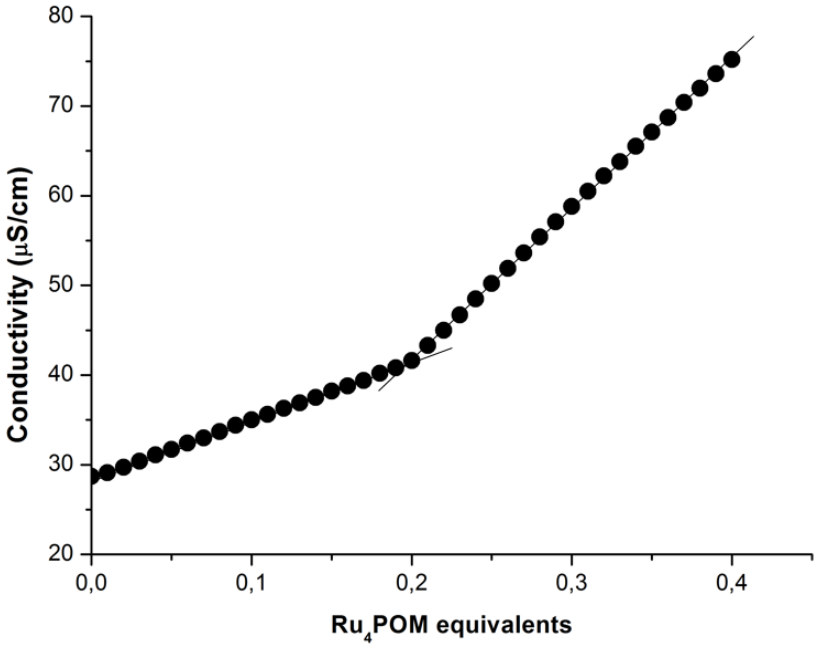

Fig. 3.9 Conductometric titration of PBI^{2+} (10^{-4} M) with Ru_4POM (up to 4×10^{-5} M) in 2 mM phosphate buffer pH 7, R.T.

Fluorescence quenching experiments were then conducted, to prove the effect of PBI^{2+}/Ru_4POM association on the emision properties of PBI^{2+}. The fluorescence of a PBI^{2+} solution (10^{-5} M) is progressively quenched by addition of Ru_4POM (up to 3×10^{-6} M) (Fig. 3.10). Also in this case, the fluorescence is completely quenched upon addition of 0.2 equivalents of Ru_4POM, corresponding to a 5:1 PBI^{2+}/Ru_4POM stoichiometry (inset in Fig. 3.10). The initial addition of Ru_4POM catalyst (up to 0.1 equivalents) results in a non-linear quenching of the fluorescence, possibly due to two competitive effects such as the quenching of the fluorescence due to Ru_4POM and the fluorescence recovery due to PBI^{2+} reorganization into the self-assembled architecture.

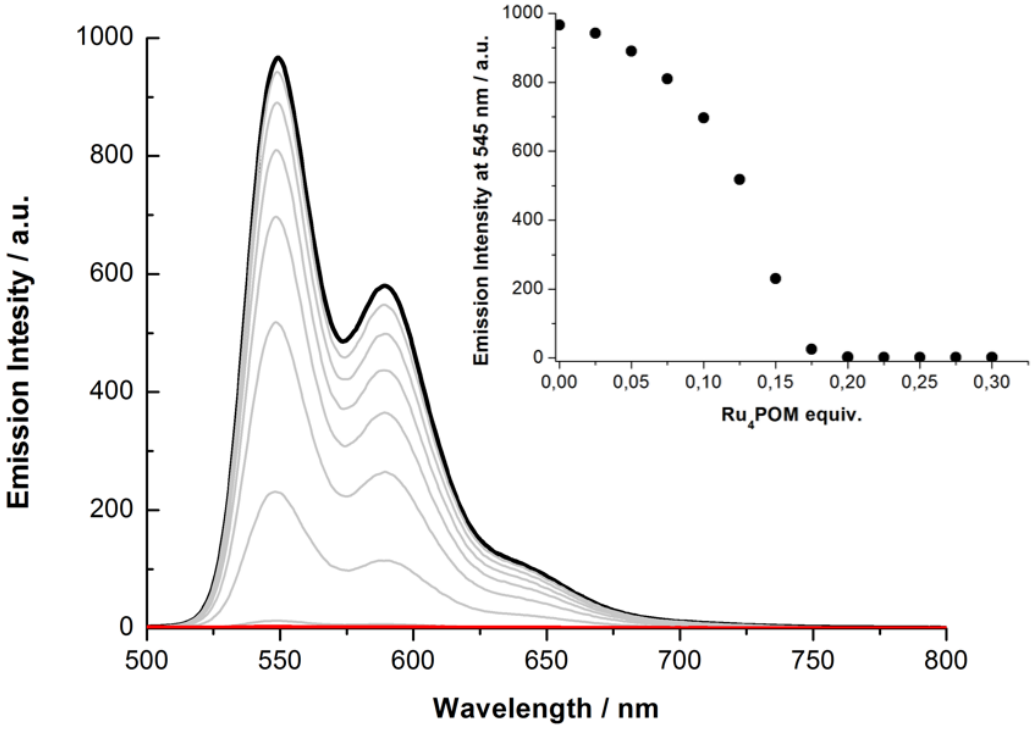

Fig. 3.10 Fluorimetric titration of PBI^{2+} (10^{-5} M, black line) in 20 mM phosphate buffer pH 7.0, R.T., with Ru_4POM from 0 equiv. to 0.3 equiv. (0.2 equiv., red line). Excitation wavelength: 480 nm. Inset: Fluorescence at 545 nm at different Ru_4POM equivalents.

Zeta potential analysis

Zeta potential analysis supports the hybrid formation in agreement with the aforementioned results. The titration of the PBI^{2+} aggregates with Ru_4POM shows a change to positive potential (+17.4 mV) from the initial value of 0 mV observed for PBI^{2+} (2.5×10^{-5} M) after the first Ru_4POM aliquots (0.02 equivalents; 10% of the equivalence point); the positive potential is maintained until nearby the equivalence point (0.2 equivalents of Ru_4POM),

where an inversion to negative potential is observed that reaches a value of -33.2 mV at the PBI^{2+}/Ru_4POM stoichiometry of 5:1, that remains stable upon further addition of Ru_4POM; the stability of this value over time is indicative of stable colloidal solution (Fig. 3.11).[173,174] A possible explanation is that addition of Ru_4POM, below the PBI^{2+}/Ru_4POM stoichiometry of 5:1, exfoliates the PBI^{2+} aggregates, liberating the positive PBI^{2+} particles, thus changing the aggregation state of the pristine assembly. Then, at the PBI^{2+}/Ru_4POM stoichiometry of 5:1, the presence of Ru_4POM is saturating the positive charges of PBI^{2+}, and a negative surface charge is observed. These results are consistent with the SAXS model described below, where a low order is observed due to the formation of a new supramolecular architecture in the presence of Ru_4POM.

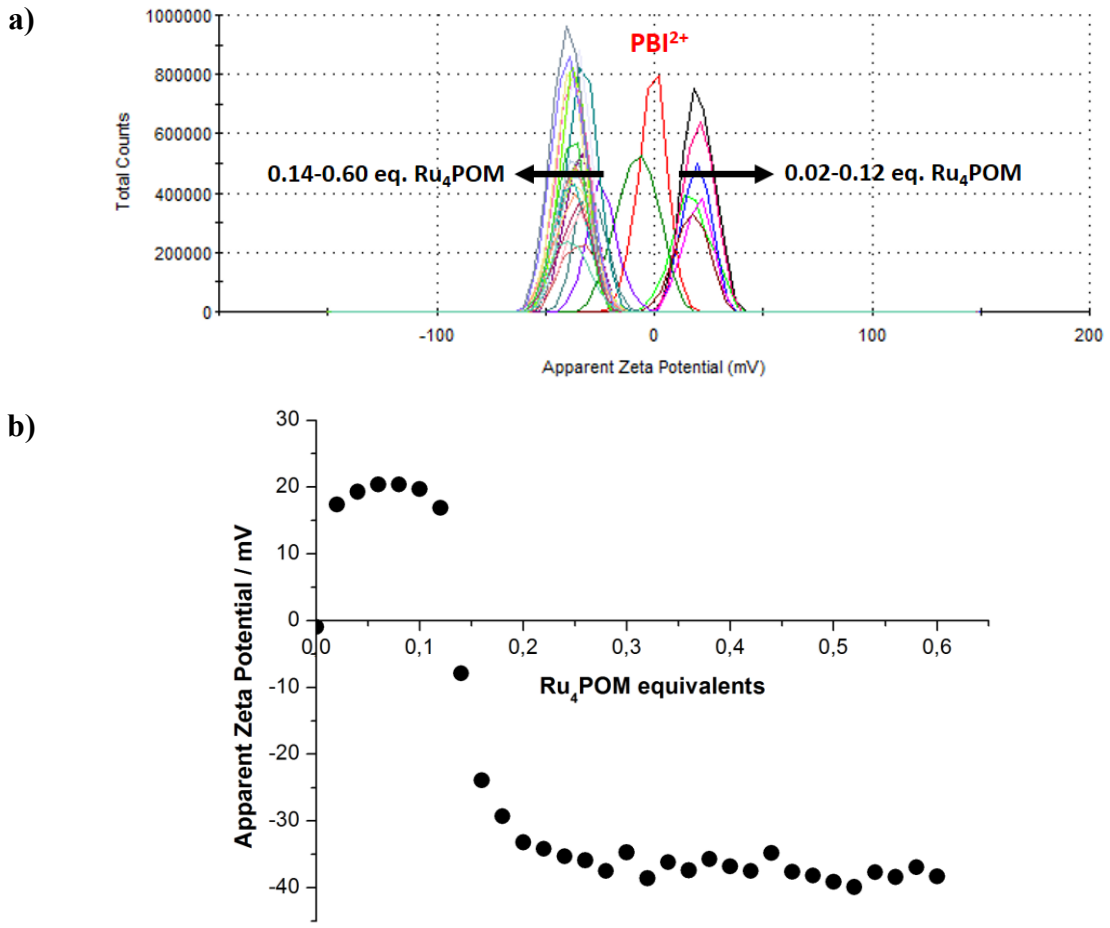

Fig. 3.11 a) ζ-Potential measurements of PBI^{2+} (2.5×10^{-5} M, red line) upon addition of Ru_4POM (up to 0.6 eq., 1.5×10^{-5} M) in 20 mM phosphate buffer pH 7.0. **b)** Apparent zeta potential at different Ru_4POM equivalents.

Control experiments with persulfate anion

In order to evaluate the addition to the PBI^{2+} assembly of the persulfate anion, used as sacrificial electron acceptor in photocatalytic water oxidation experiments (*vide infra*), a

spectrophotometric titration was conducted upon addition of $S_2O_8^{2-}$ to PBI^{2+} leading to the formation of an assembly similar to the one observed in the presence of Ru_4POM (Fig. 3.12). In this case, the abatement of the typical absorption of PBI^{2+} occurs concomitantly to an increase of the absorbance at $\lambda < 430$ nm and $\lambda > 580$ nm, with two isosbetic points at 433 nm and 580 nm. Here, the $PBI^{2+}/S_2O_8^{2-}$ ratio corresponds to 1:3.5 in 20 mM phosphate buffer pH 7 (as indicated by the plot of absorbance at 501 nm versus $S_2O_8^{2-}$ equivalents; inset in Fig. 3.12), possibly due to competition of HPO_4^{2-} and $H_2PO_4^-$ anions. Precipitation of a red solid occurs after addition of an excess of persulfate (> 4 equivalents).

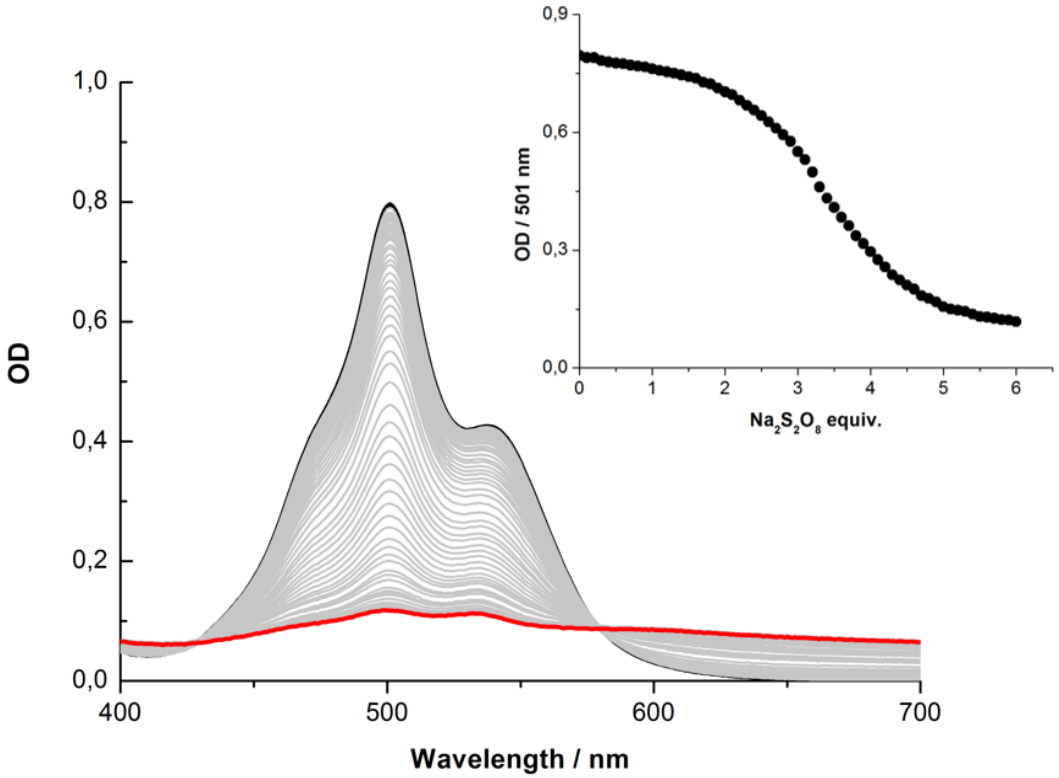

Fig. 3.12 UV-Vis spectrophotometric titration of stacked PBI^{2+} in 20 mM phosphate buffer pH 7 (2.5×10^{-5} M, black line) with $Na_2S_2O_8$ (up to 1.5×10^{-4} M, 6 eq., red line). Inset: titration curve monitored at 501 nm against the added equivalents of $Na_2S_2O_8$.

Finally, the full three-component system ($PBI^{2+}/Ru_4POM/S_2O_8^{2-}$) was studied by spectrophotometric titration, investigating also the effect of the order of addition of the two anions (Ru_4POM or $S_2O_8^{2-}$) to the PBI^{2+} assembly.

This study reveals the irreversible formation of the PBI^{2+} assembly with the first added anion (either Ru_4POM or $S_2O_8^{2-}$), with the addition of the second anion that does not lead to relevant changes in the spectrum shape (Fig. 3.13). This suggests that the second added anion

is not able to intercalate in the preformed aggregate (PBI^{2+}/first added anion). In particular, when Ru_4POM is first added, the typical features of the PBI^{2+}•Ru_4POM hybrid are observed and no relevant changes in the spectrum shape are noticed upon addition of persulfate (Fig. 3.13a). By inverting the order of $Ru_4POM/S_2O_8^{2-}$ addition, the formation of the $PBI^{2+}/S_2O_8^{2-}$ assembly is first observed; an increase in the absorbance is noticed upon addition of Ru_4POM, ascribable to free Ru_4POM in solution (Fig. 3.13b). In this case, the shape of the spectrum has not the typical features of the PBI^{2+}•Ru_4POM hybrid, suggesting that the Ru_4POM catalyst does not intercalate in the $PBI^{2+}/S_2O_8^{2-}$ assembly.

Interestingly, when Ru_4POM and $S_2O_8^{2-}$ are added together to a PBI^{2+} solution, the UV-Vis spectrum obtained resembled the one of PBI^{2+}•Ru_4POM proving a faster and stronger interactions between the two abovementioned species. These studies evidence the importance of the experimental procedure, and in particular of the order of addition of the reactants, in the photocatalytic tests with the three component $PBI^{2+}/Ru_4POM/S_2O_8^{2-}$ system.

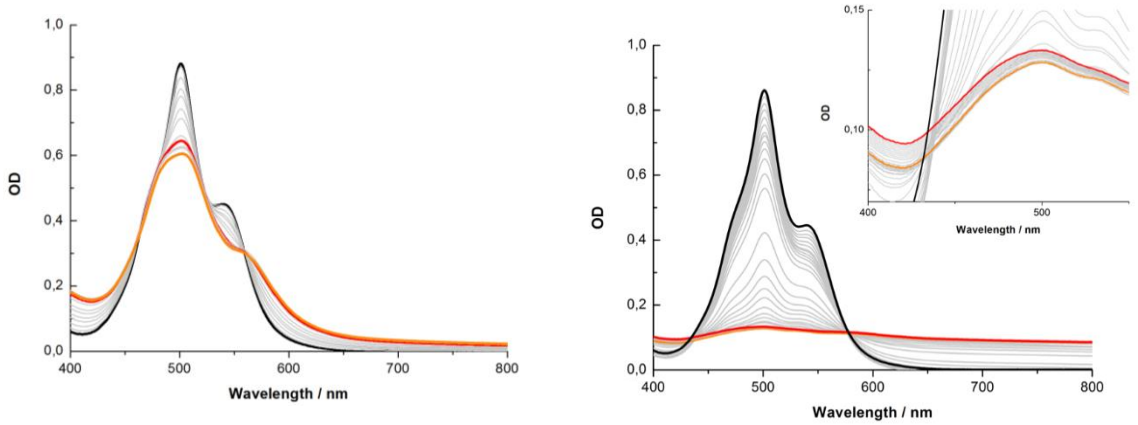

Fig. 3.13 Spectrophotometric titration of PBI^{2+} (2.5×10^{-5} M, black line) in 20 mM phosphate buffer pH 7.0, R.T., **a)** first with Ru_4POM from 0 equiv. to 0.2 equiv. (red line) and successively $Na_2S_2O_8$ from 0 equiv. to 20 equiv. (orange line); sequence of the addition: PBI^{2+}, Ru_4POM, $Na_2S_2O_8$; **b)** first with $Na_2S_2O_8$ from 0 equiv. to 20 equiv. (orange line) and successively Ru_4POM from 0 equiv. to 0.3 equiv. (red line); sequence of the addition: PBI^{2+}, $Na_2S_2O_8$, Ru_4POM.

Small Angle X-Ray Scattering

In order to study the morphology of the formed hybrid assembly, SAXS measurement in collaboration with Prof. Amenitsch in Elettra Sincrotrone (Trieste) were carried out after mixing of PBI^{2+} and Ru_4POM, as well as the sacrificial electron acceptor, $Na_2S_2O_8$ ($[PBI^{2+}] = 2\times10^{-4}$ M, $[Ru_4POM] = 5\times10^{-5}$ M and $[Na_2S_2O_8] = 2\times10^{-2}$ M).

The hybrid PBI^{2+}•Ru_4POM assembly was initially studied: the existance of a nano-porous, two dimensional superstructure with an approximate thickness of 8.2 nm was suggested (plate-like particles). Indeed, the π-π stacking peak observed in the case of PBI^{2+} alone in aqueous solution is now strongly suppressed and broadened, indicating that the long-range order of the preexisting fibers is destroyed upon Ru_4POM addition.

Taking into account the molecular size of the two components, it was possible to attribute the different diffraction peaks observed in SAXS experiments and to hypotesize a structural model for the hybrid (Fig. 3.14). In particular, the d-spacing (*i.e.* the space between planes observed in the structure) of 1.65 nm was attributed to a Ru_4POM-Ru_4POM assembly with intercalated, π-π-stacked PBI^{2+} doublets (distance of 0.36 nm).[168] Instead, the d-spacing of 2.25 nm was attributed to the mean distance between vertically diffracting planes within the nanoplates, in agreement with the long-axis dimensions of the Ru_4POM.

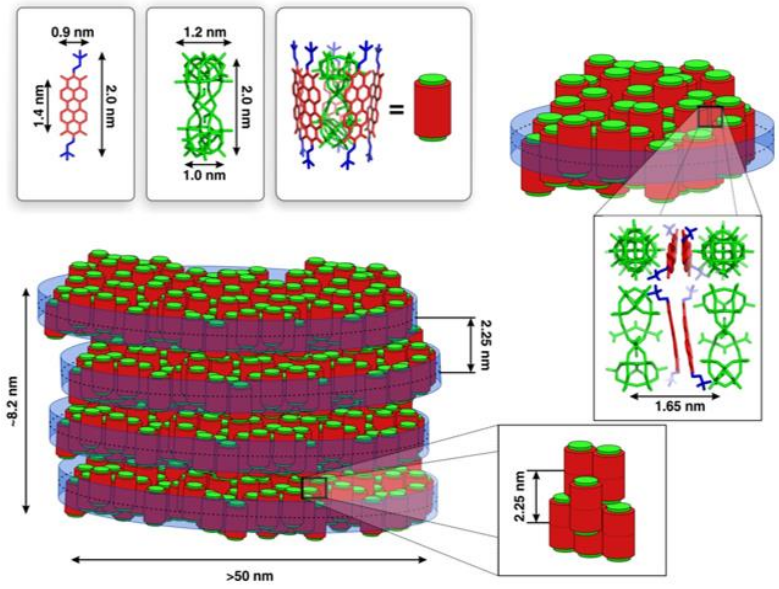

Fig. 3.14 Molecular models of both $PBI^{2+}$and Ru_4POM as well as a figurative representation of the encapsulated building-block based on the stoichiometric 5:1 mixing ratio of PBI^{2+}/Ru_4POM. Single lamellar planes are shown (top right), built of parallel aligned building-blocks with a mean in-plane distance of 1.65 nm. The characteristic motive of this arrangement is the Ru_4POM-PBI-PBI-Ru_4POM coordination shown in the zoom-in. Even though the building-blocks are not necessarily confined to the lamellae, the mean molecular out-of-plane distance corresponds to 2.25 nm (bottom right).

Interestingly, SAXS analysis confirms that addition of $S_2O_8^{2-}$ to a previously self-assembled hybrid PBI^{2+}•Ru_4POM has no impact on the final two-dimensional structure. This indicates high structural stability of the PBI^{2+}•Ru_4POM hybrid material as the molecular motif appears

to be invariant even to anionic persulfate, in agreement with UV-Vis analysis mentioned above.

Transient spectroscopy

Thanks to femtosecond-resolved pump probe spectroscopy in collaboration with Prof. Dirk Guldi in University of Erlangen, the dynamics of the hybrid in solution has been investigated in order to determine the photoassisted evolution of the photosensitizer-catalyst units to a charge-separated state, its lifetime and the competitive recombination kinetics.

The PBI^{2+}•Ru_4POM electron donor-acceptor hybrid was probed in 20 mM phosphate buffer pH 7 upon 530 nm excitation. This experiment shows that the photoexcitation of the hybrid is followed by an intrahybrid charge separation[151,175] to yield a $PBI^{\bullet+}$•$Ru_4POM(h^+)$ radical ion pair state with associated rate constants of 2.5×10^{10} s^{-1} for the formation of the charge separated state and 1.8×10^{9} s^{-1} for the corresponding recombination process (Fig. 3.15).

In such conditions, recombination processes, which occur in hundreds of picoseconds regime are too fast to guarantee the sequential "hole-accumulation" at the water oxidation catalyst. To this aim, the persulfate has been introduced in the system. In this case, the lifetime of $PBI^{\bullet+}$ is 1400 ps (vs 2600 ps in the absence of $S_2O_8^{2-}$), since it can transfer the electron to the persulfate, limiting the dentrimental recombination process. In this way, the Ru_4POM can accumulate the sequential hole needed for water oxidation.

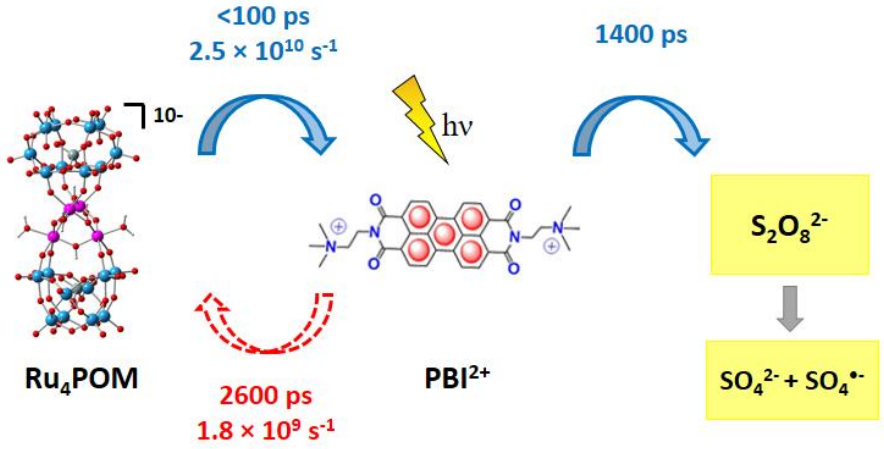

Fig. 3.15 Schematic representation of the electron transfer events occuring in the three component system $PBI^{2+}/Ru_4POM/S_2O_8^{2-}$ in 20 mM phosphate buffer pH 7, with lifetimes and rate constants for the processes obtained by femtosecond-resolved pump probe spectroscopy (in collaboration with Prof. Guldi).

These observations set the basis for the functional up-grade to a complete photocatalytic cycle, leading to oxygen evolution in water under visible light irradiation.

Energy levels for the first elementary steps involved in the photocatalytic cycle for oxygen production for the three component system $PBI^{2+}/Ru_4POM/S_2O_8^{2-}$ have been calculated (the energy of the charge-separated states has been calculated without electrostatic correction applied).[176]

The steps include: (a) light absorption and generation of PBI^{*2+} (Eq. 3.1); (b) electron transfer from Ru_4POM to PBI^{*2+}, forming reduced $PBI^{\bullet+}$ and oxidized $Ru_4POM(h^+)$ (charge separation, Eq. 3.2); (c) electron transfer from $PBI^{\bullet+}$ to $S_2O_8^{2-}$, restoring PBI^{2+} with simultaneous reduction of $S_2O_8^{2-}$ and formation of $SO_4^{\bullet-}$ (Eq. 3.3); (d) further oxidation of $Ru_4POM(h^+)$ to $Ru_4POM(2h^+)$ by $SO_4^{\bullet-}$ (Eq. 3.4); (e) repetition of processes a-d, that lead to the generation of four oxidized catalyst $Ru_4POM(4h^+)$ (Eqs. 3.5-3.8); (f) water oxidation to oxygen by $Ru_4POM(4h^+)$ and regeneration of the catalyst ground state Ru_4POM (Eq. 3.9).

$$PBI^{2+} + h\nu \rightarrow PBI^{*2+} \quad (3.1)$$

$$PBI^{*2+} + Ru_4POM \rightarrow PBI^{\bullet+} + Ru_4POM(h^+) \quad (3.2)$$

$$PBI^{\bullet+} + S_2O_8^{2-} \rightarrow PBI^{2+} + SO_4^{2-} + SO_4^{\bullet-} \quad (3.3)$$

$$Ru_4POM(h^+) + SO_4^{\bullet-} \rightarrow Ru_4POM(2h^+) + SO_4^{2-} \quad (3.4)$$

$$PBI^{2+} + h\nu \rightarrow PBI^{*2+} \quad (3.5)$$

$$PBI^{*2+} + Ru_4POM(2h^+) \rightarrow PBI^{\bullet+} + Ru_4POM(3h^+) \quad (3.6)$$

$$PBI^{\bullet+} + S_2O_8^{2-} \rightarrow PBI^{2+} + SO_4^{2-} + SO_4^{\bullet-} \quad (3.7)$$

$$Ru_4POM(3h^+) + SO_4^{\bullet-} \rightarrow Ru_4POM(4h^+) + SO_4^{2-} \quad (3.8)$$

$$Ru_4POM(4h^+) + 2H_2O \rightarrow Ru_4POM + O_2 + 4H^+ \quad (3.9)$$

A possible competitive route consists in the oxidation of the $PBI^{\bullet+}$ by the sulphate radical $SO_4^{\bullet-}$ instead of Ru_4POM.

Equations 3.1-3.3 are represented in the energy diagram of Fig. 3.16, as processes a-c; the energy of the excited state PBI^{*2+} is +2.30 eV with respect to the ground state PBI^{2+} (Eq. 3.1); the redox potential of the couple $PBI^{*2+}/PBI^{\bullet+}$ has been calculated from the sum of the energy of the excited state and the redox potential of the couple $PBI^{2+}/PBI^{\bullet+}$ (-0.10 V vs NHE, see section 3.2.1.1). Electron transfer from Ru_4POM to PBI^{*2+}, forming $Ru_4POM(h^+)$ and $PBI^{\bullet+}$ (Eq. 3.2) is exergonic by 1.45 eV, as calculated from the difference of the reduction potentials of $PBI^{*2+}/PBI^{\bullet+}$ (+2.20 V vs NHE) and of $Ru_4POM(h^+)/Ru_4POM$ (+0.75 V vs NHE at pH 7; Fig. 3.17). Subsequent electron transfers from oxidized Ru_4POM to PBI^{*2+} are exergonic by 1.18 and 0.94 eV, respectively, as calculated from the difference of the

reduction potentials of $PBI^{*2+}/PBI^{\bullet+}$ (+2.20 V vs NHE) and of redox processes of Ru_4POM (+1.02 - +1.26 V vs NHE, respectively; Fig. 3.17). Electron transfer from $PBI^{\bullet+}$ to $S_2O_8^{2-}$, forming PBI^{2+}, SO_4^{2-} and $SO_4^{\bullet-}$ (Eq. 3.3) is exergonic by 0.72 eV, as calculated from the difference of the reduction potentials of $S_2O_8^{2-}/ SO_4^{2-} + SO_4^{-}$ (0.62 V vs NHE)[177] and of $PBI^{2+}/PBI^{\bullet+}$ (-0.10 V vs NHE).

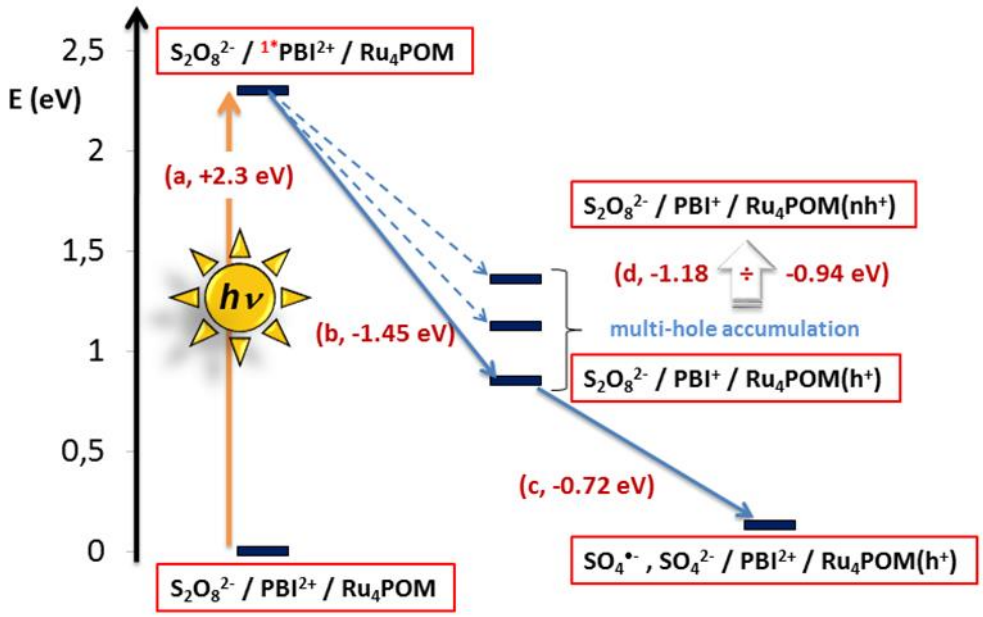

Fig. 3.16 Energy levels for the first elementary steps involved in the photocatalytic cycle for oxygen production in the $PBI^{2+}/Ru_4POM/S_2O_8^{2-}$ system: (a) light absorption and generation of PBI^{*2+}; (b) electron transfer from Ru_4POM to PBI^{*2+}, forming reduced $PBI^{\bullet+}$ and oxidized $Ru_4POM(h^+)$; (c) electron transfer from $PBI^{\bullet+}$ to $S_2O_8^{2-}$, restoring PBI^{2+} with simultaneous reduction of $S_2O_8^{2-}$ and formation of $SO_4^{\bullet-}$. The dotted arrows represent the electron transfer steps between Ru_4POM and PBI^{*2+} leading to multi-hole accumulation on Ru_4POM responsible for water oxidation.

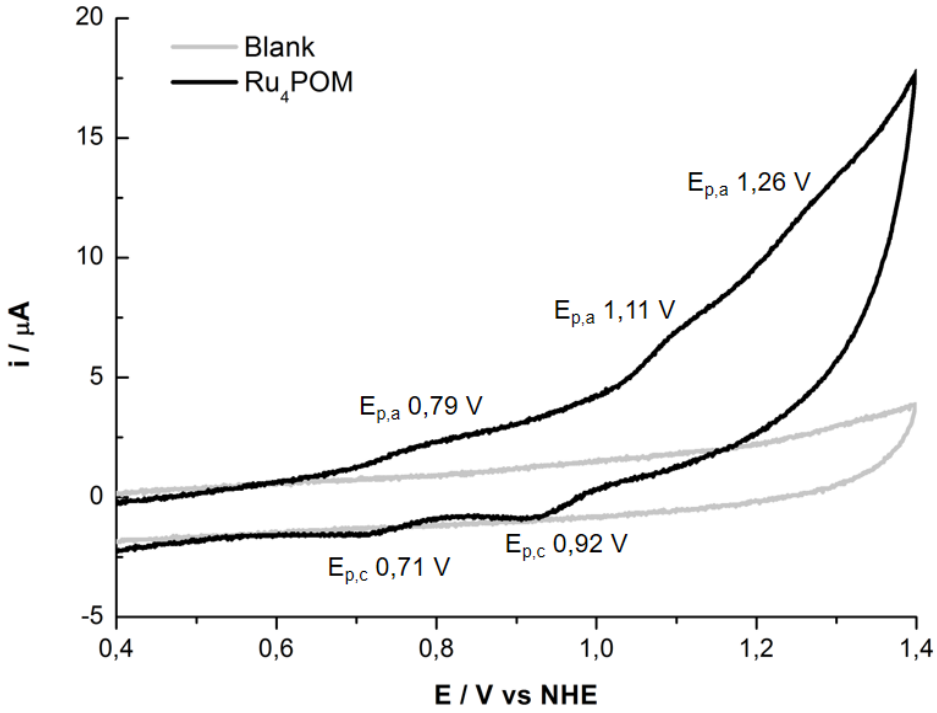

Fig. 3.17 Cyclic voltammetry (CV) obtained under cathodic scan for a solution of Ru_4POM (5×10^{-4} M in Britton-Robinson buffer pH 7 with 0.1 M KNO_3 as supporting electrolyte). Working electrode: platinum; counter electrode: platinum wire; reference electrode: Ag/AgCl (3 M NaCl), potentials are then referred to NHE.[78]

3.2.1.3 Photocatalytic Water Oxidation

After establishing the electron transfer events occurring in the three-component $PBI^{2+}/Ru_4POM/S_2O_8^{2-}$ system, this was tested in light-induced water oxidation experiments at neutral pH (20 mM phosphate buffer pH 7).

Kinetics of oxygen evolution (Fig. 3.18, Table 3.1) were recorded in the presence of PBI^{2+} (10^{-4} M), $S_2O_8^{2-}$ (10^{-3} M), and Ru_4POM (3 - 60×10^{-6} M), upon irradiation with a LED white lamp (4.5 mW/cm^2) (Fig. 3.19). The concentration of sodium persulfate [$S_2O_8^{2-}$] = 10^{-3} M turned out to work the best balancing of two opposing effects: its strong impact on the dynamics of the photogenerated $PBI^{\bullet+}$•$Ru_4POM(h^+)$, promoting hole accumulation on the WOC and the side effect of fostering particle precipitation, which produces an intense light scattering shutting down the reaction.

The kinetics of oxygen evolution depend strongly on the catalyst amount. In particular, the initial rate raises up upon increasing Ru_4POM concentration and it reaches a plateau value for [Ru_4POM] = 20 µM (Fig. 3.20a), corresponding to a PBI^{2+}/Ru_4POM ratio of 5:1, as in

the hybrid material described above. This aggregate may thus be the active species undergoing the catalytic cycle.

In such system, Ru_4POM reaches turnover frequencies up to 1.8×10^{-3} s^{-1} (Fig. 3.20b), which are significantly lower than TOF values observed for the same Ru_4POM catalyst in a photoactivated cycle for water oxidation with $Ru(bpy)_3^{2+}$ photosensitizer and $S_2O_8^{2-}$ as electron acceptor (TOF up to 8×10^{-2} s^{-1}).[73,74] This is however justified on the basis of the operating photophysical mechanism, and in particular on the concentration of the oxidants that feed the Ru_4POM catalyst in the two cases: in the case of PBI^{2+}, the one-electron oxidant is the excited state PBI^{*2+}, whose steady state concentration is intrinsically low (5.79×10^{-15} M; see appendix A.1 for the calculation). In the cycle with $Ru(bpy)_3^{2+}$ as the photosensitizer, the oxidant is the $Ru(bpy)_3^{3+}$, photogenerated by oxidative quenching of $Ru(bpy)_3^{2+}$ with persulfate and accumulable in the reaction solution.[42,75]

For this reason, also the quantum yield for the photocatalytic system with PBI^{2+} is quite low, up to 0.023 (see appendix A.2 for the calculation), if compared with the one observed with a Ru(II) polypyridine photosensitizer (up to 0.30).[54]

The lowering of TON upon increasing Ru_4POM concentration (Fig. 3.20c, see Table 3.1) can be likely due to the modification of the photosynthetic assembly which fosters unproductive recombination pathways. Indeed, the photosynthetic assembly is helded together by non-covalent interactions and it can undergo to dynamic evolution, in terms of composition and size, depending on the relative amount of the ionic components.

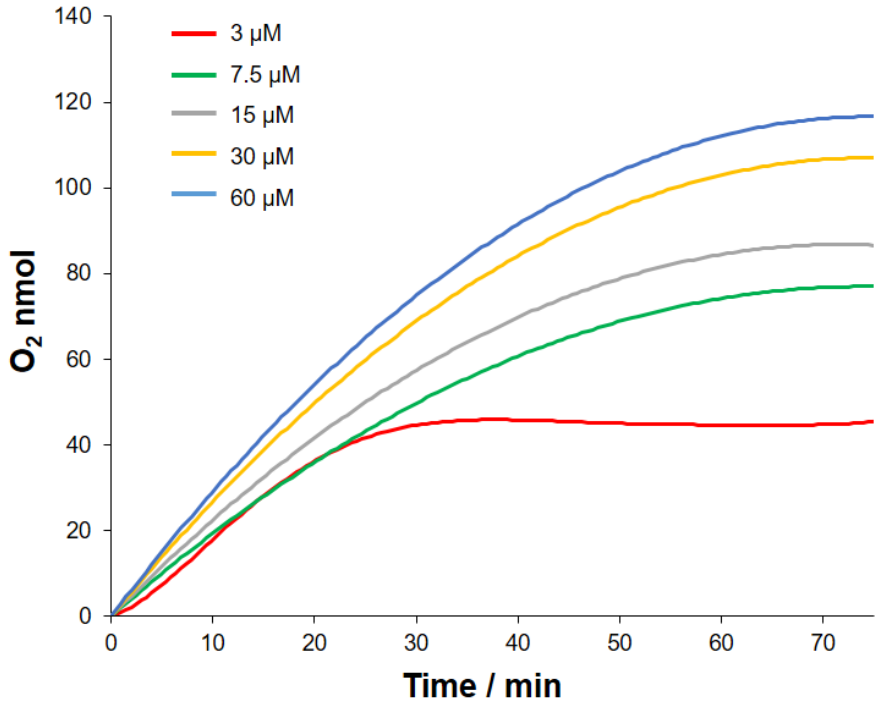

Fig. 3.18 Photoinduced water oxidation catalysis by PBI^{2+}•Ru_4POM under visible light irradiation. Oxygen evolution kinetics monitored in 20 mM phosphate buffer pH 7 upon irradiation with a LED white lamp (4.5 mW/cm^2) of PBI^{2+} (10^{-4} M) in the presence of Ru_4POM (3 - 60×10^{-6} M) and $S_2O_8^{2-}$ (10^{-3} M). The photosystem performance is evaluated according to data in Table 3.1.

Table 3.1 Photocatalytic oxygen evolution by PBI^{2+}•Ru_4POM with $S_2O_8^{2-}$ as sacrificial oxidant in water.

Ru_4POM [μM]	nmol O_2[a] (TON)[b]	Rate/10^{-3} [c] [nmol O_2 s^{-1}] (TOF/10^{-3}, s^{-1})[d]	Yield,[e] [%]	Quantum yield
3	49±7 (3.6±0.5)	24±4 (1.8±0.3)	2.2	0.009
7.5	82±10 (2.4±0.3)	29±7 (0.86±0.20)	3.6	0.011
15	93±14 (1.4±0.2)	45±3 (0.67±0.04)	4.1	0.017
30	110±7 (0.8±0.1)	60±5 (0.44±0.04)	4.9	0.022
60	120±21 (0.4±0.1)	62±7 (0.23±0.03)	5.3	0.023

Reaction conditions: 4.5 mL of 20 mM phosphate buffer pH = 7.0, [PBI^{2+}] = 10^{-4} M, [$S_2O_8^{2-}$] = 10^{-3} M, irradiation with a spotlight (4.5 mW/cm^2). [a] nmol O_2 determined after 80 min. [b] Turnover number (TON) calculated as μmol O_2 per μmol Ru_4POM. [c] Initial rate of O_2 production determined as the linear kinetic slope. [d] Turnover frequency (TOF) calculated as TON per second. [e] Determined on persulfate conversion after 80 min.

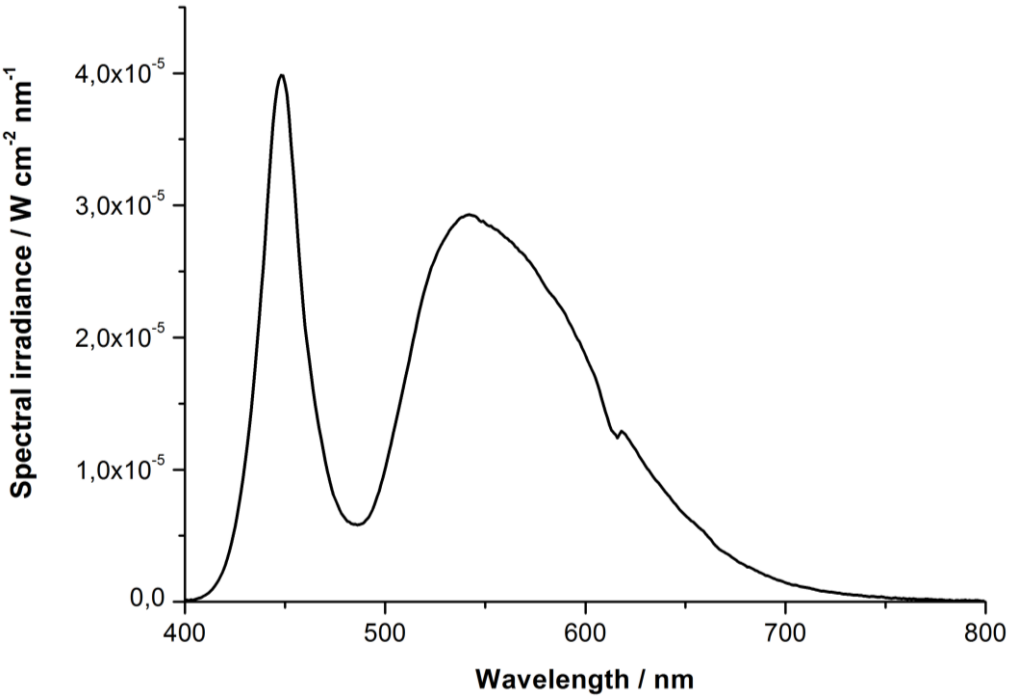

Fig. 3.19 Emission spectrum of the LED white lamp used in photocatalytic experiments. The area has been normalized (the resolution of the spectum is 1 nm), in accordance to the 4.5×10^{-3} W/cm^2 irradiance power of the lamp.

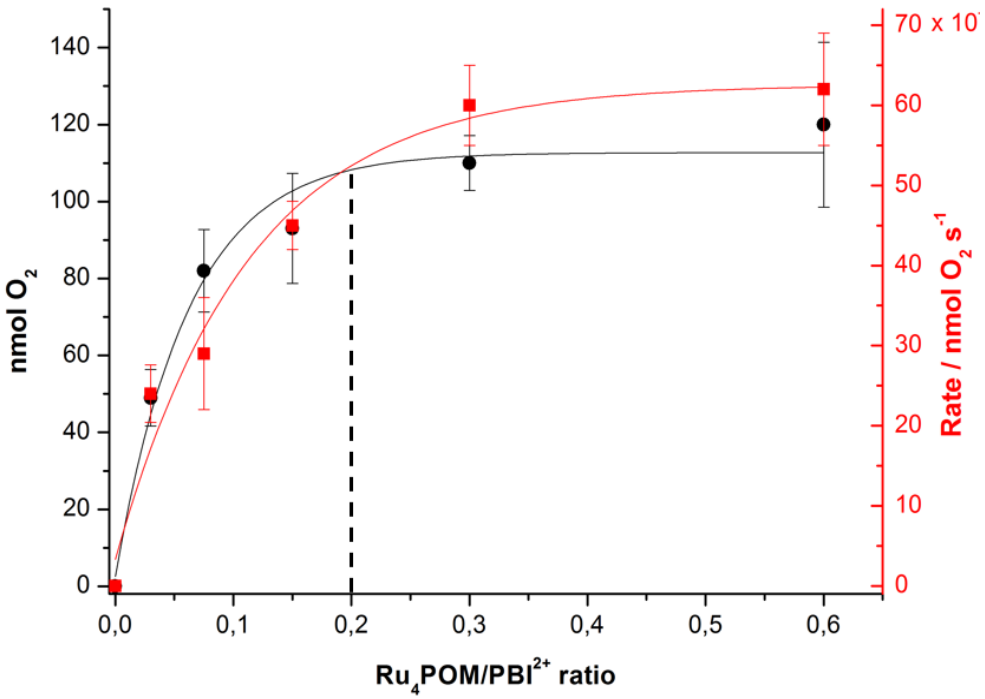

a)

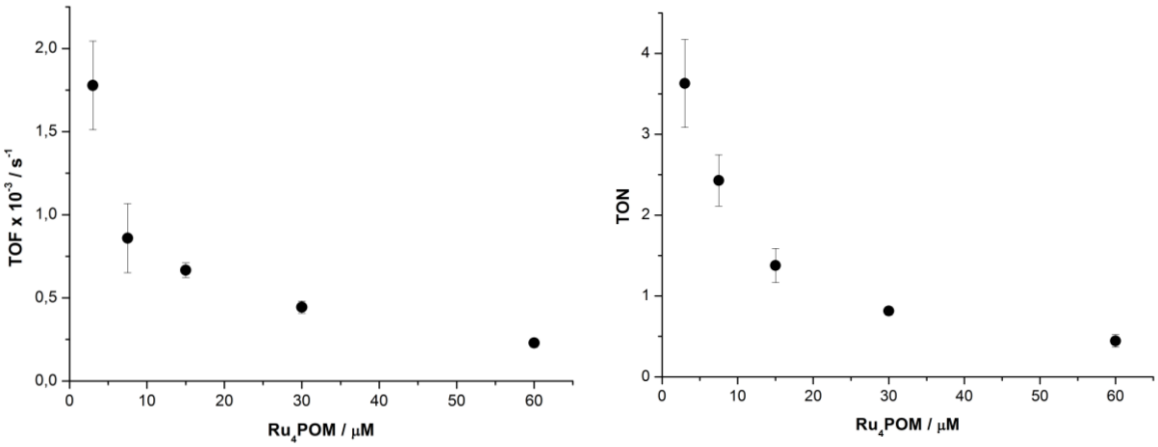

Fig. 3.20 Plots of parameters related to oxygen evolution kinetics versus Ru_4POM concentration. $[PBI^{2+}] = 10^{-4}$ M, $[S_2O_8^{2-}] = 10^{-3}$ M in 20 mM phosphate buffer pH 7.0, R.T. **a)** Plot of O_2 production (left axis, black plot) and of the initial rate of O_2 production (right axis, red plot) versus Ru_4POM/PBI^{2+} ratio; exponential fittings of the data are reported (solid lines) to underline the trend of data. **b)** Plot of initial rate of oxygen production in terms of turnover frequency (TOF), versus Ru_4POM concentration. **c)** Plot of oxygen production in terms of turnover number (TON) versus Ru_4POM concentration.

Absorption analysis of the reaction mixture confirms the robustness of the ensemble over time, since the typical features of the PBI^{2+}•Ru_4POM hybrid are preserved after photoinduced oxygen evolution (Fig. 3.21). This is markedly different from what observed in the case of $[Ru(bpy)_3]^{2+}$, where a sensitive photosensitizer degradation can be observed during photocatalysis, leading to irreversible deactivation.

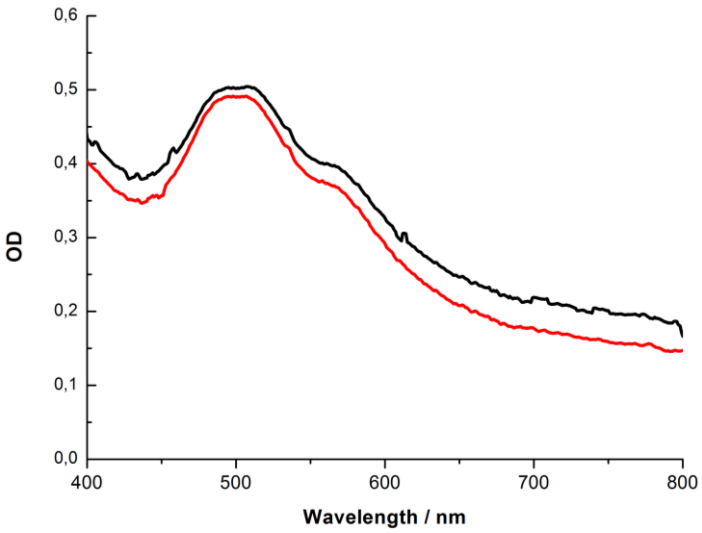

Fig. 3.21 Absorption analysis (optical path 1 mm) of the reaction mixture before (black line) and after (red line) oxygen evolving catalysis. Conditions: $[PBI^{2+}] = 10^{-4}$ M, $[Ru_4POM] = 15\times10^{-6}$ M and $[S_2O_8^{2-}] = 10^{-3}$ M in 20 mM phosphate buffer pH 7.0. The slight shift of the baseline is likely due to light scattering by aggregates.

Importantly, all the experiments showed a pleateau after 60 minutes of reaction, with no further oxygen evolution, even after sonication of the mixture, or following injections of sacrificial agent. Oxygen inhibition is thus ascribed to byproducts deriving from the reduction of the sacrificial electron acceptor. Indeed, upon addition of SO_4^{2-} (2×10^{-4} M, the product of $S_2O_8^{2-}$ reduction) to a freshly prepared reaction mixture, the oxygenic activity of the system is inhibited, possibly due to competing electrostatic interactions in the assembly that hamper the electron flow dynamics in the catalytic cycle.

3.2.2 Solution Characterization in H_2O/HCl pH 2.5

Characterization of the PBI^{2+}/Ru_4POM aggregates have been performed also in acidic solution (aqueous HCl, pH 2.5), since part of the study will be devoted to photoelectrochemical water oxidation with visible light under acidic environment (see Chapter 4).

3.2.2.1 Solution Characterization of PBI^{2+}

As observed at pH 7, the absorption and the fluorescence spectra for PBI^{2+} at pH 2.5 (5×10^{-7} - 5×10^{-5} M, in aqueous HCl, Fig. 3.22-3.23) confirm the presence of the PBI^{2+} aggregates; the fluorencence quantum yield (vs Rhodamin 6G, QY = 95%) in this medium was found 5%.

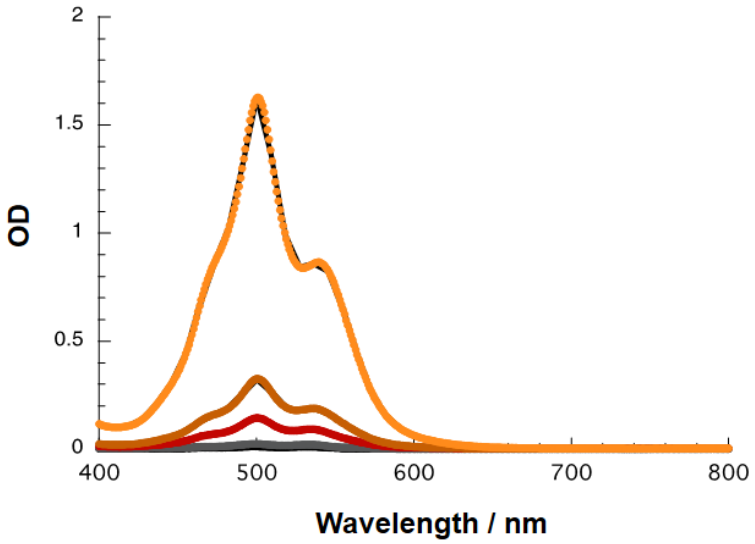

Fig. 3.22 Absorption spectra measured for PBI^{2+} in H_2O/HCl pH 2.5, R.T., from 5×10^{-7} M (black line) to 5×10^{-5} M (bright orange line).

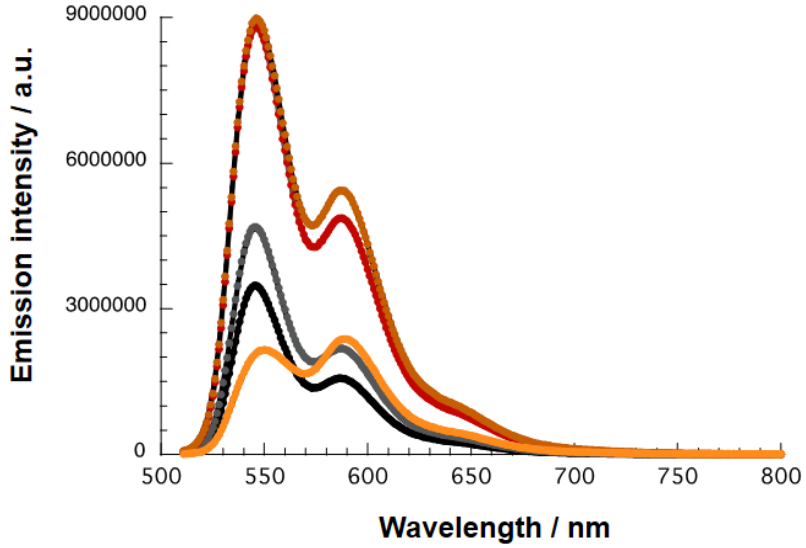

Fig. 3.23 Fluorescence spectra measured for PBI^{2+} in H_2O/HCl pH 2.5, R.T., with concentrations ranging from 5×10^{-7} (black line) to 5×10^{-5} M (bright orange line). Excitation wavelength: 480 nm.

The formation of several μm long fibers has been observed by atomic force microscopy (AFM) (Fig. 3.24).

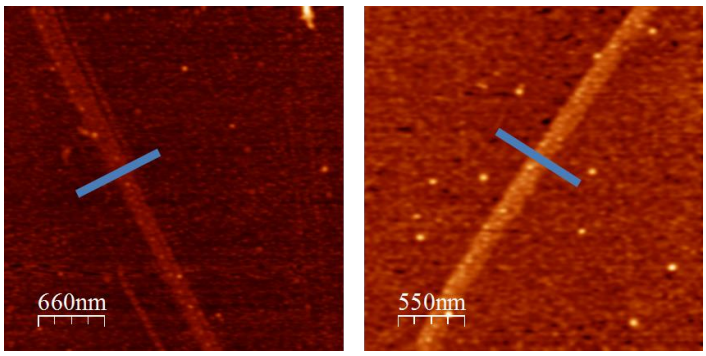

Fig. 3.24 Representative AFM images of PBI^{2+} aggregates ($[PBI^{2+}] = 2.85\times10^{-5}$ M) formed in H_2O/HCl pH 2.5 and deposited onto a silicon wafer.

Finally, from zeta potential analysis, a positive apparent potential of 28.5 mV for a 2.5×10^{-5} M PBI^{2+} solution confirms the positive surface charge of the fibers (Fig. 3.25).

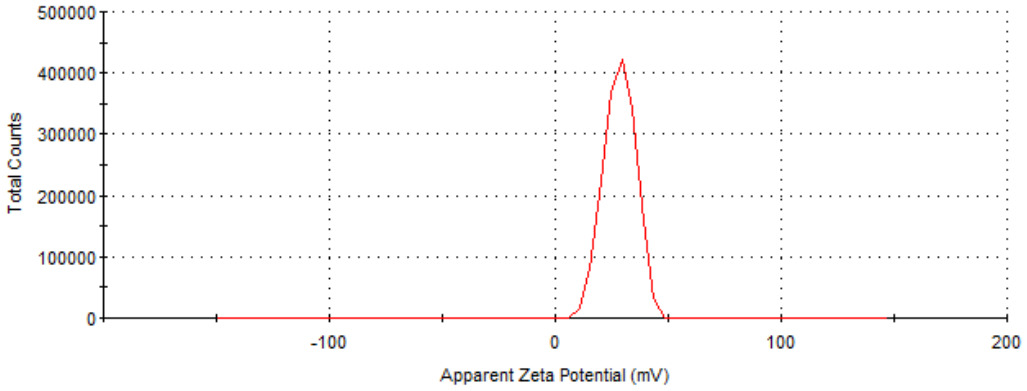

Fig. 3.25 ζ-Potential measurements of PBI^{2+} (2.5×10^{-5} M, red line) in H_2O/HCl pH 2.5.

The redox potentials of PBI^{2+} have been measured also at this acidic pH by CV (Fig. 3.26). In particular, two quasi-reversible waves are observed with half-wave reduction potentials $E_{1/2} \approx$ -0.12 V vs NHE and -0.44 V vs NHE, which are ascribed to the formation of the PBI^{2+} mono- and bis-reduced species, respectively.[166,170]

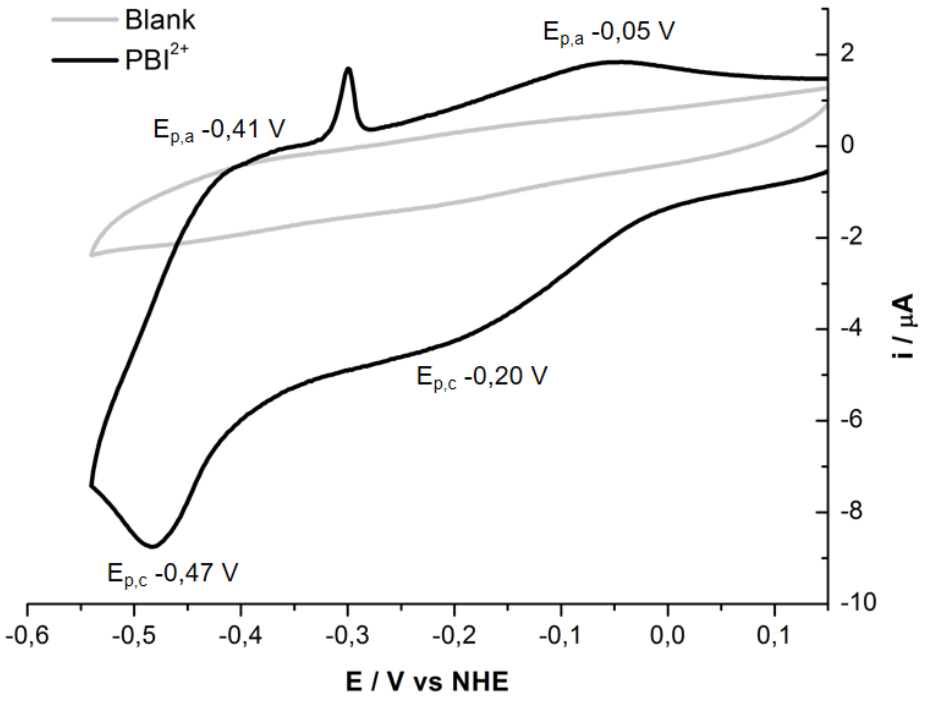

Fig. 3.26 Cyclic voltammetry (CV) obtained under cathodic scan for a solution of PBI^{2+} (5×10^{-4} M in H_2O/HCl pH 2.5, 0.1 M NaCl as supporting electrolyte). Working electrode: glassy carbon; counter electrode: platinum wire; reference electrode: Ag/AgCl (3 M NaCl). The spike observed under the anodic scan can be ascribed to the adsorbed PBI^{2+} on the electrode surface.

The calculated redox potential E(PBI^{*2+}) is +2.20 V vs NHE, the same value as the one obtained at pH 7, and is still expected to promote electron transfer events from Ru_4POM leading to water oxidation.

Moreover, oxygen evolution in acidic media represents a future challenge. In such environment, the thermodynamic requirement for water oxidation is less favorable than at neutral pH, since E(O_2/H_2O) = (1.23 - 0.0592×pH) V vs Normal Hydrogen Electrode. However a system working at acidic pH permits the coupling of water oxidation and proton reduction to hydrogen processes to occur under the same conditions.

In Chapter 4, the use of tungsten oxide (WO_3) as semiconductor for the building of photoanodes will be considered. In particular, this metal oxide can be used only in acidic media due to its poor chemical stability at neutral and basic pH.[178–180]

3.2.2.2 Solution Characterization of the PBI^{2+}•Ru_4POM Photosynthetic Ensemble

Similarly to what observed at pH 7, the strong ionic association between PBI^{2+} and Ru_4POM is confirmed also at pH 2.5. Also in this case, the absorption spectrum of PBI^{2+} (2.5×10^{-5} M) features a progressive modification of the two bands at 501 and 539 nm, decreasing in intensity upon addition of Ru_4POM (6.25×10^{-7} - 1.5×10^{-5} M) with isosbestic points at 460 and 564 nm (Fig. 3.27). Interestingly, at pH 2.5 the PBI^{2+}/Ru_4POM association stoichiometry from the titration curve results 4:1 (corresponding to 0.25 equivalents of Ru_4POM) (inset in Fig. 3.27).

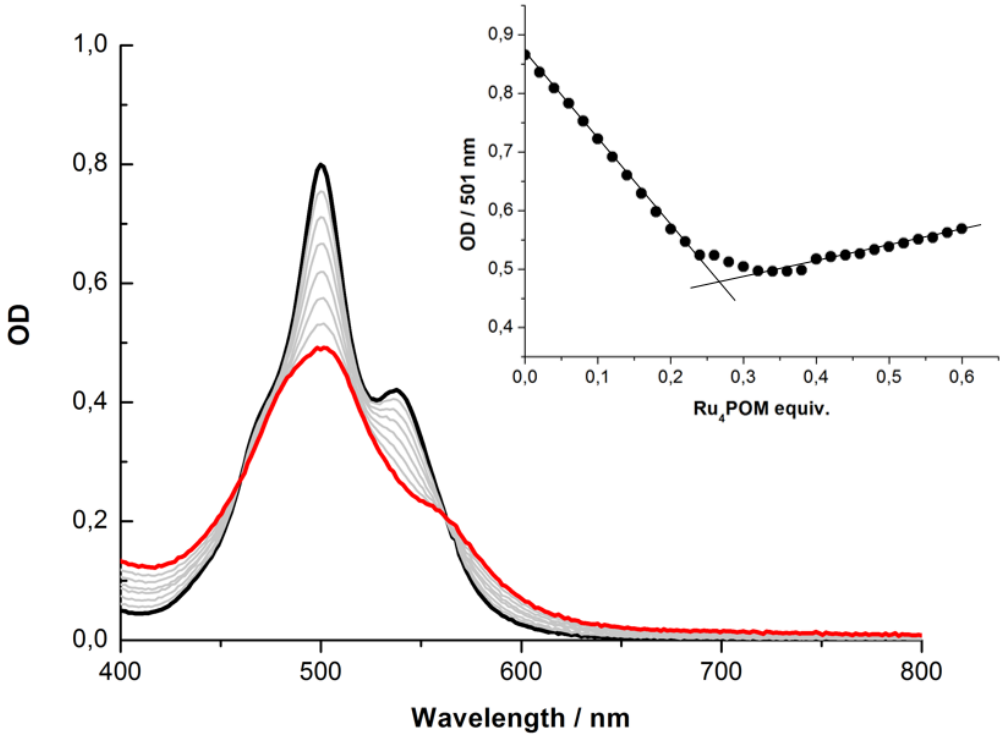

Fig. 3.27 UV-Vis spectrophotometric titration of stacked PBI^{2+} in H_2O/HCl pH 2.5 (2.5×10^{-5} M, black line) with Ru_4POM (up to 6.25×10^{-6} M, 0.25 eq.) that leads to the progressive formation of the PBI^{2+}•Ru_4POM hybrid (red line). Inset: titration curve monitored at 501 nm against the added equivalents of Ru_4POM.

This 4:1 PBI^{2+}/Ru_4POM stoichiometry was further confirmed by conductometric titration (Fig. 3.28).

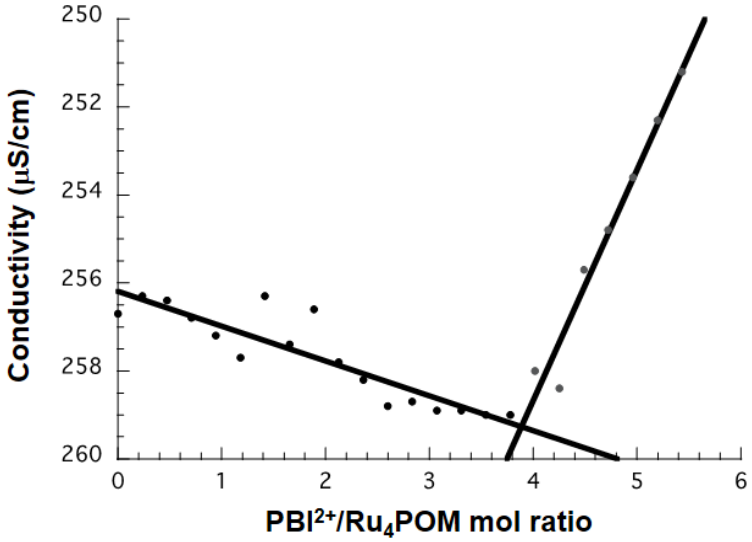

Fig. 3.28 Conductometric titration of Ru_4POM (5×10^{-5} M) with PBI^{2+} (up to 3×10^{-4} M) in H_2O/HCl pH 2.5, R.T.

The spectrophotometric titration was conducted also by addition of $S_2O_8^{2-}$ to PBI^{2+} (Fig. 3.29). The abatement of the typical absorption of PBI^{2+} is observed together with the increase of the absorbance at $\lambda < 443$ nm and $\lambda > 573$ nm, with two isosbetic points at 443 nm and 573 nm. At pH 2.5, the titration has a 1:1.5 $PBI^{2+}/S_2O_8^{2-}$ stoichiometry, as indicated by the plot of absorbance at 501 nm versus $S_2O_8^{2-}$ equivalents (inset in Fig. 3.29). Also in this case, precipitation of a red solid occurs after addition of an excess of persulfate.

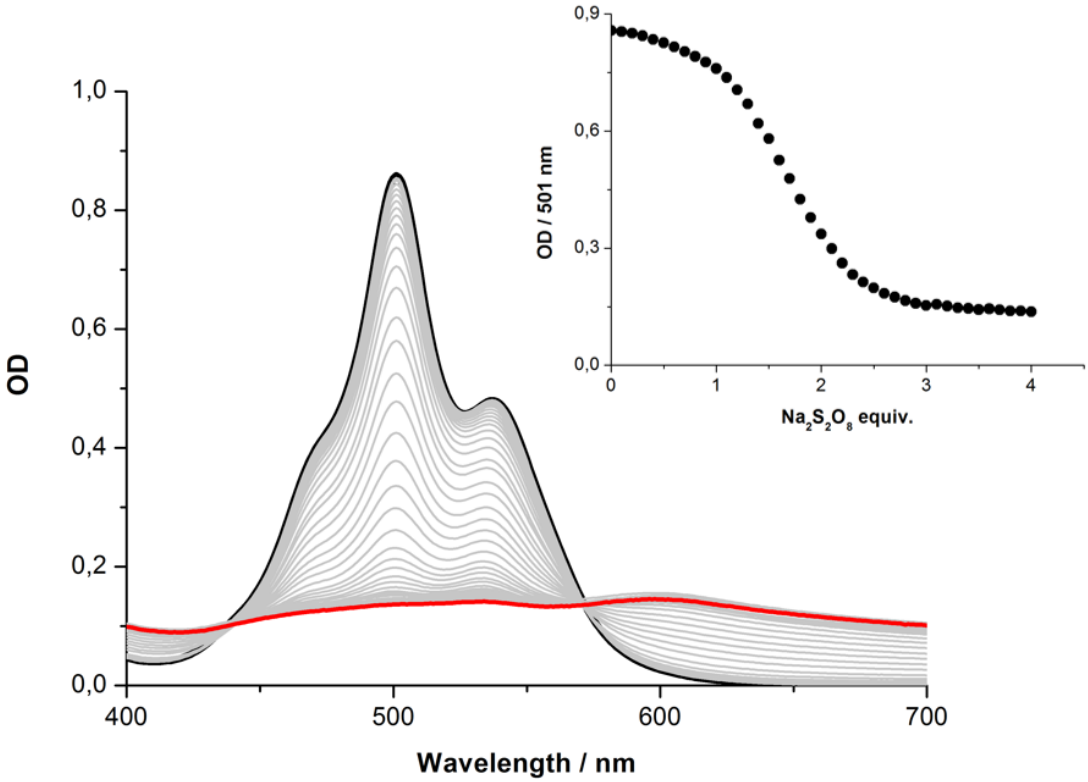

Fig. 3.29 UV-Vis spectrophotometric titration of stacked PBI^{2+} in H_2O/HCl pH 2.5 (2.5×10^{-5} M, black line) with $Na_2S_2O_8$ (up to 10^{-4} M, 4 eq., red line). Inset: titration curve monitored at 501 nm against the added equivalents of $Na_2S_2O_8$.

The full three-component system was studied, observing similar results as in the case of pH 7 and confirming the importance of the different addition order of the species.

Fluorescence experiments performed upon excitation at 480 nm confirm strong electronic interactions between the PBI^{2+}/Ru_4POM components, as the PBI^{2+} emission intensity undergoes to an exponential decrease upon addition of Ru_4POM (up to 3×10^{-6} M; Fig. 3.30). At pH 2.5, this leads to a complete quenching of the PBI^{2+} emission after addition of 0.25 Ru_4POM equivalents confirming the 4:1 PBI^{2+}/Ru_4POM stoichiometry.

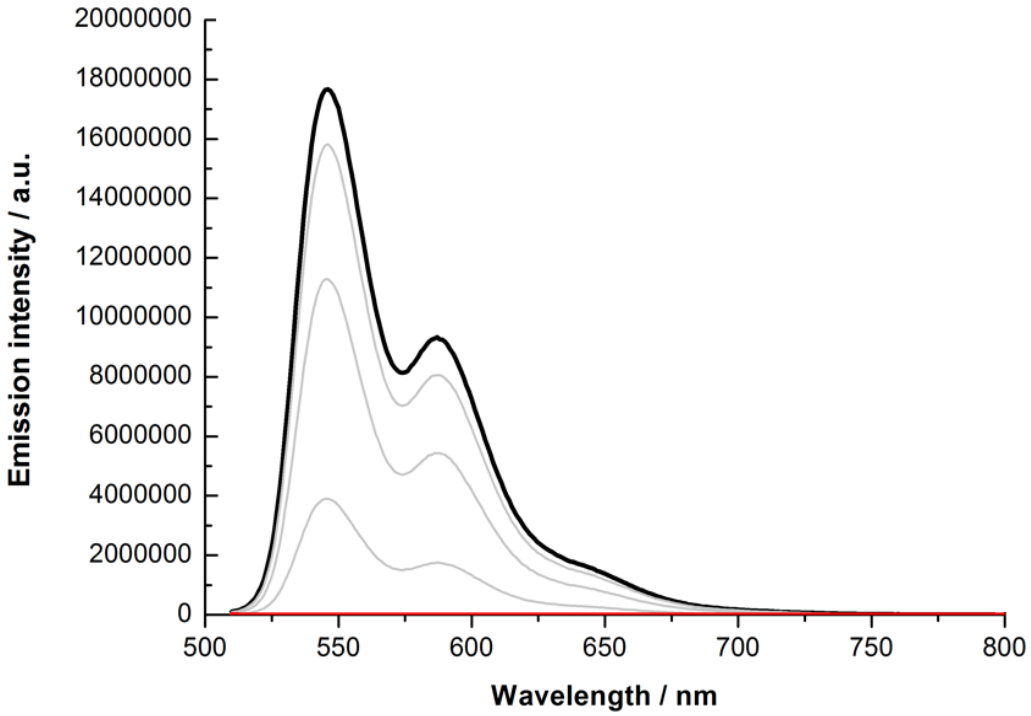

Fig. 3.30 Fluorimetric titration of PBI^{2+} (10^{-5} M, black line) in H_2O/HCl pH 2.5, R.T., with Ru_4POM from 0 equiv. to 0.3 equiv. (0.25 equiv., red line). Excitation wavelength: 480 nm.

A remarkable inversion of the surface charge displayed by the PBI^{2+} stacks (2.5×10^{-5} M) is conveniently monitored by zeta potential analysis, whereby the initial positive value of +28.5 mV for the apparent zeta potential turns to -31.9 mV upon Ru_4POM addition (0.25 equivalents) (Fig. 3.31).

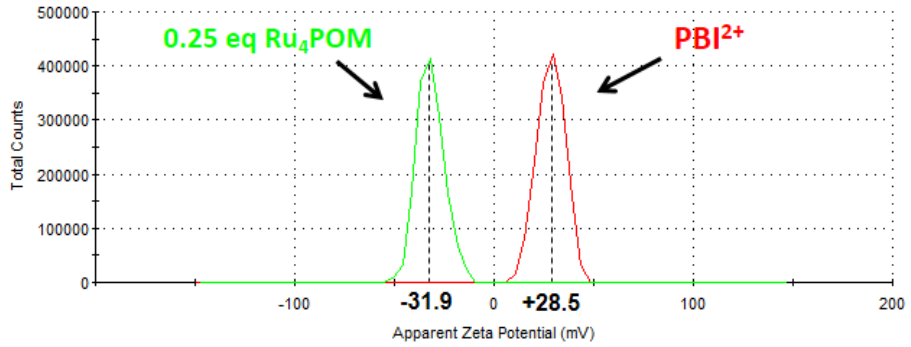

Fig. 3.31 ζ-Potential measurements of PBI^{2+} (2.5×10^{-5} M, red line) upon addition of Ru_4POM (0.25 eq, 6.25×10^{-6} M, green line) in H_2O/HCl pH 2.5.

From femtosecond-resolved pump probe spectroscopy, the dynamics of the hybrid in acidic solution has been investigated (Fig. 3.32).

Also in this case, the photoexcitation of PBI^{2+}•Ru_4POM hybrid is followed by a charge separation leading to the formation of $PBI^{\bullet+}$•$Ru_4POM(h^+)$ radical ion pair state. Even if the electron transfer from the Ru_4POM to the PBI^{*2+} occurs in less than a hundred of picoseconds as in neutral pH, the electron transfer from the $PBI^{\bullet+}$ to persulfate occurs in only 69 ps. However, also the recombination process is really fast and it occurs in 136 ps (Fig. 3.32).

For this reason, the cataytic activity of the system in light driven oxygen evolution was tested only at pH 7.

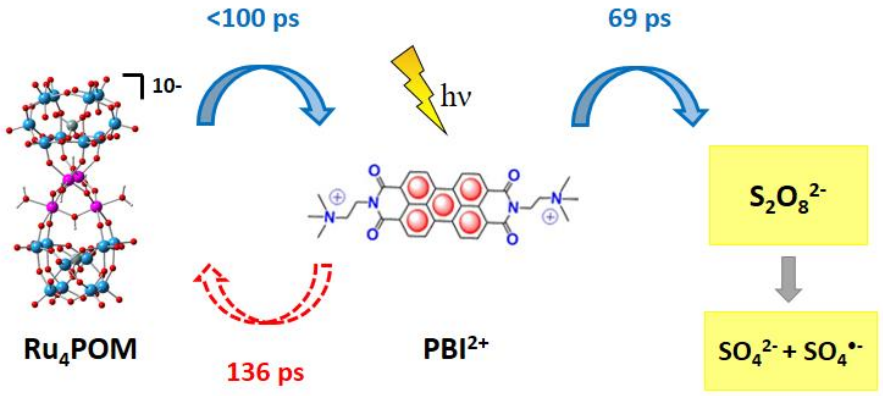

Fig. 3.32 Schematic representation of the electron transfer events occuring in the three component system $PBI^{2+}/Ru_4POM/S_2O_8^{2-}$ in H_2O/HCl pH 2.5, with lifetimes for the processes obtained by femtosecond-resolved pump probe spectroscopy (in collaboration with Prof. Guldi).

3.3 Conclusions and perspectives

In this Chapter, a novel supramolecular assembly has been presented exploiting electrostatic interaction between a metal-free cationic photosensitizer, PBI^{2+}, and a robust totally inorganic polyanionic WOC, Ru_4POM. Indeed, the use of metal-free dyes is nowadays appealing, thank to the low cost and abundance of raw materials, in the view of industrial applications.

So far, only few examples of metal-free photosensitizers for light driven water oxidation have been reported in literature. In particular, a covalent dyad with a perylene bisimide and a molecular iridium catalyst has been reported by Wasielewski and co-workers.[146] In such assembly, the electron transfer between the catalyst and the photosensitizer occurs in less

than 10 ps upon excitation of the dye. However, also charge recombination is relatively fast (tens of ps depending on the solvent), perhaps a result of structural changes at the iridium center upon oxidation.

In the PBI^{2+}/Ru_4POM system, strong interactions between the two components are observed from characterization in aqueous solution at pH 7 and at pH 2.5, with a definite stoichiometry. In particular, the PBI^{2+}/Ru_4POM ratio is 5:1 at pH 7 and 4:1 at pH 2.5. From SAXS analysis, a model for the hybrid assembly has been hypothesized, consisting of a nano-porous two dimensional architecture composed by Ru_4POM-Ru_4POM assembly with intercalated, π-π-stacked PBI^{2+} doublets. Interestingly, this self-assembled structure mimics the natural supramolecular photosystem, where the oxygen evolving complex is surrounded by a couple of chlorophylls, the photosensitizers of the natural photosynthesis. As in Nature, this superstructure allows the interactions of the components, leading to fast electron transfer events between them. Indeed, they occur upon illumination of the assembly in the presence of persulfate within hundreds of picoseconds.

These results set the basis for the use of this system for photocatalytic water oxidation in solution. This has been tested in phosphate buffer solution at pH 7, where oxygen evolution has been observed. In particular, the oxygen production reaches 120 nmol, with TOF up to 1.8×10^{-3} s^{-1}, and a quantum yield for oxygen production of 0.023. These results can be ascribed to the operating photophysical mechanism, where the excited state of the PBI^{2+}, PBI^{*2+}, is the one-electron oxidant promoting the electron transfer cascade: indeed, its steady state concentration is intrinsically low (5.79×10^{-15} M). Similarly, the low TON values observed (up to 3.6) can be due to the dynamic evolution in terms of composition and size of the photosynthetic assembly, since it is held together by non-covalent interactions.

Interestingly, from the plot of initial rate against Ru_4POM concentration a plateau is reached for [Ru_4POM] = 20μM, corresponding to a PBI^{2+}/Ru_4POM ratio of 5:1, as in the hybrid aggregate, that may thus be the active species undergoing the catalytic cycle.

Unfortunately, the system undergoes deactivation after *ca.* 60 minutes due to the byproduct formation from the sacrificial electron acceptor. These results paves the way for a further investigation of the system, possibly coupling it with a n-type semiconductor in order to avoid such competing phenomena that hamper the catalytic performance of the system in solution. The building of photoanodes with this kind of assembly will be considered in the next chapter.

4 PBI^{2+}/Ru_4POM-sensitized WO_3 photoanodes for water oxidation with visible light

4.1 Introduction

The ultimate goal of artificial photosynthesis is the building of regenerative devices, capable of splitting water upon solar irradiation without any electrical applied bias. With this aim, scientists have focused their attention on photoelectrochemical cells (PECs), and in particular on dye-sensitized photoelectrochemical cells (DS-PECs, ideally capable of exploiting the visible part of the solar emission), that drive water oxidation and proton reduction in their anodic and cathodic compartments, respectively (see section 1.7). In this case, light absorption by a suitable chromophore leads to a charge separation state that provides the electrochemical driving force for the whole process, while the catalysts are needed to overcome the kinetic barrier associated to the redox processes.

In this Chapter a photoanode for water oxidation will be presented (Fig. 4.1), supporting on a nanostructured WO_3 semiconductor the bis-cationic perilene bisimide photosensitizer/ ruthenium polyoxometalate catalyst assembly, PBI^{2+}/Ru_4POM, already used in homogeneous solution at pH 7 in the presence of persulfate (Chapter 3). Electrons injected from the PBI^{2+}/Ru_4POM into the conduction band of WO_3 will be transferd to the cathodic compartment, a Pt electrode, and exploited to reduce protons to hydrogen.

Bignozzi, Prato and co-workers reported photoanodes using this same PBI^{2+} dye as photosensitizer and IrO_2 nanoparticles as WOC onto different porous nanocrystalline metal oxide films as semiconductors.[115] In particular, electron injection of PBI^{2+} was effective on WO_3 ($k_{inj} > 10^8$ s^{-1}), while the unproductive, back electron transfer from the semiconductor to the oxidized dye is three order of magnitude slower. Moreover, 4-fold enhancement of the photocurrent density in the presence of spin coated IrO_2 nanoparticles was observed, reaching 70 μA/cm^2 at 0.75 V vs NHE in aqueous 0.1 M $NaClO_4$ pH 3 under illumination with a solar simulator (AM 1.5 G light) with 435 nm long-pass filter.

Based on this study and on the results of the PBI^{2+}/Ru_4POM supramolecular assembly previously investigated in solution, the photoanode has been prepared exploiting the capability of aggregation of PBI^{2+}/Ru_4POM into a self-assembled architecture with a definite stoichiometry.

The electrochemical and photoelectrochemical characterization of the *nano*WO_3| PBI^{2+}| Ru_4POM photoanodes will be presented: a 2-fold enhancement of the photocurrent density in the presence of Ru_4POM was observed, reaching 44 μA/cm^2 at 0.75 V and 75 μA/cm^2 at 1.20 V vs NHE in aqueous 0.1 M $NaClO_4$ pH 3, under illumination with a solar simulator

(AM 1.5 G light) with a 450 nm long-pass filter. The performance of the photoelectrodes was then evaluated in terms of turnover frequency (TOF), turnover number (TON), incident photon-to-current efficiency (IPCE) and absorbed photon-to-current efficiency (APCE). In particular, TOF and TON values resulted to be 0.026-0.048 s^{-1} and 3.8-8.5 at 0.75 V and 1.20 V vs NHE, respectively. The calculated IPCE and APCE values were 0.50% and 1.30%, respectively. These values observed with the Ru$_4$POM catalyst are comparable or slightly higher than those previously reported by Bignozzi and co-workers with the *nano*WO$_3$| PBI^{2+}| IrO$_2$ photoelectrodes (IPCE 0.6% and APCE 0.8%).[115]

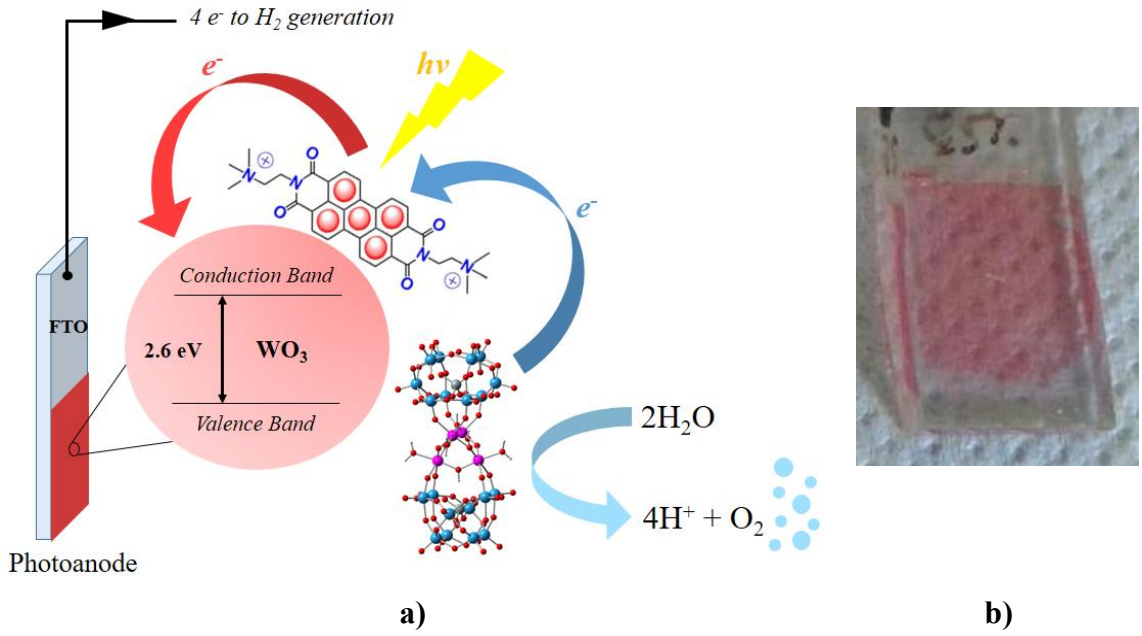

Fig. 4.1 a) Schematic representation of the PBI^{2+}/Ru$_4$POM-sensitized nanostructured WO$_3$ photoanodes, with electron transfer processes represented by arrows; **b)** picture of the photoelectrode.

4.2 Results and Discussion

Following the work by Bignozzi, Prato and co-workers on the PBI^{2+}-sensitized WO$_3$ and considering the promising results of PBI^{2+}-Ru$_4$POM in homogeneous solution (Chapter 3), a photoanode with PBI^{2+}-sensitized WO$_3$ and Ru$_4$POM as WOC has been prepared and characterized in collaboration with Prof. Bignozzi (University of Ferrara) and Prof. Bonchio (University of Padova).

The nanostructured tungsten oxide (*nano*WO$_3$) has been selected since PBI^{2+} spontaneously adsorbs on its nanocrystalline surface, and performs efficient photoinduced electron

injection into *nano*WO_3 conduction band, as proved by transient absorption spectroscopy.[115] The preparation of the photoanodes and the following experiments were performed in aqueous acidic medium, in particular at pH 3 (10^{-3} M HCl/0.1 M $NaClO_4$), in order to preserve the WO_3 film, which is sensitive to neutral and basic conditions.[178–180] However, the band gap of WO_3 is about 2.6 eV and its conduction band edge is below the hydrogen reduction potential; for this reason, a minimum applied bias is needed in order to drive the overall water splitting process with a simple Pt cathode (Fig. 4.1).

4.2.1 *nano*WO_3| PBI^{2+}| Ru_4POM photoanodes preparation

nanoWO_3| PBI^{2+} photoanodes were prepared according to literature procedure,[115] starting from the spin coating of a colloidal solution of tungsten oxide nanoparticles onto a fluorine-doped tin oxide (FTO)-coated glass slide. The electrode was then sintered at 550°C for 45 minutes in order to obtain the nanocrystalline WO_3 layer in the monoclinic phase. The procedure was repeated six times to have the optimized electrode with six spin-coated layers. In the UV-Vis spectra of the *nano*-WO_3 electrodes, some artefacts can be observed, due to interference phenomena of the incident radiation which is reflected at the interfaces between the different layers: for this reason, the UV-Vis absorption spectra of the FTO| *nano*WO_3 samples can differ from each other. However, in the characterization spectra of the PBI^{2+}/Ru_4POM sensitized *nano*WO_3 electrodes (*vide infra*), the spectrum of the blank sample (FTO| *nano*WO_3) is always subtracted.

The sensitization of the electrode with PBI^{2+} was obtained by dip coating of the FTO| *nano*WO_3 sample into a 1 mM solution of $PBI(PF_6)_2$ in acetonitrile at 50°C for 6 hours, which allows surface saturation with the dye (ΔOD at 475 nm *ca.* 0.25-0.30).

Even if this PBI^{2+} lacks of specific anchoring groups, it was shown to spontaneously bind to porous WO_3, as demonstrated by the blue shift and by the modification of the vibrational structure of the absorption spectrum on the surface, which is related with the formation of H-aggregates (stacked aggregates, different from J-aggregates; Fig. 4.2).[181]

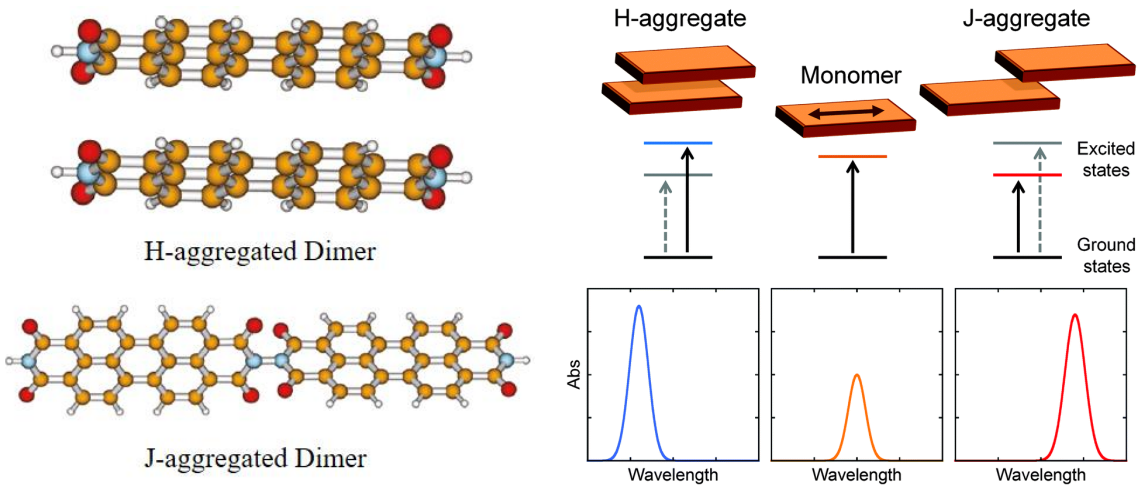

Fig. 4.2 a) H-aggregated and J-aggregated dimers;[181] **b)** spectral modifications of a dye monomer due to the formation of H- and J-aggregates: for H-aggregates a hypsochromic shift of the spectrum is observed, while for J-aggregates a bathochromic shift is observed.

Indeed, the as-prepared electrodes show a main absorption band in the 450-500 nm region and a shoulder at 551 nm (Fig. 4.3a, black line), blue-shifted with respect to solution spectra of PBI^{2+} (Fig. 4.3d, black line), and compatible with the formation of stacked aggregates on the semiconductor porous surface.

Several procedures for Ru$_4$POM catalyst deposition onto *nano*WO$_3$| PBI^{2+} electrodes were then tested:

- soaking of the *nano*WO$_3$| PBI^{2+} sensitized samples in acidic aqueous solution (0.1 M NaClO$_4$ pH 3) of Ru$_4$POM at different concentrations (1 mM and 9 mM);
- soaking in aqueous solution with 5:1 PBI^{2+}/Ru$_4$POM preformed aggregates;
- soaking of PBI^{2+}/Ru$_4$POM aggregates formed in acetonitrile solution.

As observed by UV-Vis spectra (Fig. 4.3a, red line and Fig. 4.3b, orange line), Ru$_4$POM deposition slightly modifies the absorption spectrum, with a red-shift of the absorptions and a new shoulder at 505 nm, probably due to modification in the surface aggregates in the presence of Ru$_4$POM, as observed in aqueous solution (see Chapter 3).

In the case of Ru$_4$POM deposition starting from 5:1 PBI^{2+}/Ru$_4$POM aggregates in water (Fig. 4.3c), the spectrum of the electrode after deposition is significantly different from the PBI^{2+} sensitized electrode and it shows a similar shape of the aggregate in aqueous solution (Fig. 4.3d). Finally, the electrode prepared from the PBI^{2+}/Ru$_4$POM aggregate formed in acetonitrile does not show the same significant changes after deposition (Fig. 4.3e). Indeed,

the only difference is the small increase of the intensity ratio between the peaks at 460 and 490 nm and an almost negligible increase of absorption, similarly to the spectrum of the aggregate in acetonitrile solution (Fig. 4.3f).

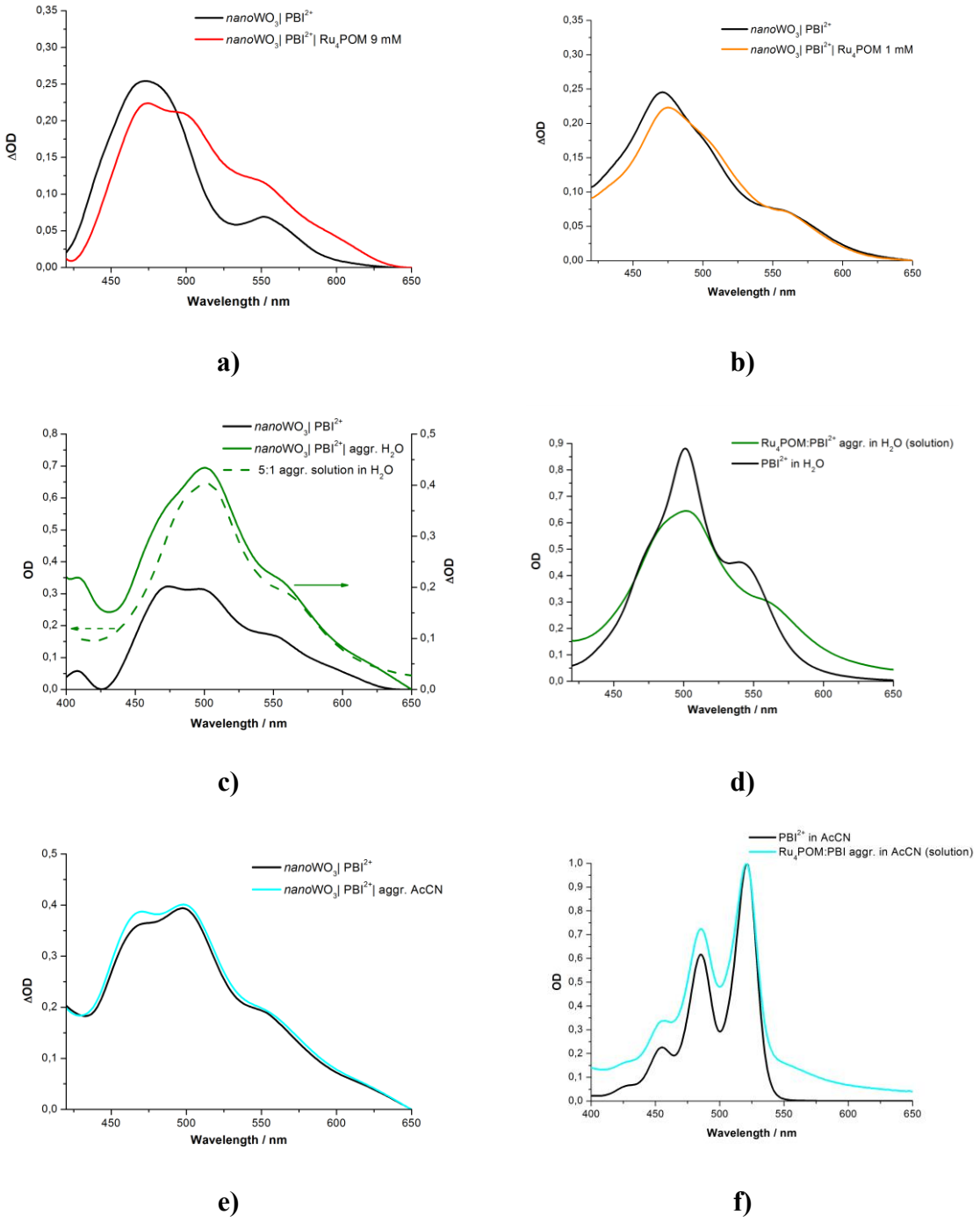

Fig. 4.3 Scattering corrected absorption spectra for *nano*WO_3| PBI^{2+} samples before (solid black lines) and after (solid colored lines) Ru_4POM catalyst deposition by soaking in **a)** 9 mM solution of Ru_4POM in 0.1 M $NaClO_4$ pH 3 (red line); **b)** 1 mM solution of Ru_4POM in 0.1 M $NaClO_4$ pH 3 (orange line); **c)** in 25 μM Ru_4POM:PBI aggregate solution in water (green olive solid line), compared to absorption spectrum of

aggregate solution (olive green dashed line); **d)** UV-Vis absorption spectra of PBI^{2+} 25 μM solution in water (black line) and of 25 μM Ru_4POM:PBI 1:5 aggregate in water (green olive line); **e)** soaking in 25 μM Ru_4POM:PBI aggregate solution in acetonitrile (cyan line); **f)** comparison between normalized UV-Vis absorption spectra of PBI^{2+} solution in acetonitrile (black line) and Ru_4POM:PBI aggregate solution in acetonitrile (cyan line).

4.2.2 Photoanodes performance in Cyclic Voltammetries

Electrochemical and photoelectrochemical experiments were performed in a three-electrode configuration with the *nano*WO_3| PBI^{2+} and the *nano*WO_3| PBI^{2+}| Ru_4POM as working electrodes, a platinum wire as counter electrode and an Ag/AgCl (3 M NaCl) as reference electrode in 0.1 M $NaClO_4$ pH 3 as electrolyte; potentials were then referred to the Normal Hydrogen Electrode (NHE), by using the conversion E(vs NHE) = E(vs Ag/AgCl) + 0.197 V. Photocurrent measurements were performed under irradiation with a solar simulator with AM 1.5 G light with a 450 nm long-pass filter. This latter was used in order to avoid direct excitation of WO_3 semiconductor, which may result in hole formation at the valence band of WO_3 and consequent production of hydroxyl radical species that may lead to dye degradation.

The samples were tested in cyclic voltammetry (CV) experiments between the open circuit potential (OCP) and 0.75 V or 1.20 V vs NHE at scan rate 20 mV/s, under dark and light conditions in order to identify the onset potential of the photoinduced catalytic process.

From Fig. 4.4, it is possible to observe that an initial anodic current spike (10-30 μA/cm^2, observed at E = 0.3-0.4 V vs NHE) is observed in all samples both in dark and light conditions, due to the rapid loss of electronic population from the superficial electronic states of the WO_3. In all dark CVs the observed current are negligible and lower than 10 μA/cm^2. For the *nano*WO_3 sample, a negligible difference in currents between dark and light is observed, confirming that the WO_3 semiconductor is not photoactive under these conditions, upon irradiation with the 450 nm long-pass filter (blue lines in Fig. 4.4a). Conversely, an increase in the current is observed upon irradiating the *nano*WO_3| PBI^{2+} samples, reaching 22 μA/cm^2 at 0.75 V vs NHE. This anodic photocurrent is therefore ascribable to the presence of the PBI^{2+} dye; nevertheless, its origin is uncertain: Finke and co-workers proposed that the photocurrent observed for ITO| PBI samples (where the PBI dye is covalently anchored to the ITO surface by exploiting phosphonate groups) was probably due to the oxidation of trace impurities or to some oxidative degradation of the dye.[114]

From Fig. 4.4b, the catalyst-functionalized electrodes show photocurrent densities of 40-45 μA/cm^2 at 0.75 V vs NHE, twice the photocurrent value for the *nano*WO_3| PBI^{2+} electrode, with the only exception of the *nano*WO_3| PBI^{2+}| Ru_4POM 1 mM sample which shows photocurrents similar to the catalyst free electrode (orange and black traces in Fig. 4.4b).

The onset potential of the catalytic waves for the photoelectrodes with Ru_4POM (prepared from PBI^{2+}/Ru_4POM aggregates in water and in acetonitrile, or by dipping in Ru_4POM 9 mM aqueous solution) is *ca*. 0.39 V vs NHE (green, cyan and red traces in Fig. 4.4b).

It was then decided to investigate deeply the properties of the electrodes prepared by dipping in Ru_4POM 9 mM aqueous solution, that provides the easiest way to functionalize the sensitized electrodes with Ru_4POM catalyst.

For this electrode, the catalytic activity due to the presence of Ru_4POM is confirmed, since the photocurrent density increases upon increasing the potential until 1.20 V vs NHE, reaching 80 μA/cm^2 (Fig. 4.4c). Moreover, the presence of cathodic peaks observed in the reverse scan at 0.45-0.54 and 0.97 V vs NHE, which are not visible in the *nano*WO_3| PBI^{2+} sample, could be related to Ru_4POM reduction (Fig. 4.4c).

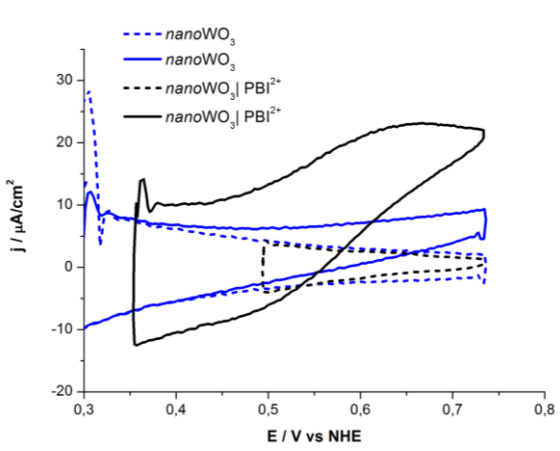

a)

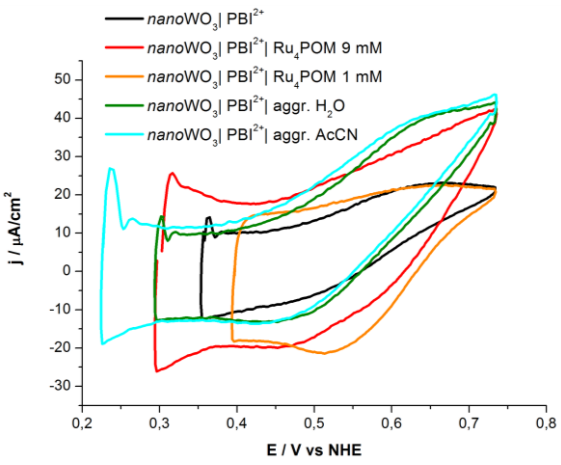

b)

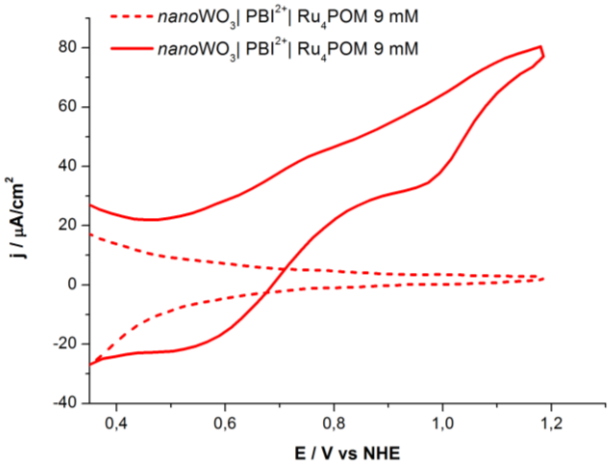

c)

Fig. 4.4 Cyclic voltammetries under light (solid lines) and dark conditions (dashed lines), in 0.1 M $NaClO_4$ pH 3, RE = Ag/AgCl (3 M NaCl), CE = Pt wire, 20 mV/s, light: AM 1.5 + 450 nm long-pass filter. **a)** CV for bare *nano*WO_3 and for *nano*WO_3| PBI^{2+}. **b)** Comparison of CV under light for sensitized samples soaked in Ru_4POM 9 mM (red line) solution, 1 mM (orange line) solution, Ru_4POM/PBI^{2+} 1:5 aggregate aqueous solution (olive green line), Ru_4POM/PBI^{2+} aggregate in acetonitrile solution (cyan line). **c)** CV for *nano*WO_3| PBI^{2+}| Ru_4POM 9 mM under dark and light conditions until 1.20 V vs NHE.

4.2.3 *nano*WO_3| PBI^{2+}| Ru_4POM 9 mM photoanodes performance in Constant Potential Electrolysis

Constant Potential Electrolysis experiments were performed at 0.75 V and 1.20 V vs NHE, in order to evaluate the performance and the stability of the photoelectrodes under prolonged operating conditions. Importantly, already under non-operating conditions a visible bleaching of the sample after 40 minutes in 0.1 M $NaClO_4$ pH 3 is observed, due to PBI^{2+} detachment from the electrode surface by interaction with perchlorate anions, used as supporting electrolyte. $NaNO_3$, tested as an alternative supporting electrolyte, provided similar results.

A first CPE experiment with two photoelectrodes *nano*WO_3| PBI^{2+} and *nano*WO_3| PBI^{2+}| Ru_4POM 9 mM, was performed at 0.75 V vs NHE (Fig. 4.5a). The catalyst-functionalized photoelectrode shows an initial photocurrent of 44 µA/cm^2, according to what observed in light CVs, which decays in the first 5 minutes and stabilizes at about 7 µA/cm^2. For the blank *nano*WO_3| PBI^{2+} sample, a similar behavior is observed with the initial and the final photocurrents being respectively 22 µA/cm^2 and 3 µA/cm^2.

A second CPE experiment with two new photoelectrodes was performed at a higher potential of 1.20 V vs NHE, in order to evaluate the effect of higher potentials in terms of photoelectrode degradation (Fig. 4.5b). For the *nano*WO_3| PBI^{2+} sample, a first rapid decay in the photocurrent is observed with a subsequent strong increase from 40 to 50 $\mu A/cm^2$ occurred in the first 10 minutes; the peak current then rapidly decays and apparently stabilizes below 40 $\mu A/cm^2$. The *nano*WO_3| PBI^{2+}| Ru_4POM 9 mM electrode shows similar features, although the peak current is lower, with the same stabilization at about 40 $\mu A/cm^2$. The two observed peaks are thus ascribable to rapid degradation of the PBI^{2+} photosensitizer, probably due to oxidant or radical species generated from the semiconductor or to simple oxidative degradation of the PBI^{2+} dye caused by the high applied potential.

In these experiments, oxygen detection was not possible neither with oxygen-sensitive fluorescence probes, due to interference from incident light, nor by gas chromatography, since the photocurrent densities are too low to produce a significant and detectable amount of oxygen, even assuming a quantitative faradaic yield for oxygen.

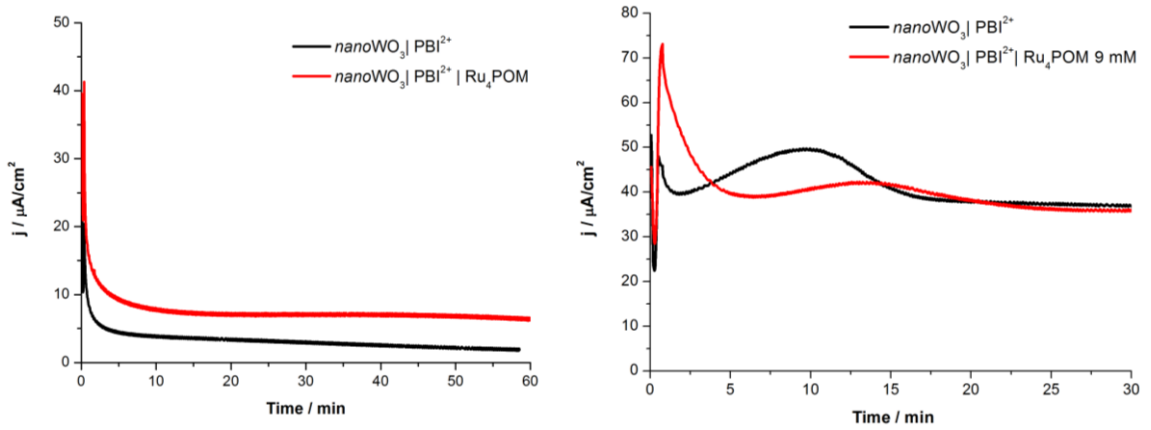

a) **b)**

Fig. 4.5 Constant Potential Electrolysis for photoelectrodes *nano*WO_3| PBI^{2+} and *nano*WO_3| PBI^{2+}| Ru_4POM 9 mM under irradiation in 0.1 M $NaClO_4$ pH 3, RE = Ag/AgCl (3 M NaCl), CE = Pt wire, light: AM 1.5 + 450 nm long-pass filter at **a)** 0.75 V vs NHE and **b)** 1.20 V vs NHE.

4.2.4 Catalyst quantification, turnover frequency and turnover number

The catalyst loading onto the electrode is a fundamental parameter to take into account for the evaluation of electrode performance.

The amount of Ru_4POM catalyst onto the *nano*WO_3| PBI^{2+}| Ru_4POM 9 mM electrodes was determined by inductively coupled plasma optical emission spectrometry (ICP-OES), an analytical technique used for the detection of trace metals. The loading of Ru_4POM was found to be 4.34 ± 0.23 nmol/cm^2. For a *nano*WO_3| PBI^{2+} electrode, the PBI^{2+} loading was instead determined by UV-Vis spectroscopy, after dissolution of the PBI^{2+} film in DMF: the amount was 16.5 nmol/cm^2 (this value may be slightly underestimated, since the PBI^{2+} was not fully detached from the electrode surface). Importantly, the calculated PBI^{2+}/Ru_4POM ratio is 3.8:1, close to the stoichiometric ratio of 4:1 already observed for the aggregate in acidic solution at pH 2.5 (in this case the electrodes are prepared at pH 3).

Once the catalyst loading has been determined and assuming a quantitative faradaic yield for oxygen production in the observed photocurrents, the turnover frequency (TOF) and the turnover number (TON) can be determined on the basis of the maximum photocurrent density in a short time interval (determining the TOF) and of the total charge passed before electrode degradation (determining TON), according to the following equations (Eqs. 4.1-4.2):

$$TOF = \frac{J_{MAX}}{4F \cdot l_{WOC}} \tag{4.1}$$

$$TON = \frac{Q_{MAX}}{4F \cdot l_{WOC}} \tag{4.2}$$

where J_{MAX} is the photocurrent density, Q is the charge, F is the Faraday constant and l_{WOC} is the catalyst loading.

TOF and TON values were calculated for the *nano*WO_3| PBI^{2+}| Ru_4POM 9 mM photoelectrodes, from the previously reported CPE experiments performed at 0.75 V and 1.20 V vs NHE (Fig. 4.5). The maximum photocurrent density values were chosen at 10 seconds because after this time the contribution of transient capacitive currents have already decayed to zero, while the surface electronic states of the semiconductor have been emptied and the semiconductor has been again oxidized, thus avoiding to consider contributions related to semiconductor oxidation. The charge values were obtained from the total charge passed after 10 minutes of CPE at 0.75 V vs NHE and 5 minutes of CPE at 1.20 V vs NHE, corresponding to the time at which begins the leaching of the dye from the electrodes.

The obtained results are summarized in Table 4.1: the TOF results of 0.026 s^{-1} at 0.75 V vs NHE and it almost doubles at 1.20 V vs NHE, being 0.048 s^{-1}. These TOF values are generally higher than that reported for other photoanodic systems containing Ru_4POM as

catalyst (0.004-0.02 s^{-1}, see Table 4.2).[108] The calculated TON are 3.8 at low potential (E = 0.75 V vs NHE) to 8.5 at high potential (E = 1.20 vs NHE); these values are slightly lower with respect to the TON of 14 exhibited by the Ru_4POM photoelectrode reported in literature (with a Ru(II) polypyridine-based photosensitizer), but this value is limited from the instability of the photoanodic system under operating conditions.[108]

Table 4.1 Turnover number and frequency estimates calculated with Eqs. 4.1 and 4.2 from Constant Potential Electrolysis performed at 0.75 V and 1.20 V vs NHE, reported in Fig. 4.5: maximum photocurrent density values correspond to photocurrent density values after 10 s of CPE; TON was calculated from the charge value passed after 10 minutes and 5 minutes respectively for CPE at 0.75 V and 1.20 V vs NHE.

Working electrode	E_{CPE} vs NHE [V]	J_{MAX} [$\mu A/cm^2$]	TOF [s^{-1}]	TON
nanoWO_3| PBI^{2+}| Ru_4POM	0.75	44	0.026	3.8
nanoWO_3| PBI^{2+}		22	-	-
nanoWO_3| PBI^{2+}| Ru_4POM	1.20	75	0.048	8.5
nanoWO_3| PBI^{2+}		49	-	-

4.2.5 Incident and Absorbed Photon-to-Current Efficiency

Incident Photon-to-Current Efficiencies (IPCE) and Absorbed Photon-to-Current Efficiencies (APCE) are parameters related to the percentage of incident and absorbed photons that are converted to electric current, respectively (see also section 1.5.4).

These parameters were determined for *nano*WO_3\| PBI^{2+} and for *nano*WO_3\| PBI^{2+}\| Ru_4POM (9 mM and 1 mM) photoelectrodes, in collaboration with Dr. Serena Berardi, Prof. Caramori and Prof. Bignozzi (University of Ferrara). For each sample a dark/light chronoamperometry was carried out at 0.75 V vs NHE in 0.1 M $NaClO_4$ pH 3 (Fig. 4.6a), with monochromatic irradiation with wavelength between 410 and 580 nm, generated by a 175 W Xenon lamp coupled to an Applied Photophysics monochromator. The chronoamperometries were performed starting from 410 nm and moving forward with 10 nm steps, separating each 100 seconds long step of monochromatic irradiation with a dark interval. The irradiance, i.e. the irradiated power per area unit, of the monochromatic light source was calculated at each wavelength with an appropriately calibrated silicon photodiode.

The IPCE value was calculated according to Eq. 4.3:

$$IPCE_\lambda = \frac{\Phi_{e^-}}{\Phi_{ph}} \cdot 100 = \frac{J_\lambda \cdot 10^{-2} / F}{J_\lambda / N_A \cdot E_\lambda} \cdot 100 \approx 1240 \cdot \frac{J_\lambda}{\lambda \cdot I_\lambda} \quad (4.3)$$

where Φ_{e^-} and Φ_{ph} are the flux of electrons and incident photons (mol/s m^2), respectively, J_λ is the steady state photocurrent density (μA/cm^2) at a certain value of λ, F is the Faraday constant, I_λ is the irradiance defined as the irradiated power at λ per unit area, N_A is Avogadro's number and E_λ = hc/λ × 10^{-9} is the energy (eV) of a photon of wavelength λ (nm).

The APCE value was then calculated from the IPCE and the UV-Vis absorption spectra of the samples, used to calculate the light harvesting efficiency (LHE) at each wavelength, according to Eq. 4.4:

$$APCE_\lambda = \frac{IPCE_\lambda}{LHE_\lambda} = \frac{IPCE_\lambda}{1 - T(\lambda)} = \frac{IPCE_\lambda}{1 - 10^{-A(\lambda)}} \quad (4.4)$$

where $T(\lambda)$ is the transmittance and $A(\lambda)$ is the absorbance at λ.

In Fig. 4.6b, the IPCE trends are reported for the three samples: the orange trace related to the *nano*WO$_3$| PBI^{2+}| Ru$_4$POM 1 mM shows a similar trend of the catalyst-free electrode, consistently with the cyclic voltammetries results described above. Since the photocurrent densities should be higher for wavelength at which the sample absorbs, IPCE trends should resemble the UV-Vis absorption spectrum of the samples, meaning that it should be higher where absorption of the sensitizer occurs. However, while for blank *nano*WO$_3$| PBI^{2+} and for *nano*WO$_3$| PBI^{2+}| Ru$_4$POM 1 mM samples the IPCE values are 0.1-0.2% above 510 nm, where PBI^{2+} does not absorb, the IPCE for *nano*WO$_3$| PBI^{2+}| Ru$_4$POM 9 mM is 0.4%: this could be explained by the extended absorption due to the presence of PBI^{2+}/Ru$_4$POM aggregates on the electrode surface. Indeed, IPCE results and absorption spectra for the samples exhibit similar trends between 460 and 500 nm, while then the IPCE values decay above 500 nm for the PBI-sensitized sample (Fig. 4.6c). In the case of *nano*WO$_3$| PBI^{2+}| Ru$_4$POM 9 mM, the absorbance above 520 nm is higher than for the blank sample, which is consistent with higher IPCE values.

The APCE values were obtained from the normalization of the IPCE trend with the UV-Vis absorption spectra of the samples (Fig. 4.6d).

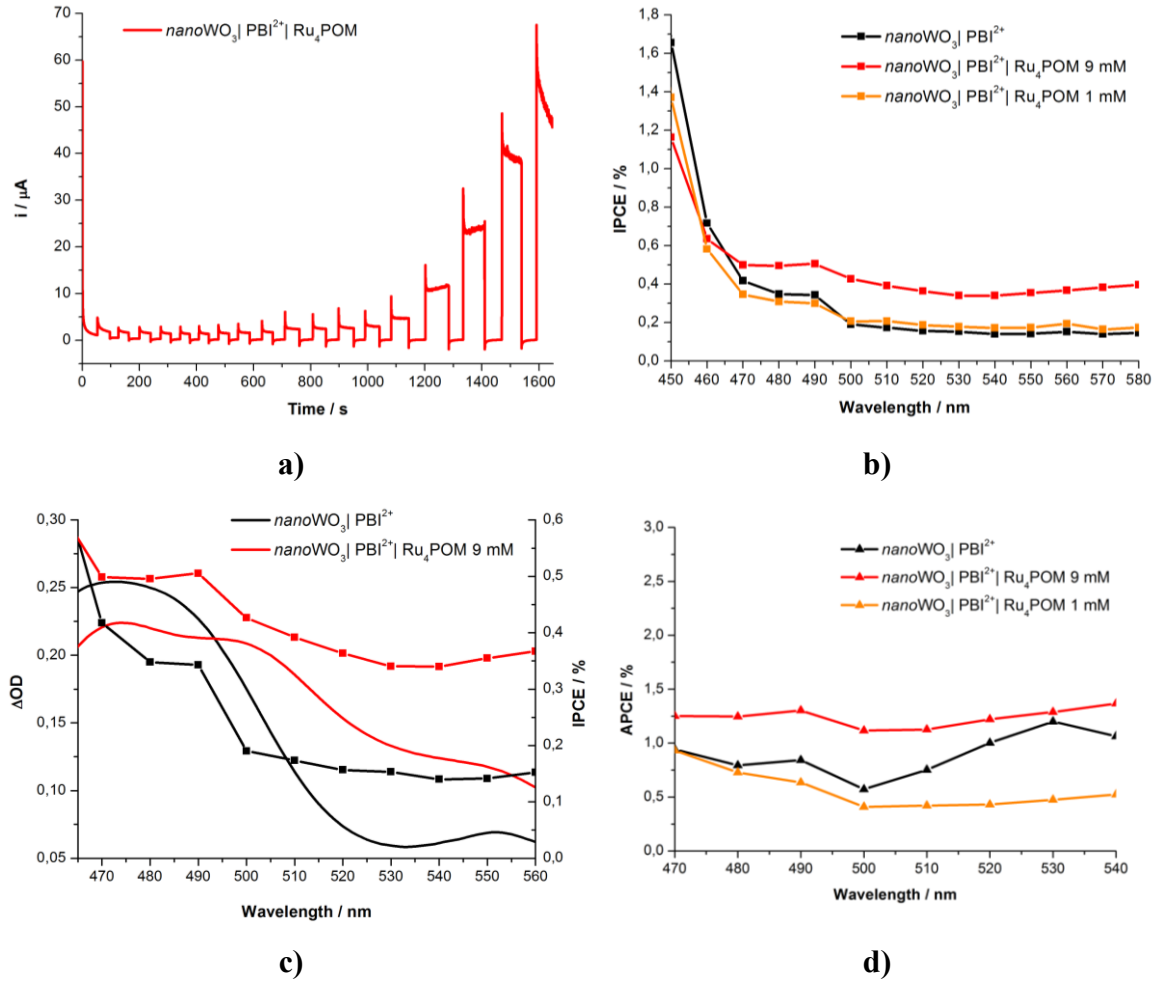

Fig. 4.6 a) Dark-light chronoamperometry for *nano*WO_3| PBI^{2+}| Ru_4POM 9 mM performed at 0.75 V vs NHE in 0.1 M NaClO4 pH 3, RE = Ag/AgCl (3 M NaCl), CE = Pt wire, with monochromatic irradiation generated by a 175 W Xenon lamp coupled to an Applied Photophysics monochromator: wavelengths between 410 nm and 580 nm with 10 nm steps. **b)** IPCE for blank *nano*WO_3| PBI^{2+} and for *nano*WO_3| PBI^{2+}| Ru_4POM samples (soaked in Ru_4POM 9 mM and 1 mM) determined from dark-light chronoamperometries. **c)** Comparison between UV-Vis absorption spectra (solid lines) and IPCE (solid dotted lines) for *nano*WO_3| PBI^{2+} (black lines) and *nano*WO_3| PBI^{2+}| Ru_4POM 9 mM (red lines). **d)** APCE for *nano*WO_3| PBI^{2+} and for *nano*WO_3| PBI^{2+}| Ru_4POM samples (soaked in Ru_4POM 9 mM and 1 mM).

Since the photosensitizer absorption maximizes in the 470-500 nm region, the significant IPCE and APCE values are those calculated in this range, being respectively 0.50% and 1.30% for the *nano*WO_3| PBI^{2+}| Ru_4POM 9 mM sample and 0.34% and 0.64% for the blank *nano*WO_3| PBI^{2+} sample. These values observed with the Ru_4POM catalyst are comparable than those previously reported by Bignozzi and co-workers with the same *nano*WO_3| PBI^{2+} photoelectrodes with IrO_2 catalyst (IPCE 0.6% and APCE 0.8%).[115]

4.3 Conclusions and Perspectives

A dye-sensitized photoanodic system has been developed, starting from a semiconducting film of nanocrystalline porous WO_3, deposited by six successive spin coating steps onto FTO-coated glass slides, leading to a film thickness of *ca.* 1.5 μm. The electrode was then sensitized with the bis-cationic perylene bisimide, PBI^{2+}, which spontaneously adsorbs on metal oxide surfaces and is able to inject electrons into the conduction band of WO_3 with higher rates ($k_{inj} > 10^8$ s^{-1}) with respect to SnO_2 and TiO_2.[115] Moreover, this PBI^{2+} was also chosen because it is metal-free and its highly oxidizing excited state (2.20 V vs NHE) and its high oxidative stability in water makes it compatible with almost all WOCs. Finally, thanks to the cationic charge, it can electrostatically interact with the Ru_4POM, used as WOC both at neutral and acidic pH, leading to the formation of supramolecular architecture with a definite PBI^{2+}/Ru_4POM ratio (5:1 at pH 7 and 4:1 at pH 2.5).

For this reason, Ru_4POM has been deposited by soaking onto the *nano*WO_3| PBI^{2+} photoelectrodes in three different forms: pristine Ru_4POM, preformed PBI^{2+}/Ru_4POM aggregates in water and PBI^{2+}/Ru_4POM aggregates in acetonitrile.

From CV experiments performed in acidic solution (0.1 M $NaClO_4$ pH 3) upon irradiation with visible light (AM 1.5 G light with 450 nm long-pass filter to avoid WO_3 excitation), the photocurrent density related to Ru_4POM catalyst-functionalized photoelectrodes shows a two-fold enhancement with respect to the *nano*WO_3| PBI^{2+} photoelectrodes at 0.75 V vs NHE (40-45 μA/cm^2 vs 22 μA/cm^2). The photoelectrodes with the catalyst showed an onset potential at 0.40 V vs NHE.

During CPE experiments at 0.75 V vs NHE, the photocurrent density for the *nano*WO_3| PBI^{2+}| Ru_4POM electrodes decayed from 44 μA/cm^2 to 7 μA/cm^2 in 60 minutes, with the initial value being halved after the first 2 minutes. Also in the case of the blank *nano*WO_3| PBI^{2+} electrodes, the initial photocurrent density of 22 μA/cm^2 is halved in the first 2 minutes and decayed to 3 μA/cm^2 in 60 minutes. Importantly, visible bleaching of the electrodes was observed after 10 minutes of electrolysis, due to the leaching of the dye by interaction with the perchlorate anions used as electrolyte. The low observed photocurrents made impossible the oxygen detection neither with gas chromatography nor with oxygen-sensitive fluorescence probes, for interference issues from incident light.

The catalyst loading was determined by ICP-OES experiments and was found to be 4.34 ± 0.23 nmol/cm^2 of Ru_4POM. The dye loading was also determined by UV-Vis spectroscopy

and was found to be 16.5 nmol/cm^2. Interestingly, the PBI^{2+}/Ru_4POM ratio results of 3.8:1, as expected for the aggregate formation in solution at acidic pH (4:1 at pH 2.5).

According to Eqs. 4.1-4.2 and knowing the catalyst loading, TOF and TON values were calculated from the initial photocurrent and from the total charge passed after 10 minutes, respectively, of CPE at 0.75 V and 1.20 V vs NHE. TOF and TON values resulted to be respectively 0.026-0.048 s^{-1} and 3.8-8.5.

Finally, the IPCE values were calculated according to Eq. 4.3 from the steady state photocurrents recorded in chronoamperometric experiments performed under monochromatic irradiation in the 410-580 nm range with 10 nm steps. APCE values were then calculated according to Eq. 4.4 from IPCE results and UV-Vis absorption spectra of the samples. The maximum IPCE value of 0.50% and of 0.34% for *nano*WO_3| PBI^{2+}| Ru_4POM 9 mM and for *nano*WO_3| PBI^{2+} samples, respectively, were obtained at 490 nm, consistently with the maximum absorption of the photosensitizer, while the resulting APCE values were 1.30% and 0.64%, respectively.

In conclusion, in the view of building a photoelectrochemical device, the obtained results are promising since the coupling of PBI^{2+} and Ru_4POM, demonstrating oxygenic activity in solution, also produced an oxygen evolving system when deposited onto an inexpensive nanocrystalline semiconductor film such as WO_3.

In Table 4.2 the performance of the *nano*WO_3| PBI^{2+}| Ru_4POM 9 mM photoanodes are reported in comparison with the state-of-the-art photoelectrodes for oxygen evolution.

Table 4.2 Overview on state-of-the-art photoanodes and their performances.

#	Photoanode	E vs NHE [V]	J_{max} [$\mu A/cm^2$]	TOF [s^{-1}]	Stability $t_{1/2}$ [min]	IPCE [%]	APCE [%]	Ref.
1	*nano*WO_3| PBI^{2+}| Ru_4POM 9 mM	0.75	44	0.026	2	0.50	1.30	This study
2	*nano*TiO_2| $[Ru(bpy)_2(dpbpy)]^{2+}$| Ru_4POM[a]	0.20	14.2	0.004	<2	-	0.11	[108]
3	*nano*TiO_2| [Ru(Na-5-crown-phen)$_2$ (dpbpy)]$^{4+}$| Ru_4POM[a]	0.20	54.8	0.02	2	-	0.39	[108]
4	*nano*TiO_2| $[Ru(bpy)_2(dpbpy)]^{2+}$| Ru(II)(bda)(4-picoline)[b]	0.20	1700	1.0	<2	14	-	[109]
5	ITO| PBI| CoO_x[c]	1.20	150	-	-	0.12	1	[114]
6	*nano*WO_3| PBI| IrO_2[d]	0.75	70	-	-	0.6	0.8	[115]
7	*meso*ITO| PS II[e]	0.55	0.3	0.03	4	0.125	0.70	[116]
8	IO-*meso*ITO| PS II[f]	0.50	930	12.9	*ca* 5	17.0	-	[117]
9	IO-ITO| polymer-PS II[g]	0.50	410	6.7	4	7.7	-	[118]

[a]Dye sensitized TiO_2 with Ru_4POM deposited on it; general conditions: pH 5.8 in 80 mM $Na_2SiF_6/NaHCO_3$ buffer electrolyte containing $NaClO_4$ (200 mM), irradiation 455 nm (33 mW cm^{-2}). [b]Coadsorbed Ru(bpy)- and Ru(II)(bda)-derivatives on nanostructured TiO_2; general conditions: pH 6.8 in phosphate buffer, irradiation with a white light source coupled to a 400 nm long-pass filter (300 mW cm^{-2}). [c]Dye sensitized ITO with photoelectrodeposited CoO_x nanoparticles; general conditions: pH 7 in 0.1 M phosphate buffer, irradiation with a xenon arc lamp (100 mW cm^{-2}). [d]Dye sensitized WO_3 with spin coated IrO_2 nanoparticles; general conditions: pH 3 $HClO_4$, 0.1 M $NaClO_4$, illumination under AM 1.5 G with a cut-off filter at 435 nm (100 mW cm^{-2}). [e]Mesoporous ITO loaded with photosystem II; general conditions: pH 6.5 in 40 mM 2-(N-morpholino)ethanesulfonic acid (MES) electrolyte, irradiation at 680 nm. [f]Inverse opal mesoporous ITO with embedded photosystem II; general conditions: pH 6.5 in 40 mM 2-(N-morpholino)ethanesulfonic acid (MES), $MgCl_2$ (15 mM), $CaCl_2$ (15 mM), glycerol (10%), and betaine (1 M), irradiation at 679 nm. [g]Inverse opal mesoporous ITO where photosystem II is embedded with the aid of redox active polymers; general conditions: pH 6.5 in 40 mM MES electrolyte containing $CaCl_2$ (20 mM), $MgCl_2$ (15 mM) KCl (50 mM).

As observed from entries 1-3 in Tab. 4.2, the PBI^{2+}-sensitized photoelectrodes resulted in higher APCE values if compared with Ru(II) polypyridine-based photosensitizer (1.30 % vs 0.11-0.39%).[108] Indeed, even if the observed photocurrents are comparable between electrodes, the absorption due to $Ru(bpy)_3^{2+}$ is less effective than in the case of PBI^{2+}.

Moreover, while Ru(II) polypyridine-based photosensitizer are used at nearly neutral pH (6 - 9) since the dye is susceptible to self-degradation, PBI^{2+} can be used as photosensitizer both at neutral and acidic pH (see Chapter 3), making it suitable for application in a wide range of pH. The performance of these photoelectrodes in terms of TOF (the same Ru_4POM catalyst is used), shows also a better results with the PBI^{2+} as dye, where 0.026 s^{-1} is reached (vs 0.004-0.02 s^{-1}), confirming a strong interaction in the case of the PBI^{2+}/Ru_4POM system between the PS-WOC moieties.

Since now, the best state-of-the-art photoelectrode, reported by Sun and co-workers, consists of a Ru(II) polypyridine-based dye and a ruthenium molecular catalyst (entry 4).[109] This photoelectrode reaches 1700 $\mu A/cm^2$ at 0.20 V vs NHE (phosphate buffer pH 6.8), due to the coadsorption of the PS and the WOC on the nanostructured TiO_2.

The comparison between PBI-based photoelectrodes with molecular catalyst (entry 1) and metal oxides catalysts (entries 5-6)[114,115] shows higher photocurrents in the case of metal oxides-based electrodes. However, in the case of ITO| PBI| CoO_x electrode (entry 5), the applied potential is 1.20 V vs NHE, instead of 0.75 V. Interestingly, nanostructured architectures with the PBI^{2+} and the Ru_4POM molecular catalyst can be obtained, exploiting the self-assembling nature of the PBI^{2+}/Ru_4POM system with a definite stoichiometry, which has a positive impact on the performance of the photoelectrodes. Indeed, this system shows a high APCE value compared with the other electrodes (1.30% vs 1-0.8%).

All the reported photoelectrodes (entries 1-6) show comparable stabilities reaching 2 minutes. In most cases, this is due to the photosensitizer leaching from the electrode surface because of the applied bias. Therefore, a fundamental improvement will be the anchoring of the dye on the porous surface of the semiconductor, possibly by covalent linking with phosphonate groups, as reported by Finke and co-workers.[114]

Finally, another important improvement will look at the use of metal oxide blocking layers between PBI^{2+} and WO_3 in order to limit recombination processes,[182,183] which might be one of the main reason for the low observed photocurrents.

Finally, taking inspiration by Reisner and co-workers, the engineering of electrodes with a semiconducting mesoporous/macroporous skeleton can be considered to further increase the effective surface area, consequently obtaining higher catalyst loading and higher photocurrents.[116–118]

5 Conclusions and perspectives

This Thesis project has been focused on the development of innovative synthetic systems for artificial photosynthesis, aimed at the production of renewable fuels with sunlight, by the water splitting into hydrogen and oxygen.

This work has mainly focused on the water oxidation reaction, since it is recognized as the bottleneck in the development of an efficient device for water splitting. Considerable results have been achieved in the last years, concerning stability and efficiency of water oxidation catalysts (WOCs).[33]

In particular, the research is currently dedicated at the optimization of the molecular components, including light-antennae, photosensitizers and multi-redox catalysts, within nanostructured environments that influence the geometry and the properties of the photosynthetic ensemble. Moreover, the integration of such systems on electroactive semiconductor surfaces and their interface with light is one of the key challenge for the development of regenerative photoanodes.

In this work, these open issues were considered.

In **Chapter 2**, a covalent dyad based on a Co(II) catalyst and a Ru(II) photosensitizer moiety has been presented. The covalent approach could guarantee a stringent molecular control on the PS-WOC distances and geometries as governing factors for photoinduced electron transfers to prevent side reactions leading to photosensitizer self-oxidation and degradation, or to prevent unproductive charge recombination.

The photophysical characterization in aqueous environment has been proved, showing an oxidative quenching of the photosensitizer moiety by the Co(II) in 15 ps: this confirms the electronic interaction between the two metal centers. In principle, this fast quenching of the photosensitizer excited state might be detrimental for the use of this dyad in homogeneous systems. However, such dyad displaying an intramolecular quenching could still be considered for the application in regenerative systems where the PS-WOC dyad is supported onto the surface of a semiconductor.

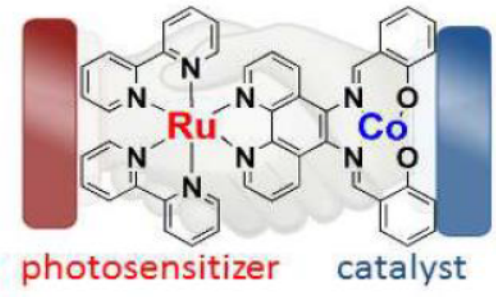

In **Chapter 3**, a novel supramolecular self-assembling system combining an organic metal-free bis-cationic perylene bisimide (PBI) photosensitizer with a totally inorganic anionic polyoxometalate (Ru_4POM) has been presented.

Nowadays, the choice of metal-free photosensitizers is a key aspect, in the view of industrial applications. Moreover, this PBI self-assembles in water into 1-D structures, and it provides one of the strongest photo-generated oxidant with $E(PBI^{*2+/1+}) = 2.20$ V vs NHE.

As in Nature, which uses non-covalent motifs to drive the process of photosynthesis, the combination with the Ru_4POM catalyst is driven by supramolecular, electrostatic interactions. This system self-assembles in aqueous environment into a nano-porous two dimentional architecture with a definite PBI^{2+}/Ru_4POM 5:1 stoichiometry, capable of driving water oxidation upon illumination with visible light. This system undergoes deactivation due to the byproduct formation from the sacrificial electron acceptor, used during photocatalytic experiments. These results paves the way for a further investigation of the system, coupling it with a n-type semiconductor in order to avoid such competing phenomena that hamper the catalytic performance of the system in solution.

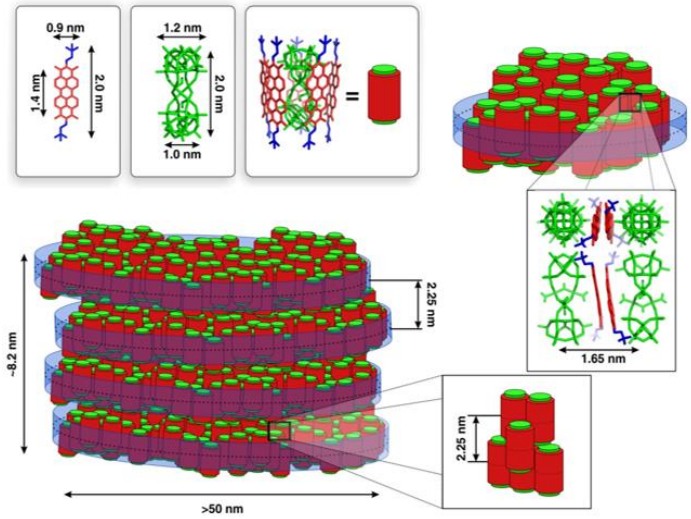

In **Chapter 4**, the photoanode supporting the PBI^{2+}/Ru_4POM assembly on a nanostructured WO_3 semiconductor has been presented. The obtained results, such as the photocurrent density of 44 $\mu A/cm^2$ at 0.75 V vs NHE, the TOF of 0.026s^{-1} and the IPCE and APCE values of 0.50% and 1.30%, respectively, are in line with the state-of-the-art performance of photoanodes and they are promising since the coupling of PBI^{2+} and Ru_4POM, demonstrating oxygenic activity in solution, also produced an oxygen evolving system when deposited onto an inexpensive nanocrystalline semiconductor film such as WO_3.

A fundamental improvement will be the anchoring of the dye on the porous surface of the semiconductor, possibly by covalent linking with phosphonate groups, as reported by Finke and co-workers,[114] and also the engineering of electrodes with a semiconducting mesoporous/macroporous skeleton can be considered to further increase the effective surface area, consequently obtaining higher catalyst loading and higher photocurrents.[116–118]

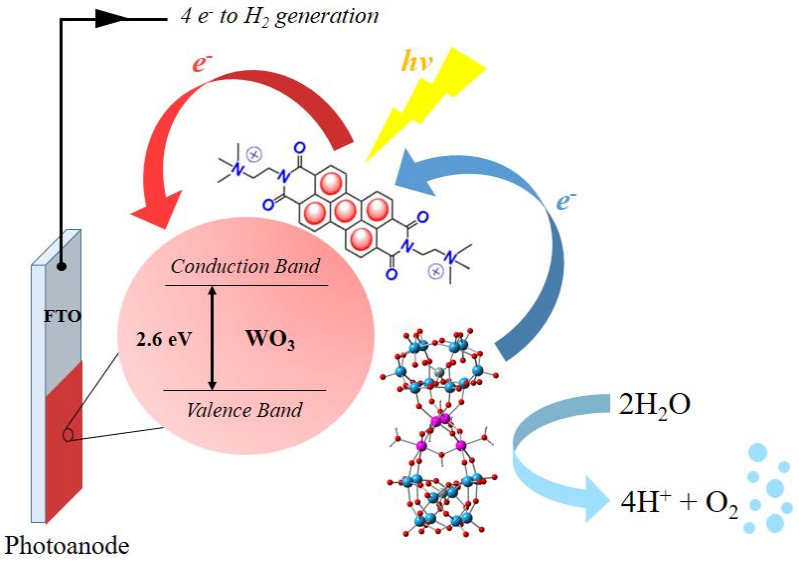

Finally, the aim of this Thesis is to give an overview on the importance of the geometry and morphology of the photosensitizer-catalyst assembly for the efficiency of the water oxidation process, both in homogeneous solution and supported on a solid semiconductor.

6 Experimental section

6.1 Materials

Chemicals and solvents for all synthetic and characterization procedures have been purchased from Sigma Aldrich, and used as received if not differently specified. All solvents used for photochemical characterization of single molecules and hybrid materials are of spectroscopic grade (99.5%). Deuterated solvents have been purchased from Sigma Aldrich and Cambridge Isotope Laboratories.

6.2 Instrumentation

^{1}H- and ^{13}C-NMR spectra were recorded with Bruker AV300 instruments operating at 300 MHz.

Electrospray Ionization-Mass Spectrometry (ESI-MS) measurements were performed with an Agilent Technologies MSD SL Trap mass spectrometer with ESI source coupled with a 1100 Series HPLC system.

UV-Vis absorption spectra were recorded at room temperature on a Perkin Elmer Lambda 45 and on a Varian Cary 50 Scan spectrophotometers.

Fluorescence spectra were recorded on a Perkin Elmer LS50B fluorimeter.

Fourier-Transform Infrared (FT-IR) spectra were recorded with a Nicolet 5700 FT-IR instrument equipped with Omnic 7.1 software.

ζ-Potential measurements were performed using a Malvern Zetasizer Nano ZS90 instrument, in poly-(methyl methacrylate) (PMMA) cuvettes containing 1 ml of the solution under investigation.

Cyclic Voltammetry (CV) studies and Constant Potential Electrolysis (CPE) experiments were carried out using a BAS EC-epsilon potentiostat and an AMEL Potentiostat-Galvanostat, model 7050, with a three-electrode cell under N_2 anhydrous atmosphere in deoxygenated phosphate buffer solution 0.2 M pH 7.0 and Britton-Robinson (BR) buffer pH 7.0, prepared according to literature procedures;[78] a glassy carbon (GC) electrode (3 mm diameter, geometric surface area of 7 mm^2) or Indium Tin Oxide (ITO) coated glass slides

(surface resistivity 8-12 Ω/sq) from Sigma Aldrich were used as working electrodes, a platinum wire as counter electrode and Ag/AgCl (3M NaCl) as reference electrode. For spectroelectrochemistry, a platinum minigrid has been used as working electrode, a platinum wire as counter electrode and Ag/AgCl (3M NaCl) as reference electrode, in a cuvette with 1 mm optical path. The potentials have been reported *versus* Normal Hydrogen Electrode, using the conversion E(vs NHE) = E(Ag/AgCl) + 0.197 V.

Photoelectrochemical experiments were performed using an AMEL Potentiostat-Galvanostat, model 7050, in combination with a LOT-Quantum Design solar simulator AM 1.5 G. A standard three-electrode electrochemical cell was used, with a platinum wire and an Ag/AgCl (3 M NaCl) as counter electrode and reference electrode, respectively.

Oxygen evolution measurements were monitored using a FOSPOR-R-AF probe, interfaced with a Neofox Real-Time software for data collection. The probe consists of a film of photosensitive material, excited by a 470 nm emitting LED source. The excitation and emission radiations are carried through an optic fiber to the detector. Oxygen quenches the emission of the photosensitive material in the film, linking the quenching with the concentration of oxygen in the probe.

6.3 Methods

Oxygen evolution kinetics were performed in aqueous solution (4.5 mL) containing PBI^{2+}, $Na_2S_2O_8$ and Ru_4POM, kept under stirring. The mixture was fluxed 20 minutes with nitrogen to remove the dissolved oxygen. The glass reactor (8.0 mL total volume), was purged with nitrogen and allowed to equilibrate in the dark at 25°C. Irradiation of the solution was conducted with one spotlight 10 cm far (4.5mW/cm^2). Oxygen evolution was monitored with a FOSPOR-R-AF probe, inserted in the reaction headspace and interfaced with a Neofox Real-Time software for data collection; dissolved oxygen was assumed to be negligible. The rate of oxygen production has been taken from the initial slope of the kinetic curves. Reactions have been run in triplicates; it has been confirmed that the concomitant presence of PBI^{2+}, $Na_2S_2O_8$, Ru_4POM and light was necessary to achieve oxygen production. The incident photons on the reactor have been obtained by measuring the power emitted from the LED white lamp by means of an Avantes AvaSpec-OPT-ULS3648 spectrometer.

Electrochemical measurements were performed purging nitrogen in the electrolyte solution for 15 minutes, before starting any electrochemical measurement. All Cyclic Voltammetries (CV) were performed starting from the Open Circuit Potential (OCP). No stirring of the electrolytic solution was applied. All Constant Potential Electrolysis (CPE) were conducted under continuous stirring of the solution. Before applying the final constant potential for CPE, a linear potential ramp with a rate of 20 mV/s was applied from the OCP to the potential applied under electrolysis.

Photoelectrochemical measurements were performed under illumination of the electrochemical cell with the solar simulator (AM 1.5 G light) from a distance of 20 cm. A 450 nm long-pass filter was used in order to avoid excitation of WO_3 that could likely form hydroxyl radicals in the presence of water, resulting in the degradation of the organic sensitizer.

6.4 Synthesis

6.4.1 Synthesis of 1,10-phenanthroline-5,6-dione

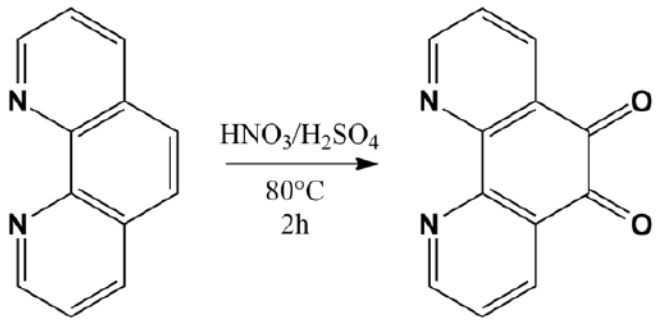

1,10-phenanthroline-5,6-dione was synthesized following the procedure described by Yamada *et al.*[127] A 250 mL round bottom flask containing 4g (22.2 mmol) of 1,10-phenanthroline monohydrate and 24 g (201.6 mmol) of potassium bromide was cooled to 0 ºC using an ice bath. Concentrated sulphuric acid (80 mL) was added in small portions followed by concentrated nitric acid (40 mL). The resulting solution was heated for 2 h at 100ºC, cooled to room temperature and poured into 500 mL of water. The solution was neutralized using a 0.1 M sodium hydroxide solution and extracted with dichloromethane.

The organic phases were collected and the solvent was evaporated to yield 1.5 g of a yellow solid (35% yield).

^{1}H-NMR (CF_3COOD; 300 MHz; δ, ppm): 8.80-9.25 (m, 4H), 8.05-8.35 (m, 2H).

6.4.2 Synthesis of 1,10-phenanthroline-5,6-dioxime

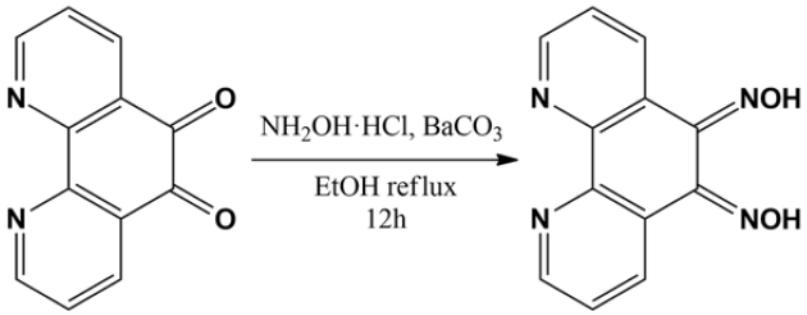

1,10-phenanthroline-5,6-dioxime was synthesized following the procedure described by Bodige *et al.*[128] A dispersion containing a mixture of 1.5 g (7.2 mmol) of 1,10-phenanthroline-5,6-dione, 1.7 g (24.5 mmol) of $NH_2OH{\cdot}HCl$ and 1.82 g (9.2 mmol) of $BaCO_3$ in 150 mL of ethanol was stirred and refluxed for 12 hours. The solvent was evaporated under reduced pressure and treated with 140 mL of 0.2 M $NH_2OH{\cdot}HCl$, stirred for 30 minutes and filtered. The light yellowish solid was thus washed with small fractions of water, ethanol and diethyl ether, and dried under vacuum to yield 1 g (57% yield).

Elemental Analysis calculated (%) for $C_{12}H_8N_4O_2$: C 60.00, H 3.34; found: C 60.02, H 3.60.

6.4.3 Synthesis of 1,10-phenanthroline-5,6-diamine

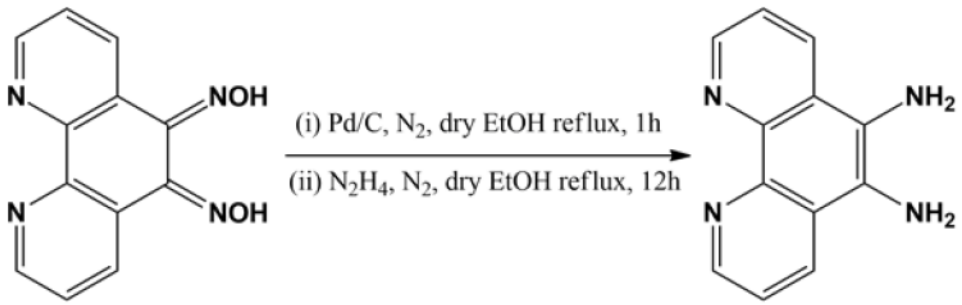

1,10-phenanthroline-5,6-diamine was synthesized following the procedure described by Bodige *et al.*[128] A dispersion of 820 mg (3.34 mmol) of 1,10-phenanthroline-5,6-dioxime

and 800 mg of Pd-C (10%) in 100 mL of absolute ethanol was purged with N_2 for 15 min and heated to reflux. To this mixture, a solution of 7.5 mL of hydrazine monohydrate and 30 mL of ethanol was added over a period of one hour and the resulting mixture refluxed for 12 hours. The mixture was filtered hot through a bed of Celite and the pad was washed several times with 20 mL each of boiling ethanol. The filtrated dried and the residue was triturated with 45 mL of water and left at 4 ºC overnight. The tan precipitate was filtered and washed with cold water to obtain 300 mg of the desired product (42% yield).

Elemental Analysis calculated (%) for $C_{12}H_{10}N_4$: C 68.55, H 4.79, N 26.65; found: C 68.45, H 4.84, N 26.54.

^{1}H-NMR ([d_6]-DMSO; 300 MHz; δ, ppm): 8.77 (m, 2H), 8.47 (m, 2H), 7.60 (m, 2H), 5.22 (s, 4H).

IR (KBr powder; ν, cm^{-1}): 3372, 3267, 3209, 1655, 1605, 1589, 1567, 1486, 1434, 1412, 1305, 799, 733.

6.4.4 Synthesis of Phenantroline-Salophen (2)

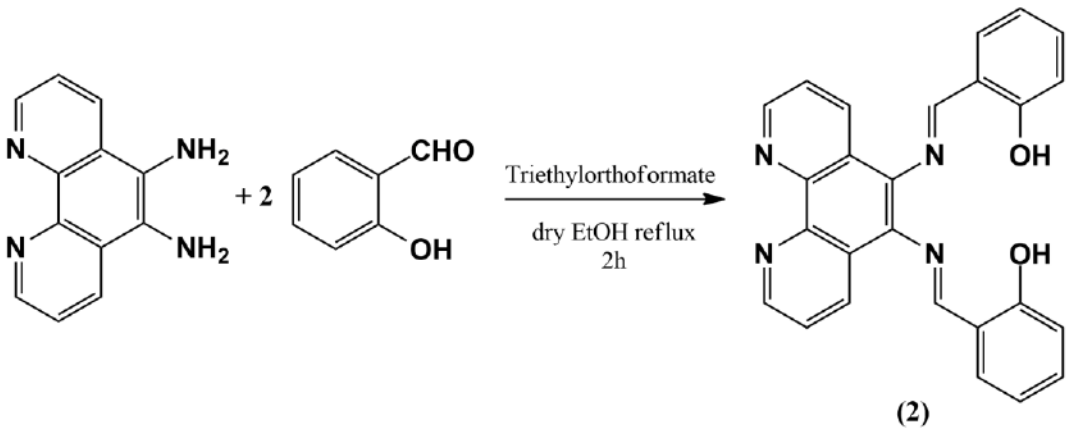

(2)

N,N'-bis(salicylidene)-5,6-(1,10-phenantroline)diamine, **2**, was synthesized adapting the procedure described by Pellegrin *et al.*[125] In a round bottom flask, 200 mg (0.95 mmol) of 1,10-phenantroline-5,6-diamine and 2 mL (20 mmol) of salicylaldehyde were suspended in absolute ethanol together with some drops of triethylorthoformate. The mixture has heated to reflux for 3 hours to observe a precipitate that was collected by filtration, exhaustively washed with diethyl ether and dried under vacuum to obtain 170 mg of a yellow solid (42% yield).

Elemental Analysis calculated (%) for $C_{26}H_{18}N_4O_2$ (418): C 74.63, H 4.34, N 13.39, O 7.65; found: C 73.49, H 4.28, N 14.01.

MS-MALDI-TOF (synapinic acid): m/z 419.2 [MH^+]

^{1}H-NMR ([d_6]-DMSO; 300 MHz; δ, ppm): 13.02 (s, 2H), 9.21 (m, 4H), 8.98-9.10 (dd, 2H), 8.27 (d, 2H), 7.80-8.06 (m, 2H), 7.51 (t, 2H), 7.10-7.25 (m, 4H).

IR (KBr powder, ν, cm^{-1}): 3460 (OH), 3066, 3011, 2981, 2936, 2705 (CH), 1625 (C=N phen), 1514 (C=N imine).

6.4.5 Synthesis of [Ru(bpy)$_2$ PhnSlp]Cl$_2$ (3)

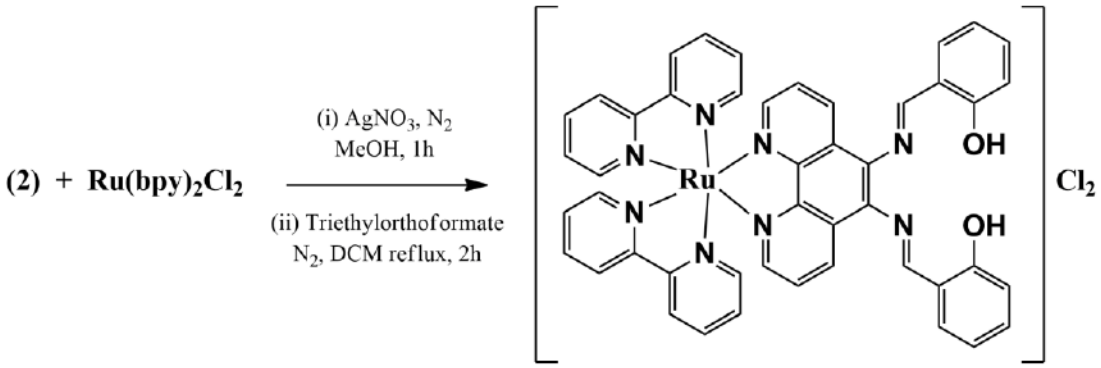

(3)

3 was synthesized adapting the procedure described by Pellegrin *et al.*[125] 60 mg (0.12 mmol) of *cis*-Ru(bpy)$_2$Cl$_2$ and 47 mg (0.28 mmol) of $AgNO_3$ were suspended in 10 mL of methanol. The mixture was stirred for one hour under inert atmosphere and the white precipitate of AgCl filtered off. 58 mg (0.12 mmol) of **2** dissolved in dichloromethane were added to the clear red solution followed by some drops of triethylorthoformate. The mixture was stirred and heated to reflux overnight under nitrogen. The solvent was removed from the reddish solution, the crude product was redissolved in acetone and an excess of tetra-*n*-butylammonium chloride was added, observing the precipitation of a brown solid. The precipitate was collected and exhaustively washed with diethyl ether to remove the excess of the salt. After removal of the solvent, the solid was purified by using chromatography in neutral alumina with dichloromethane/methanol (95:5) as eluent, the first fraction recovered and the solvent evaporated to obtain 90 mg of an orange solid (66% yield).

Elemental Analysis calculated (%) for $C_{62}H_{66}Cl_2N_8O_2Ru$: C 66.06, H 5.90, N 9.94; found: C 67.02, H 5.93, N 10.00.

^{1}H-NMR ([d$_6$]-DMSO, 300 MHz; δ, ppm): 12.77 (s, 2H), 9.38 (d, 2H), 9.25-9.35 (dd, 4H), 8.92 (s, 2H), 8.78 (d, 2H), 8.66 (t, 2H), 8.57 (t, 2H), 8.33 (d, 2H), 8.18-8.30 (m, 4H), 8.06-8.12 (m, 2H), 7.81 (t, 4H), 7.62 (t, 2H), 7.38 (m, 4H).
IR (KBr powder, ν, cm^{-1}): 3426 (OH), 3064, 2970, 2922, 2857 (CH), 1607 (C=N phen), 1585 (C=N imine).

6.4.6 Synthesis of [Ru(bpy)$_2$ CoPhnSlp]Cl$_2$ (1)

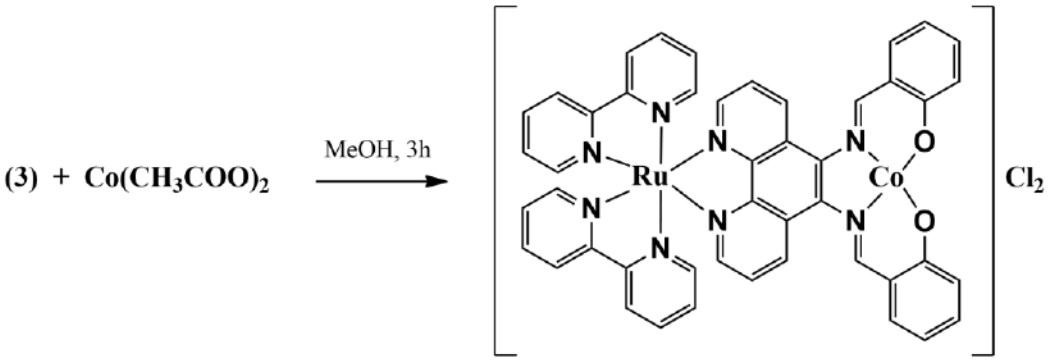

(1)

To a solution of 50 mg (0.05 mmol) of **3** in 10 mL of methanol was added 13 mg (0.05 mmol) of $Co(CH_3COO)_2 \cdot 4H_2O$ and stirred overnight at room temperature. Addition of diethyl ether induced precipitation of a solid that was filtered and washed extensively with diethyl ether to obtain 48 mg of an orangish-brown solid (91% yield).

Elemental Analysis calculated (%) for $C_{46}H_{32}Cl_2CoN_8O_2Ru$: C 57.57, H 3.36, N 11.68; found: C 57.49, H 3.50, N 11.79.
IR (KBr powder; ν, cm^{-1}): 3067, 2969, 2923, 2848 (CH), 1607 (C=N phen), 1552 (C=N imine), 553 (Co-O).

6.4.7 Synthesis of N,N'-bis((trimethylammonium)ethylene) perylene-3,4,9,10-tetracarboxylic acid bisimide (PBI^{2+})

N,N′-bis((trimethylammonium)ethylene)perylene-3,4,9,10-tetracarboxylic acid bisimide bischloride salt (PBI^{2+} 2Cl$^-$) has been synthesized starting from the corresponding bisiodide salt, already described in literature.[184,185] For the exchange of the counterion, the precursor (PBI^{2+} 2I$^-$) was solubilized in a mixture of 2-propanol/HCl$_{conc.}$ and the solution was stirred

for 2 h at room temperature. The precipitate was filtered and washed with 2×30 ml toluene and 2×30 ml Et_2O. The operation was repeated 3 times. The resulting solid is dried under vacuum to afford PBI^{2+} $2Cl^-$ (2.19 g, 80 % yield) as a dark red powder.

ESI-MS: m/z 597.4 [M^{2+}-$2Cl^-$)/2], 281.5.
^{1}H-NMR (TFA_d; 270 MHz; δ, ppm): 8.88 (d, 4H), 8.80 (d, 4H), 4.83 (t, 4H), 3.84 (t, 4H), 3.36 (s, 12H).
^{13}C-NMR (TFA_d; 270 MHz; δ, ppm): 36.4, 55.6, 64.6, 123.5, 126.7, 128.7, 131.6, 135.5, 138.6, 167.8.
IR (KBr powder; ν, cm^{-1}): 1694, 1657 (>CO), 1593 (–C=C-), 1439, 1403, 1343 (>C-N-R).

6.4.8 Synthesis of $Na_{10}\{Ru^{IV}_4(\mu\text{-}O)_4(\mu\text{-}OH)_2(H_2O)_4[\gamma\text{-}SiW_{10}O_{36}]_2\}$ (Ru_4POM)

Ru_4POM was synthesized adapting the procedure by Sartorel *et al*.[71] 0.153 g of $RuCl_3 \cdot xH_2O$ (0.74 mmol) were dissolved in 30 mL of H_2O milliQ. 1 g of $K_8\gamma\text{-}SiW_{10}O_{36} \cdot 12H_2O$ (0.38 mmol) was then added. The dark brown solution has a pH = 6.2, and was kept at 70°C for 1 hour. After heating, the pH was 1.8, and the solution was filtered. Excess of CsCl was added to precipitate the Cs salt, which was then washed three times with 2-3 mL of cold water. $Cs_{10}Ru_4POM$ was then dissolved in 100 mL of H_2O milliQ to prepare the sodium salt after cation exchange by eluting it through a cation exchange resin, charged with Na^+. The crude sodium salt was then purified on an exclusion dimensional sephadex G- 50 column (10 g of stationary phase for 1 g of crude $Na_{10}Ru_4POM$, dissolved in 10 mL of water). The purified $Na_{10}Ru_4POM$ was finally obtained after removal of the solvent (800 mg, 74% yield).

IR (KBr powder; ν, cm^{-1}): 3434, 2923, 2853, 1622, 1044, 999, 950, 876, 804, 539.

6.5 Photoanodes preparation

Tungsten oxide deposition

The deposition of tungsten oxide, WO_3, onto fluorine doped tin oxide (FTO) electrodes was performed at the Department of Chemistry and Pharmaceutical Sciences of the University of Ferrara (in collaboration with Prof. Bignozzi and Dr. Berardi), with the deposition method

reported in literature.[115] Tungsten oxide colloidal paste was deposited by spin coating (6 s at 600 rpm followed by 20 s at 2000 rpm) onto a portion of the active area of cleaned FTO slides and dried with warm air stream before sintering at 550°C for 30 minutes (to obtain a monoclinic nanocrystalline layer): six layers of WO_3 were deposited with this procedure and the sintering time was prolonged to 45 minutes for the last layer. From experimental measurements, this deposition procedure showed the best results in terms of electrode performances. The surface was activated by soaking the slides in aqueous 1 M H_2SO_4 at room temperature for 2 hours, after which they were rinsed with ethanol, dried under warm air stream, and finally sintered at 550°C for 45 minutes.

Dye-sensitization of WO_3 with PBI^{2+}

The electrodes were heated at 450°C for 15 minutes to activate the WO_3 surface, left to cool and then soaked into a 1 mM $PBI(PF_6)_2$ solution in acetonitrile at 50°C for 6 hours. The sensitized-electrodes were then rinsed with acetonitrile to remove the excess of dye and dried in N_2 flow.

Ru_4POM catalyst deposition

Three kinds of procedure were tested:

- pristine Ru_4POM was deposited by 5 minutes soaking of the dye-sensitized WO_3 photoanodes in aqueous solutions of Ru_4POM with different concentrations (9 mM and 1 mM) in 0.1 M $NaClO_4$ pH 3, followed by rinsing with milliQ water and drying in N_2 flow;
- aggregates of PBI^{2+}/Ru_4POM with 5:1 stoichiometry formed in water were deposited by 10 minutes soaking of the dye-sensitized photoanodes in a $PBI(Cl)_2$ 0.1 mM and Ru_4POM 0.02 mM solution in milliQ water, then rinsed with milliQ water and dried in N_2 flow;
- a 98% acetonitrile - 2% milliQ water solution with 0.1 mM $PBI(PF_6)_2$ and 0.02 mM in Ru_4POM was prepared by mixing a $PBI(PF_6)_2$ 1 mM solution in acetonitrile and a Ru_4POM 1 mM solution in milliQ water, in order to obtain a solution of PBI^{2+}/Ru_4POM aggregates with 5:1 stoichiometry in acetonitrile; sensitized electrodes were then soaked for 10 minutes in the solution, rinsed with ethanol and dried in N_2 flow.

Appendix

Appendix

A.1 Calculation of the steady state concentration of PBI^{*2+}

The steady state concentration of the PBI^{2+} excited state has been calculated with a simple analytical model, considering the rate equations describing the fractions of the molecular ground state, n_0, and the excited state, n_1:[186,187]

$$\frac{dn_1}{dt} = \frac{P\sigma}{Shv}(n_0 - n_1) - (K_r + K_{nr})n_1 \quad (A.1)$$

$$\frac{dn_0}{dt} = -\frac{P\sigma}{Shv}(n_0 - n_1) + (K_r + K_{nr})n_1 \quad (A.2)$$

$$n_0 + n_1 = 1 \quad (A.3)$$

where P [W] is the irradiation power; S [cm^2] is the irradiated spot area; σ [cm^2] = 2303·ε/N_{Av} is the absorption cross section; $h\nu = hc/\lambda$ is the energy of photons (h is the Planck's constant [J·s]); K_r [s^{-1}] is the radiative decay rate and K_{nr} [s^{-1}] is the non-radiative decay rate.

At weak irradiation power used in photocatalytic experiments, $n_1 << n_0$ and n_0-$n_1 \approx 1$ (ground state non-depletion approximation). In steady state hypothesis, the time derivative in Eq. A.1 can be neglected to yield:

$$0 \approx \frac{dn_1}{dt} = \frac{P\sigma\lambda}{Shc}(n_0 - n_1) - (K_r + K_{nr})n_1 \Longrightarrow$$

$$n_1 \approx \frac{P\sigma\lambda/Shc}{(K_r + K_{nr})} \quad (A.4)$$

$$n_1 \approx I\sigma\tau_{excited\ state} \quad (A.5)$$

where $I = P\lambda/Shc$ and $\tau_{excited\ state} = 1/(K_r + K_{nr})$.

Eqs. A.1-A.5 can be employed assuming the use of monochromatic light. In this case, where a LED white lamp is used, the total fraction of molecules in the excited state can be obtained from the integration of the contribution at each wavelength to the molecule fraction in the excited state generated by light (Eq. A.6):

$$n_1 \approx \int I_\lambda(\lambda)\sigma_\lambda(\lambda)\tau_{excited\ state}\, d\lambda \quad (A.6)$$

The term $I_\lambda(\lambda)$, the photon flux per surface unit [photon s^{-1} cm^{-2} nm^{-1}] at wavelength λ, shows the dependence from the irradiation power. The $P_\lambda(\lambda)/S$ value, the spectral irradiance [W cm^{-}

^{2} nm^{-1}], is obtained from the emission spectrum of the LED white lamp, whose area is equal to the total irradiation power of the lamp per surface unit (4.5×10^{-3} W cm^{-2}) (Fig. A.1). In this way, the photon flux at each wavelength can be calculated from Eq. A.7:

$$I_\lambda(\lambda) = \frac{P_\lambda(\lambda)\lambda}{Shc} \tag{A.7}$$

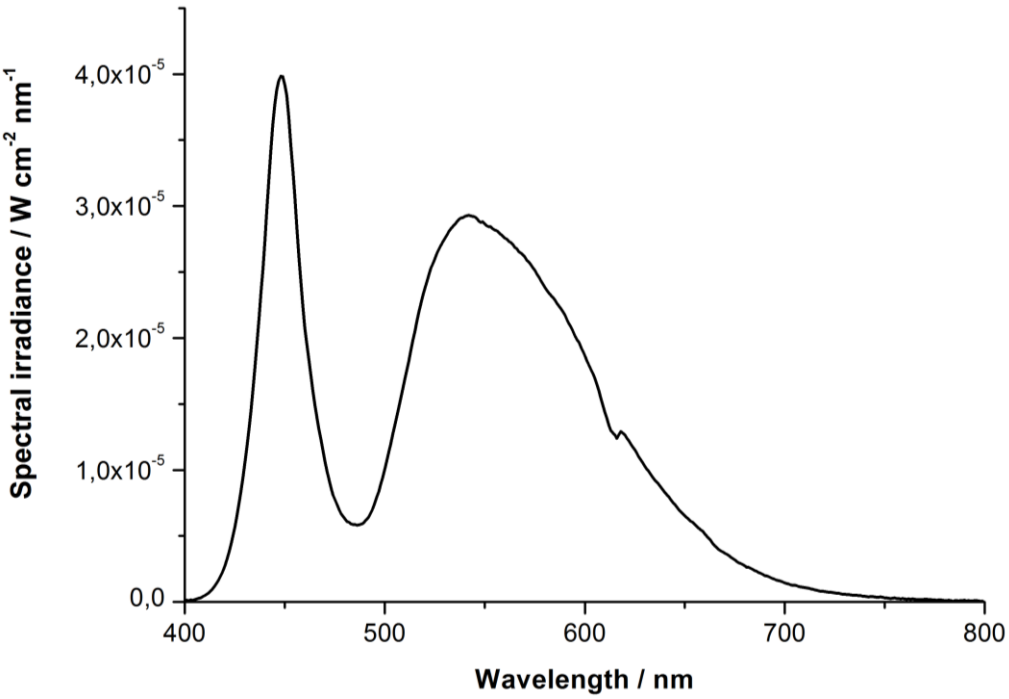

Fig. A.1 Emission spectrum of the LED white lamp used in photocatalytic experiments. The area has been normalized (the resolution of the spectum is 1 nm) to 4.5×10^{-3} W cm^{-2}, irradiance power of the lamp.

The term $\sigma_\lambda(\lambda)$, the absorption cross section [cm^2] at wavelength λ, shows the dependence from the absorption spectrum of the irradiated solution (Fig. A.2) and can be calculated from Eq. A.8. The $\varepsilon(\lambda)$ values are calculated assuming that the absorbance is given only by the dye.

$$\sigma_\lambda(\lambda) = \frac{2303\varepsilon(\lambda)}{\mathcal{N}_{Av}} \tag{A.8}$$

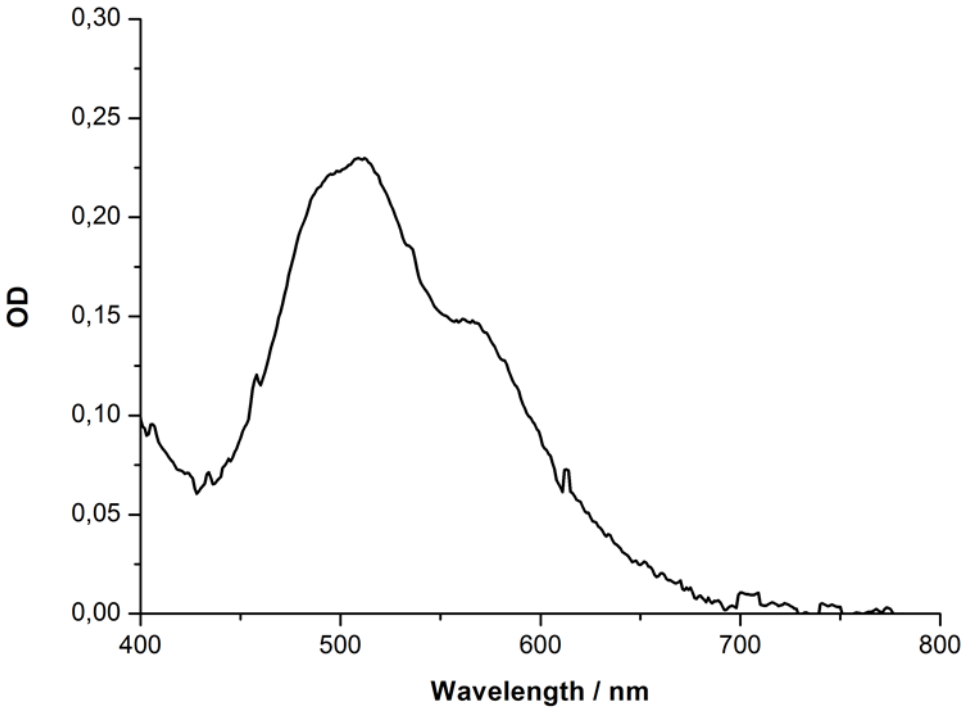

Fig. A.2 Absorption spectrum (optical path 1 mm) of the reaction mixture before oxygen evolving catalysis, corrected for the scattering contribution. Conditions: $[PBI^{2+}] = 10^{-4}$ M, $[Ru_4POM] = 15\times10^{-6}$ M and $[S_2O_8^{2-}] = 10^{-3}$ M in 20 mM phosphate buffer pH 7.0.

The term $\tau_{excited\ state}$ [s] is then given by transient absorption spectroscopy experiments (see section 3.2.1.2). In the presence of Ru_4POM, the lifetime of the excited state of PBI^{2+} is less than 100 picoseconds, since the electron transfer from Ru_4POM to PBI^{*2+} occurs.

From Eq. A.6, the fraction of molecules in the excited state results 5.79×10^{-11}. Finally, this value is multiplied by the dye concentration (10^{-4} M), giving 5.79×10^{-15} M, the steady state concentration of PBI^{2+} in the excited state.

A.2 Quantum yield determination

Since the light source used in photocatalytic experiments has a broad spectrum (non-monochromatic spectrum), usual methods for determination of photon fluxes and quantum yields has to be modify to take into account the different energies of the photons arriving at the sample.[188]

The quantum yield of a reaction (Φ) can be calculated dividing the rate of the reaction, v_r [mol s^{-1}], by the amount of excitation per second, θ [mol s^{-1}] (Eq. A.9). The excitation per

second can be calculated from Eq. A.10, where $\varphi_0(\lambda)$ is the photon flux per unit wavelength [mol s^{-1} nm^{-1}]. In these calculation the validity of Kasha's rule is assumed, stating that the same excited state is reached for different energies of photons. The photon flux per wavelength, $\varphi_0(\lambda)$, can be determined from the emission spectrum of the LED white lamp according to Eq. A.11. In this equation $P(\lambda)$ [W nm^{-1}] is given by Eq. A.12, where P_{tot} is the total irradiation power of the lamp (4.5×10^{-3} W cm^{-2} multiplied by the irradiated surface of the reactor, 5.2×1.3 cm^2).

The term θ depends also on the probability of absorption of a photon of the incoming irradiation source by the photocatalytic mixture, $P_{abs}(\lambda)$, and this probability depends on the wavelength of the incoming photon, according to Eq. A.13. In this equation, $A_{tot}(\lambda)$ is the measured absorbance at wavelength λ for a UV-Vis cell. Since the absorption spectrum of the photocatalytic solution was measured on a cuvette with b = 0.1 cm optical path, whereas irradiation of the solution in the reactor was performed with an optical pathlength of ℓ = 1.3 cm (reactor depth), the total absorbance of the solution being irradiated by the lamp can be obtained, correcting $A_{tot}(\lambda)$ for ℓ/b.

$$\Phi = \frac{v_r}{\theta} \tag{A.9}$$

$$\theta = \int \varphi_0(\lambda) P_{abs}(\lambda)\, d\lambda \tag{A.10}$$

$$\varphi_0(\lambda) = \frac{P(\lambda)\lambda}{hc\mathcal{N}_{Av}} \tag{A.11}$$

$$\int P_\lambda(\lambda)\, d\lambda = P_{tot} \tag{A.12}$$

$$P_{abs}(\lambda) = (1 - 10^{-(A_{tot}(\lambda)\cdot\ell/b)}) \tag{A.13}$$

The calculated $\varphi_0(\lambda)$ and $P_{abs}(\lambda)$ are reported in Fig. A.3 (blue line and black line, respectively). The resulting product equals the θ value (red line), assuming that the quantum yield of the reaction is constant for the wavelength range studied, according to Kasha's rule.

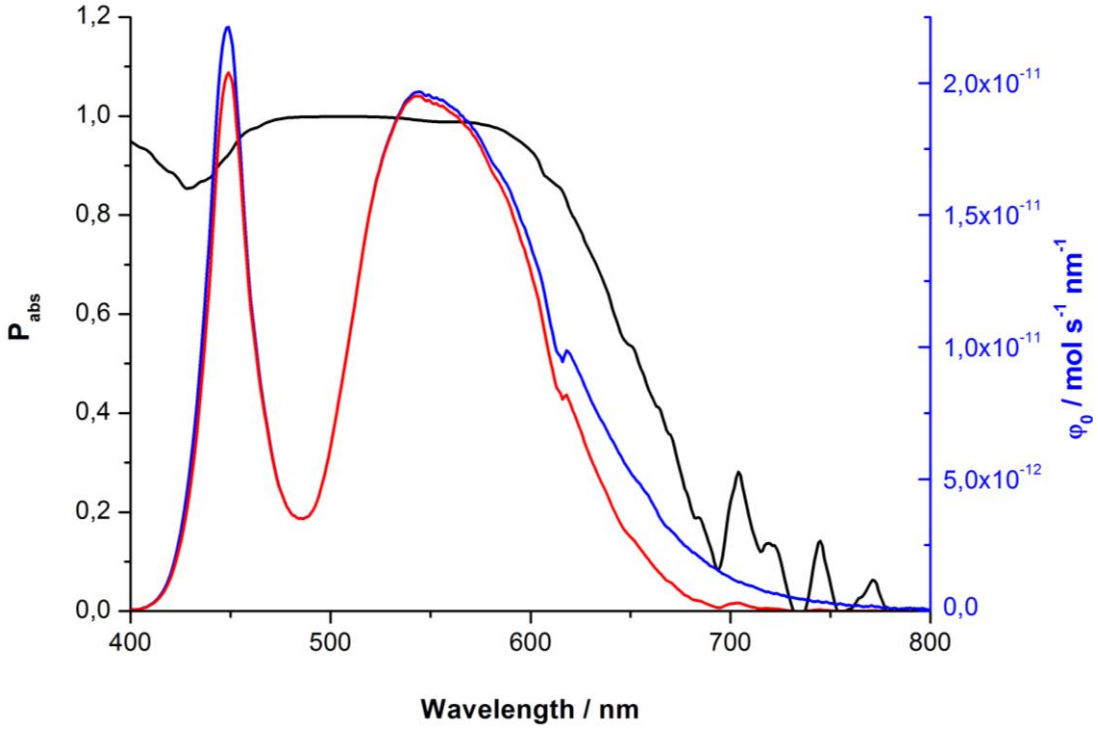

Fig. A.3 Plot of the incoming total photon flux $\varphi_0(\lambda)$ (blue curve, right axis) and of the probability of absorption $P_{abs}(\lambda)$ (black curve, left axis); the red curve (right axis) shows the resulting product of the two functions.

Finally, to determine the quantum yield of the reaction, the rate of product formation v_r is divided by θ (2.70×10^{-9} mol s^{-1}), according to Eq. A.9. In Table A.1, the calculated quantum yield for each photocatalytic experiment has been reported.

Table A.1 Initial rate of O_2 production determined as the linear kinetic slope and quantum yield, determined for each photocatalytic experiment (calculated $\theta = 2.70\times10^{-9}$ mol s^{-1}). Reaction conditions: 4.5 mL of 20 mM phosphate buffer pH = 7.0, $[PBI^{2+}] = 10^{-4}$ M, $[S_2O_8^{2-}] = 10^{-3}$ M, irradiation with a spotlight (4.5 mW/cm^2).

Ru_4POM [μM]	Rate/10^{-3} [c] [nmol O_2 s^{-1}]	Quantum Yield
3	24±4	0.009
7.5	29±7	0.011
15	45±3	0.017
30	60±5	0.022
60	62±7	0.023

Appendix

References

[1] British Petroleum (BP), *BP Statistical Review of World Energy - Full Report*, **2016**.

[2] U.S. Energy Information Administration, *International Energy Outlook*, **2016**.

[3] World Energy Council, *World Energy Issues Monitor*, **2016**.

[4] International Energy Agency, *Key World Energy Statistics*, **2015**.

[5] Department of Economic and Social Affairs, *World Population Prospects*, **2015**.

[6] Eurostat Statistical books, *The EU in the World, 2015 Edition*, **2015**.

[7] European Commission, *EU Energy in Figures, Statistical Pocketbook 2015*, **2015**.

[8] D. Ahuja, M. Tatsutani, *S.A.P.I.EN.S.* **2009**, *2*, 1–16.

[9] R. D. Vidic, S. L. Brantley, J. M. Vandenbossche, D. Yoxtheimer, J. D. Abad, *Science,* **2013**, *340*, 1235009.

[10] N. Armaroli, V. Balzani, *Angew. Chemie - Int. Ed.* **2007**, *46*, 52–66.

[11] T. F. Stocker, *Science,* **2013**, *339*, 280–282.

[12] V. Balzani, A. Credi, M. Venturi, *ChemSusChem* **2008**, *1*, 26–58.

[13] G. Ciamician, *Science,* **1912**, *36*, 385–394.

[14] J. Barber, *Chem. Soc. Rev.* **2009**, *38*, 185–196.

[15] K. N. Ferreira, T. M. Iverson, K. Maghlaoui, J. Barber, *Science,* **2004**, *303*, 1831–1838.

[16] R. E. Blankenship, *Molecular Mechanisms of Photosynthesis, 2nd Edition*, **2014**.

[17] A. W. Rutherford, P. Faller, *Philos. Trans. R. Soc. Lond. B. Biol. Sci.* **2003**, *358*, 245–253.

[18] M. D. Kärkäs, O. Verho, E. V. Johnston, B. Åkermark, *Chem. Rev.* **2014**, *114*, 11863–12001.

[19] M. Grabolle, H. Dau, *Biochim. Biophys. Acta* **2005**, *1708*, 209–218.

[20] Y. Umena, K. Kawakami, J.-R. Shen, N. Kamiya, *Nature* **2011**, *473*, 55–60.

[21] M. Suga, F. Akita, K. Hirata, G. Ueno, H. Murakami, Y. Nakajima, T. Shimizu, K. Yamashita, M. Yamamoto, H. Ago, et al., *Nature* **2015**, *517*, 99–103.

[22] B. Loll, J. Kern, W. Saenger, A. Zouni, J. Biesiadka, *Nature* **2005**, *438*, 1040–1044.

[23] A. Zouni, H.-T. Witt, J. Kern, P. Fromme, N. Krauss, W. Saenger, P. Orth, *Nature* **2001**, *409*, 739–743.

[24] A. Guskov, J. Kern, A. Gabdulkhakov, M. Broser, A. Zouni, W. Saenger, *Nat. Struct. Mol. Biol.* **2009**, *16*, 334–342.

[25] J. Yano, J. Kern, K. Sauer, M. J. Latimer, Y. Pushkar, J. Biesiadka, B. Loll, W. Saenger, J. Messinger, A. Zouni, et al., *Science,* **2006**, *314*, 821–825.

[26] J. M. Peloquin, K. A. Campbell, D. W. Randall, M. A. Evanchik, V. L. Pecoraro, W. H. Armstrong, R. D. Britt, *J. Am. Chem. Soc.* **2000**, *122*, 10926–10942.

[27] J. Yano, V. Yachandra, *Chem. Rev.* **2014**, *114*, 4175–4205.

[28] I. D. Young, M. Ibrahim, R. Chatterjee, S. Gul, F. D. Fuller, S. Koroidov, A. S. Brewster, R. Tran, R. Alonso-Mori, T. Kroll, et al., *Nature* **2016**, 1–22.

[29] B. Kok, B. Forbush, M. McGloin, *Photochem. Photobiol.* **1970**, *11*, 457–475.

[30] M. Askerka, J. Wang, D. J. Vinyard, G. W. Brudvig, V. S. Batista, *Biochemistry* **2016**, *55*, 981–984.

[31] M. H. V. Huynh, T. J. Meyer, *Chem. Rev.* **2007**, *107*, 5004–5064.

[32] T. J. Meyer, *Nature* **2008**, *451*, 778–779.

[33] M. D. Kärkäs, B. Åkermark, *Dalt. Trans.* **2016**, *45*, 14421–14461.

[34] P. Ceroni, A. Credi, M. Venturi, V. Balzani, *Photochem. Photobiol. Sci.* **2010**, *9*, 1561–1573.

[35] J. H. Alstrum-Acevedo, M. K. Brennaman, T. J. Meyer, *Inorg. Chem.* **2005**, *44*, 6802–6827.

[36] P. D. Frischmann, K. Mahata, F. Würthner, *Chem. Soc. Rev.* **2013**, *42*, 1847–1870.

[37] P. Du, R. Eisenberg, *Energy Environ. Sci.* **2012**, *5*, 6012–6021.

[38] X. Sala, S. Maji, R. Bofill, J. García-Antón, L. Escriche, A. Llobet, *Acc. Chem. Res.* **2014**, *47*, 504–516.

[39] S. Berardi, S. Drouet, L. Francàs, C. Gimbert-Suriñach, M. Guttentag, C. Richmond, T. Stoll, A. Llobet, *Chem. Soc. Rev.* **2014**, *43*, 7501–7519.

[40] F. Bolletta, A. Juris, M. Maestri, D. Sandrini, *Inorg. Chim. Acta* **1980**, *44*, L175–L176.

[41] G. Navon, N. Sutin, *Inorg. Chem.* **1974**, *13*, 2159–2164.

[42] A. Sartorel, M. Bonchio, S. Campagna, F. Scandola, *Chem. Soc. Rev.* **2013**, *42*, 2262–2280.

[43] C. Costentin, S. Drouet, M. Robert, J. M. Savéant, *J. Am. Chem. Soc.* **2012**, *134*, 11235–11242.

[44] E. S. Rountree, B. D. McCarthy, T. T. Eisenhart, J. L. Dempsey, *Inorg. Chem.* **2014**, *53*, 9983–10002.

[45] J. R. Swierk, T. E. Mallouk, *Chem. Soc. Rev.* **2013**, *42*, 2357–2387.

[46] K. S. Joya, J. L. Vallés-Pardo, Y. F. Joya, T. Eisenmayer, B. Thomas, F. Buda, H. J. M. De Groot, *Chempluschem* **2013**, *78*, 35–47.

[47] J.-M. Savéant, *ChemElectroChem* **2016**, *3*, 1–12.

[48] A. J. Bard, L. R. Faulkner, *ELECTROCHEMICAL METHODS Fundamentals and Applications*, **2001**.

[49] C. Costentin, J.-M. Savéant, *ChemElectroChem* **2014**, *1*, 1226–1236.

[50] F. Puntoriero, A. Sartorel, M. Orlandi, G. La Ganga, S. Serroni, M. Bonchio, F. Scandola, S. Campagna, *Coord. Chem. Rev.* **2011**, *255*, 2594–2601.

[51] S. Hammes-Schiffer, *Acc. Chem. Res.* **2009**, *42*, 1881–1889.

[52] C. L. Hill, *Chem. Soc. Rev.* **2012**, *41*, 7572–7589.

[53] S. Campagna, G. Denti, S. Serroni, A. Juris, M. Venturi, V. Ricevuto, V. Balzani, *Chem. Eur. J.* **1995**, *1*, 211–221.

[54] F. Puntoriero, G. La Ganga, A. Sartorel, M. Carraro, G. Scorrano, M. Bonchio, S. Campagna, *Chem. Commun.* **2010**, *46*, 4725–4727.

[55] M. Burian, Z. Syrgiannis, G. La Ganga, F. Puntoriero, M. Natali, F. Scandola, S. Campagna, M. Prato, M. Bonchio, H. Amenitsch, et al., *Inorg. Chim. Acta* **2017**, *454*, 171–175.

[56] H.-C. Chen, D. G. H. Hetterscheid, R. M. Williams, J. I. van der Vlugt, J. N. H. Reek, A. M. Brouwer, *Energy Environ. Sci.* **2015**, *8*, 975–982.

[57] P. Chen, O. S. Finikova, Z. Ou, S. A. Vinogradov, K. M. Kadish, *Inorg. Chem.* **2012**, *51*, 6200–6210.

[58] M. Natali, E. Deponti, D. Vilona, A. Sartorel, M. Bonchio, F. Scandola, *Eur. J. Inorg. Chem.* **2015**, *21*, 3467–3477.

[59] S.-T. Zheng, G.-Y. Yang, *Chem. Soc. Rev.* **2012**, *41*, 7623–7646.

[60] D. M. Robinson, Y. B. Go, M. Greenblatt, G. C. Dismukes, *J. Am. Chem. Soc.* **2010**, *132*, 11467–11469.

[61] F. Jiao, H. Frei, *Chem. Commun.* **2010**, *46*, 2920–2922.

[62] T. Nakagawa, C. A. Beasley, R. W. Murray, *J. Phys. Chem. C* **2009**, *113*, 12958–12961.

[63] A. Mills, P. A. Duckmanton, J. Reglinski, *Chem. Commun.* **2010**, *46*, 2397–2398.

[64] R. Brimblecombe, G. C. Dismukes, G. F. Swiegers, L. Spiccia, *Dalt. Trans.* **2009**, 9374–9384.

[65] X. Sala, I. Romero, M. Rodríguez, L. Escriche, A. Llobet, *Angew. Chemie - Int. Ed.* **2009**, *48*, 2842–2852.

[66] L. Li, L. Duan, Y. Xu, M. Gorlov, A. Hagfeldt, L. Sun, *Chem. Commun.* **2010**, *46*, 7307–7309.

[67] V. Artero, M. Fontecave, *Chem. Soc. Rev.* **2013**, *42*, 2338–2356.

[68] B. Limburg, E. Bouwman, S. Bonnet, *Coord. Chem. Rev.* **2012**, *256*, 1451–1467.

[69] S. S. Mal, U. Kortz, *Angew. Chemie - Int. Ed.* **2005**, *44*, 3777–3780.

[70] B. S. Bassil, M. Ibrahim, R. Al-Oweini, M. Asano, Z. Wang, J. Van Tol, N. S. Dalal, K.-Y. Choi, R. Ngo Biboum, B. Keita, et al., *Angew. Chemie - Int. Ed.* **2011**, *50*, 5961–5964.

[71] A. Sartorel, M. Carraro, G. Scorrano, R. De Zorzi, S. Geremia, N. D. McDaniel, S. Bernhard, M. Bonchio, *J. Am. Chem. Soc.* **2008**, *130*, 5006–5007.

[72] Y. V. Geletii, B. Botar, P. Kögerler, D. A. Hillesheim, D. G. Musaev, C. L. Hill, *Angew. Chemie - Int. Ed.* **2008**, *47*, 3896–3899.

[73] Y. V. Geletii, Z. Huang, Y. Hou, D. G. Musaev, T. Lian, C. L. Hill, *J. Am. Chem. Soc.* **2009**, *131*, 7522–7523.

[74] M. Orlandi, R. Argazzi, A. Sartorel, M. Carraro, G. Scorrano, M. Bonchio, F. Scandola, *Chem. Commun.* **2010**, *46*, 3152–3154.

[75] M. Natali, M. Orlandi, S. Berardi, S. Campagna, M. Bonchio, A. Sartorel, F. Scandola, *Inorg. Chem.* **2012**, *51*, 7324–7331.

[76] M. Hara, C. C. Waraksa, J. T. Lean, B. A. Lewis, T. E. Mallouk, *J. Phys. Chem. A* **2000**, *104*, 5275–5280.

[77] A. Sartorel, P. Miró, E. Salvadori, S. Romain, M. Carraro, G. Scorrano, M. Di Valentin, A. Llobet, C. Bo, M. Bonchio, *J. Am. Chem. Soc.* **2009**, *131*, 16051–16053.

[78] Y. Liu, S.-X. Guo, A. M. Bond, J. Zhang, Y. V. Geletii, C. L. Hill, *Inorg. Chem.* **2013**, *52*, 11986−11996.

[79] A. Sartorel, M. Carraro, F. M. Toma, M. Prato, M. Bonchio, *Energy Environ. Sci.* **2012**, *5*, 5592–5603.

[80] F. M. Toma, A. Sartorel, M. Iurlo, M. Carraro, P. Parisse, C. Maccato, S. Rapino, B. R. Gonzalez, H. Amenitsch, T. Da Ros, et al., *Nat. Chem.* **2010**, *2*, 826–831.

[81] F. M. Toma, A. Sartorel, M. Iurlo, M. Carraro, S. Rapino, L. Hoober-Burkhardt, T. Da Ros, M. Marcaccio, G. Scorrano, F. Paolucci, et al., *ChemSusChem* **2011**, *4*, 1447–1451.

[82] A. Sartorel, M. Truccolo, S. Berardi, M. Gardan, M. Carraro, F. M. Toma, G. Scorrano, M. Prato, M. Bonchio, *Chem. Commun.* **2011**, *47*, 1716–1718.

[83] B. S. Brunschwig, M. H. Chou, C. Creutz, P. Ghosh, N. Sutin, *J. Am. Chem. Soc.* **1983**, *105*, 4832–4833.

[84] Q. Yin, J. M. Tan, C. Besson, Y. V. Geletii, D. G. Musaev, A. E. Kuznetsov, Z. Luo, K. I. Hardcastle, C. L. Hill, *Science,* **2010**, *328*, 342–345.

[85] Z. Huang, Z. Luo, Y. V. Geletii, J. W. Vickers, Q. Yin, D. Wu, Y. Hou, Y. Ding, J. Song, D. G. Musaev, et al., *J. Am. Chem. Soc.* **2011**, *133*, 2068–2071.

[86] J. J. Stracke, R. G. Finke, *J. Am. Chem. Soc.* **2011**, *133*, 14872–14875.

[87] R. Al-Oweini, A. Sartorel, B. S. Bassil, M. Natali, S. Berardi, F. Scandola, U. Kortz, M. Bonchio, *Angew. Chemie - Int. Ed.* **2014**, *53*, 11182–11185.

[88] L. Duan, F. Bozoglian, S. Mandal, B. Stewart, T. Privalov, A. Llobet, L. Sun, *Nat. Chem.* **2012**, *4*, 418–423.

[89] L. Duan, C. M. Araujo, M. S. G. Ahlquist, L. Sun, *PNAS* **2012**, *109*, 15584–15588.

[90] R. Staehle, L. Tong, L. Wang, L. Duan, A. Fischer, M. S. G. Ahlquist, L. Sun, S. Rau, *Inorg. Chem.* **2014**, *53*, 1307–1319.

[91] L. Wang, L. Duan, L. Tong, L. Sun, *J. Catal.* **2013**, *306*, 129–132.

[92] D. Wang, J. T. Groves, *PNAS* **2013**, *110*, 15579–15584.

[93] T. Nakazono, A. R. Parent, K. Sakai, *Chem. Commun.* **2013**, *49*, 6325–6327.

[94] C.-F. Leung, S.-M. Ng, C.-C. Ko, W.-L. Man, J.-S. Wu, L.-J. Chen, T.-C. Lau, *Energy Environ. Sci.* **2012**, *5*, 7903–7906.

[95] E. Pizzolato, M. Natali, B. Posocco, A. Montellano López, I. Bazzan, M. Di Valentin, P. Galloni, V. Conte, M. Bonchio, F. Scandola, et al., *Chem. Commun.* **2013**, *49*, 9941–9943.

[96] D. K. Dogutan, R. McGuire, D. G. Nocera, *J. Am. Chem. Soc.* **2011**, *133*, 9178–9180.

[97] D. J. Wasylenko, C. Ganesamoorthy, J. Borau-Garcia, C. P. Berlinguette, *Chem. Commun.* **2011**, *47*, 4249–4251.

[98] D. J. Wasylenko, R. D. Palmer, E. Schott, C. P. Berlinguette, *Chem. Commun.* **2012**, *48*, 2107–2109.

[99] W. C. Ellis, N. D. McDaniel, S. Bernhard, T. J. Collins, *J. Am. Chem. Soc.* **2010**, *132*, 10990–10991.

[100] J. L. Fillol, Z. Codolà, I. Garcia-Bosch, L. Gómez, J. J. Pla, M. Costas, *Nat. Chem.* **2011**, *3*, 807–813.

[101] M. K. Coggins, M.-T. Zhang, A. K. Vannucci, C. J. Dares, T. J. Meyer, *J. Am. Chem. Soc.* **2014**, *136*, 5531–5534.

[102] S. M. Barnett, K. I. Goldberg, J. M. Mayer, *Nat. Chem.* **2012**, *4*, 498–502.

[103] M.-T. Zhang, Z. Chen, P. Kang, T. J. Meyer, *J. Am. Chem. Soc.* **2013**, *135*, 2048–2051.

[104] M. Yamamoto, K. Tanaka, *Chempluschem* **2016**, *81*, 1028–1044.

[105] R. L. House, N. Y. M. Iha, R. L. Coppo, L. Alibabaei, B. D. Sherman, P. Kang, M. K. Brennaman, P. G. Hoertz, T. J. Meyer, *J. Photochem. Photobiol. C-Photochemistry Rev.* **2015**, *25*, 32–45.

[106] J. R. Swierk, T. E. Mallouk, *Chem. Soc. Rev.* **2013**, *42*, 2357–2387.

[107] X. Xiang, J. Fielden, W. Rodríguez-Córdoba, Z. Huang, N. Zhang, Z. Luo, D. G. Musaev, T. Lian, C. L. Hill, *J. Phys. Chem. C* **2013**, *117*, 918–926.

[108] J. Fielden, J. M. Sumliner, N. Han, Y. V. Geletii, X. Xiang, D. G. Musaev, T. Lian, C. L. Hill, *Chem. Sci.* **2015**, *6*, 5531–5543.

[109] Y. Gao, X. Ding, J. Liu, L. Wang, Z. Lu, L. Li, L. Sun, *J. Am. Chem. Soc.* **2013**, *135*, 4219–4222.

[110] C. Huang, S. Barlow, S. R. Marder, *J. Org. Chem.* **2011**, *76*, 2386–2407.

[111] D. Görl, X. Zhang, F. Würthner, *Angew. Chemie - Int. Ed.* **2012**, *51*, 6328–6348.

[112] P. D. Frischmann, K. Mahata, F. Würthner, *Chem. Soc. Rev.* **2013**, *42*, 1847–1870.

[113] F. Würthner, C. R. Saha-Möller, B. Fimmel, S. Ogi, P. Leowanawat, D. Schmidt, *Chem. Rev.* **2016**, *116*, 962–1052.

[114] J. T. Kirner, J. J. Stracke, B. A. Gregg, R. G. Finke, *ACS Appl. Mater. Interfaces* **2014**, *6*, 13367–13377.

[115] F. Ronconi, Z. Syrgiannis, A. Bonasera, M. Prato, R. Argazzi, S. Caramori, V. Cristino, C. A. Bignozzi, *J. Am. Chem. Soc.* **2015**, *137*, 4630–4633.

[116] Y.-H. Lai, M. Kato, D. Mersch, E. Reisner, *Faraday Discuss.* **2014**, *176*, 199–211.

[117] D. Mersch, C.-Y. Lee, J. Z. Zhang, K. Brinkert, J. C. Fontecilla-Camps, A. W. Rutherford, E. Reisner, *J. Am. Chem. Soc.* **2015**, *137*, 8541–8549.

[118] K. P. Sokol, D. Mersch, V. Hartmann, J. Z. Zhang, M. M. Nowaczyk, M. Rögner, A. Ruff, W. Schuhmann, N. Plumeré, E. Reisner, *Energy Environ. Sci.* **2016**, *9*, 3698–3709.

[119] N. D. Morris, M. Suzuki, T. E. Mallouk, *J. Phys. Chem. A* **2004**, *108*, 9115–9119.

[120] P. G. Hoertz, Y. Kim, W. J. Youngblood, T. E. Mallouk, *J. Phys. Chem. B* **2007**, *111*, 6845–6856.

[121] S. Berardi, G. La Ganga, M. Natali, I. Bazzan, F. Puntoriero, A. Sartorel, F. Scandola, S. Campagna, M. Bonchio, *J. Am. Chem. Soc.* **2012**, *134*, 11104–11107.

[122] G. La Ganga, F. Puntoriero, S. Campagna, I. Bazzan, S. Berardi, M. Bonchio, A. Sartorel, M. Natali, F. Scandola, *Faraday Discuss.* **2012**, *155*, 177–190.

[123] M. Natali, S. Berardi, A. Sartorel, M. Bonchio, S. Campagna, F. Scandola, *Chem. Commun.* **2012**, *48*, 8808–8810.

[124] A. Montellano López, M. Natali, E. Pizzolato, C. Chiorboli, M. Bonchio, A. Sartorel, F. Scandola, *Phys. Chem. Chem. Phys.* **2014**, *16*, 12000–12007.

[125] Y. Pellegrin, A. Quaranta, P. Dorlet, M. F. Charlot, W. Leibl, A. Aukauloo, *Chem. A Eur. J.* **2005**, *11*, 3698–3710.

[126] Y. Pellegrin, K. E. Berg, G. Blondin, E. Anxolabéhère-Mallart, W. Leibl, A. Aukauloo, *Eur. J. Inorg. Chem.* **2003**, 1900–1910.

[127] M. Yamada, Y. Tanaka, Y. Yoshimoto, S. Kuroda, I. Shimao, *Bull. Chem. Soc. Jpn.* **1992**, *65*, 1006–1011.

[128] S. Bodige, F. M. Macdonnell, *Tetrahedron Lett.* **1997**, *38*, 8159–8160.

[129] C. V. Krishnan, C. Creutz, H. A. Schwarz, N. Sutin, *J. Am. Chem. Soc.* **1983**, *105*, 5617–5623.

[130] A. A. Isse, A. Gennaro, E. Vianello, C. Floriani, *J. Mol. Catal.* **1991**, *70*, 197–208.

[131] S. Campagna, F. Puntoriero, F. Nastasi, G. Bergamini, V. Balzani, *Top. Curr. Chem.* **2007**, *280*, 117–214.

[132] M. N. Ackermann, L. V. Interrante, *Inorg. Chem.* **1984**, *23*, 3904–3911.

[133] A. Pui, C. Dobrota, J.-P. Mahy, *J. Coord. Chem.* **2007**, *60*, 581–595.

[134] B. Ortiz, S.-M. Park, *Bull. Korean Chem. Soc.* **2000**, *21*, 405–411.

[135] N. Bresciani Pahor, M. Calligaris, P. Delise, G. Dodic, G. Nardin, L. Randaccio, *J. Chem. Soc. Dalt. Trans.* **1976**.

[136] B. J. Kennedy, G. D. Fallon, B. M. K. C. Gatehouse, K. S. Murray, *Inorg. Chem.* **1984**, *23*, 580–588.

[137] L. A. Kelly, M. A. J. Rodgers, *J. Phys. Chem.* **1994**, *98*, 6377–6385.

[138] S. H. Alarcón, D. Pagani, J. Bacigalupo, A. C. Olivieri, *J. Mol. Struct.* **1999**, *475*, 233–240.

[139] P. M. Dominiak, E. Grech, G. Barr, S. Teat, P. Mallinson, K. Woźniak, *Chem. - A Eur. J.* **2003**, *9*, 963–970.

[140] A. A. Khandar, B. Shaabani, F. Belaj, A. Bakhtiari, *Inorg. Chim. Acta* **2007**, *360*, 3255–3264.

[141] D. Hong, J. Jung, J. Park, Y. Yamada, T. Suenobu, Y.-M. Lee, W. Nam, S. Fukuzumi, *Energy Environ. Sci.* **2012**, *5*, 7606–7616.

[142] A. R. Parent, R. H. Crabtree, G. W. Brudvig, *Chem. Soc. Rev.* **2013**, *42*, 2247–2252.

[143] T. A. Heimer, E. J. Heilweil, C. A. Bignozzi, G. J. Meyer, *J. Phys. Chem. A* **2000**, *104*, 4256–4262.

[144] M. R. Wasielewski, *Acc. Chem. Res.* **2009**, *42*, 1910–1921.

[145] M. D. Kärkäs, E. V. Johnston, O. Verho, B. Åkermark, *Acc. Chem. Res.* **2014**, *47*, 100–111.

[146] M. T. Vagnini, A. L. Smeigh, J. D. Blakemore, S. W. Eaton, N. D. Schley, F. D'Souza, R. H. Crabtree, G. W. Brudvig, D. T. Co, M. R. Wasielewski, *PNAS* **2012**, *109*, 15651–15656.

[147] E. E. Neuteboom, S. C. J. Meskers, P. A. van Hal, J. K. J. van Duren, E. W. Meijer, R. A. J. Janssen, H. Dupin, G. Pourtois, J. Cornil, R. Lazzaroni, et al., *J. Am. Chem. Soc.* **2003**, *125*, 8625–8638.

[148] B. A. Jones, A. Facchetti, M. R. Wasielewski, T. J. Marks, *J. Am. Chem. Soc.* **2007**, *129*, 15259–15278.

[149] R. J. Lindquist, B. T. Phelan, A. Reynal, E. A. Margulies, L. E. Shoer, J. R. Durrant, M. R. Wasielewski, *J. Mater. Chem. A* **2016**, *4*, 2880–2893.

[150] L. Zhang, J. M. Cole, *ACS Appl. Mater. Interfaces* **2015**, *7*, 3427–3455.

[151] H. Lv, Y. V. Geletii, C. Zhao, J. W. Vickers, G. Zhu, Z. Luo, J. Song, T. Lian, D. G. Musaev, C. L. Hill, *Chem. Soc. Rev.* **2012**, *41*, 7572–7589.

[152] B. Schwarz, J. Forster, M. K. Goetz, D. Yücel, C. Berger, T. Jacob, C. Streb, *Angew. Chemie - Int. Ed.* **2016**, *55*, 6329–6333.

[153] Á. J. Jiménez, R. Krick Calderón, M. S. Rodríguez-Morgade, D. M. Guldi, T. Torres, *Chem. Sci.* **2013**, *4*, 1064–1074.

[154] Á. J. Jiménez, F. Spänig, M. S. Rodríguez-Morgade, K. Ohkubo, S. Fukuzumi, D. M. Guldi, T. Torres, *Org. Lett.* **2007**, *9*, 2481–2484.

[155] V. M. Blas-Ferrando, J. Ortiz, L. Bouissane, K. Ohkubo, S. Fukuzumi, F. Fernández-Lázaro, Á. Sastre-Santos, *Chem. Commun.* **2012**, *48*, 6241–6243.

[156] S. Jin, M. Supur, M. Addicoat, K. Furukawa, L. Chen, T. Nakamura, S. Fukuzumi, S. Irle, D. Jiang, *J. Am. Chem. Soc.* **2015**, *137*, 7817–7827.

[157] A. Prodi, C. Chiorboli, F. Scandola, E. Iengo, E. Alessio, R. Dobrawa, F. Würthner, *J. Am. Chem. Soc.* **2005**, *127*, 1454–1462.

[158] V. V. Roznyatovskiy, R. Carmieli, S. M. Dyar, K. E. Brown, M. R. Wasielewski, *Angew. Chemie - Int. Ed.* **2014**, *53*, 3457–3461.

[159] R. K. Dubey, M. Niemi, K. Kaunisto, K. Stranius, A. Efimov, N. V. Tkachenko, H. Lemmetyinen, *Inorg. Chem.* **2013**, *52*, 9761–9773.

[160] M. Natali, F. Puntoriero, C. Chiorboli, G. La Ganga, A. Sartorel, M. Bonchio, S. Campagna, F. Scandola, *J. Phys. Chem. C* **2015**, *119*, 2371–2379.

[161] Z. Chen, A. Lohr, C. R. Saha-Möller, F. Würthner, *Chem. Soc. Rev.* **2009**, *38*, 564–584.

[162] L. Feng, M. Rudolf, S. Wolfrum, A. Troeger, Z. Slanina, T. Akasaka, S. Nagase, N. Martín, T. Ameri, C. J. Brabec, et al., *J. Am. Chem. Soc.* **2012**, *134*, 12190–12197.

[163] X. Li, L. E. Sinks, B. Rybtchinski, M. R. Wasielewski, *J. Am. Chem. Soc.* **2004**, *126*, 10810–10811.

[164] Y. Guan, Y. Zakrevskyy, J. Stumpe, M. Antonietti, C. F. J. Faul, *Chem. Commun.* **2003**, 894–895.

[165] S. Amiralaei, D. Uzun, H. Icil, *Photochem. Photobiol. Sci.* **2008**, *7*, 936–947.

[166] M. Supur, S. Fukuzumi, *J. Phys. Chem. C* **2012**, *116*, 23274–23282.

[167] Y. Guan, S.-H. Yu, M. Antonietti, C. Böttcher, C. F. J. Faul, *Chem. Eur. J.* **2005**, *11*, 1305–

1311.

[168] N. Tasios, C. Grigoriadis, M. R. Hansen, H. Wonneberger, C. Li, H. W. Spiess, K. Müllen, G. Floudas, *J. Am. Chem. Soc.* **2010**, *132*, 7478–7487.

[169] M. Supur, S. Fukuzumi, *Phys. Chem. Chem. Phys.* **2013**, *15*, 2539–2546.

[170] E. Shirman, A. Ustinov, N. Ben-shitrit, H. Weissman, M. A. Iron, R. Cohen, B. Rybtchinski, *J. Phys. Chem. B* **2008**, *112*, 8855–8858.

[171] A. R. Parent, R. H. Crabtree, G. W. Brudvig, *Chem. Soc. Rev.* **2013**, *42*, 2247–2252.

[172] S. Piccinin, A. Sartorel, G. Aquilanti, A. Goldoni, M. Bonchio, S. Fabris, *PNAS* **2013**, *110*, 4917–4922.

[173] J. Eastman, *Colloid Science: Principles, Methods and Applications, Blackwell Publishing Ltd.*, **2009**.

[174] D. Jing, B. Bhushan, *J. Colloid Interface Sci.* **2015**, *454*, 152–179.

[175] S. Fukuzumi, K. Ohkubo, T. Suenobu, *Acc. Chem. Res.* **2014**, *47*, 1455–1464.

[176] H. E. A. Kramer, M. Hafner, *Berichte der Bunsengesellschaft für Phys. Chemie* **1969**, *73*, 833–834.

[177] R. Memming, *J. Electrochem. Soc.* **1969**, *116*, 785–790.

[178] J. C. Hill, K.-S. Choi, *J. Phys. Chem. C* **2012**, *116*, 7612–7620.

[179] R. A. Carcel, L. Andronic, A. Duta, *Mater. Charact.* **2012**, *70*, 68–73.

[180] C. R. Lhermitte, J. G. Verwer, B. M. Bartlett, *J. Mater. Chem. A* **2016**, *4*, 2960–2968.

[181] F. Gao, Y. Zhao, W. Liang, *J. Phys. Chem. B* **2011**, *115*, 2699–2708.

[182] M. Liberatore, L. Burtone, T. M. Brown, A. Reale, A. Di Carlo, F. Decker, S. Caramori, C. A. Bignozzi, *Appl. Phys. Lett.* **2009**, *94*, 173113.

[183] L. Li, C. Xu, Y. Zhao, S. Chen, K. J. Ziegler, *ACS Appl. Mater. Interfaces* **2015**, *7*, 12824–12831.

[184] Y. Huang, Y. Yan, B. M. Smarsly, Z. Wei, C. F. J. Faul, *J. Mater. Chem.* **2009**, *19*, 2356–2362.

[185] T. Deligeorgiev, D. Zaneva, I. Petkov, I. Timcheva, R. Sabnis, *Dye. Pigment.* **1994**, *24*, 75–81.

[186] V. N. Peters, R. Alexander, D. A. A. Peters, M. A. Noginov, *Sci. Rep.* **2016**, *6*, 33238.

[187] P. Flamant, Y. H. Meyer, *Opt. Commun.* **1973**, *7*, 146–149.

[188] B. Limburg, E. Bouwman, S. Bonnet, *ACS Catal.* **2016**, *6*, 5273–5284.